IMAGING AND SPECTROSCOPY OF INDIVIDUAL PARAMAGNETIC ELECTRONIC STATES ON THE ATOMIC SCALE

by

Kapildeb Ambal

A dissertation submitted to the faculty of
The University of Utah
in partial fulfillment of the requirements for the degree of

Doctor of Philosophy

in

Physics

Department of Physics and Astronomy

The University of Utah

May 2016

Copyright © Kapildeb Ambal 2016

All Rights Reserved

THE UNIVERSITY OF UTAH GRADUATE SCHOOL

STATEMENT OF THESIS APPROVAL

The dissertation of Kapildeb Ambal

has been approved by the following supervisory committee members:

Committee member	Date Approved
Christoph Boehme, Chair	11/17/2015
Clayton C. Williams, Member	11/17/2015
Mikhail Raikh, Member	1/25/2016
Stephan LeBohec, Member	11/17/2015
Ashutosh Tiwari, Member	

and by Carleton DeTar, Chair/Dean of

the Department/College/School of Physics and Astronomy

and by David B. Kieda, Dean of The Graduate School.

ABSTRACT

Localized electronic states, in particular defect states and charge carrier transitions into and between these states, are the microscopic origin for major efficiency limitations of semiconductor materials and devices. Investigating these defects and their physical properties, including their chemical identity, their energy and spatial distribution, and also their paramagnetic behavior (spin relaxation times, spin-dependent transitions, spin coupling parameters), can strongly improve the understanding of how defects interact with macroscopic materials' properties and thus, it can help to find and create better semiconductor materials and devices.

The focus of the study presented in the following chapters was to open up experimental access to the detection of single electronic defects in condensed matter with sub–nanometer spatial resolution that simultaneously also allows for the identification of a defect's chemical identity and magneto–electronic properties like spin. First, a brief overview about a theoretically described single–spin magnetic resonance tunneling force microscopy concept is presented, for which it is proposed to observe the spin–manifold of individual defects through detection of random telegraph noise produced by spin–dependent tunneling into and out of the probe state. Then, several key requirements for the implementation of this concept are implemented and verified by utilization of a low-temperature ultra–high–vacuum scanning probe microscope. In particular, it is demonstrated that it is possible to (i) prepare a silicondioxide layer on crystalline silicon with very high ($> 5 \times 10^{18}\text{cm}^{-3}$) densities of silicon dangling bonds (so–called E' centers) that possess a spin–dynamics that is suitable for their utilization as spin–readout probes for the investigated spin–microscopy concept; (ii) implement a set of magnetic field field coils into the given low–temperature ultra–high–vacuum scanning–probe setup that allow for the excitation of magnetic resonance at low magnetic fields (<20mT); (iii) use this setup for the detection and imaging of individual phosphorous donor atoms, individual surface defect states, as

well as charge currents that percolate through these states under appropriate bias conditions, and (iv) observe random telegraph noise of the Coulomb forces caused by individual electrons that randomly tunnel into and out of the observed highly localized surface states.

To my Mother and Father

CONTENTS

ABSTRACT iii

LIST OF FIGURES viii

ACKNOWLEDGMENTS xviii

CHAPTERS

1. INTRODUCTION 1

1.1 Finding pathways for a single–spin spectroscopy with atomic spatial resolution 2
1.2 References 6

2. EXPERIMENTAL METHODS AND RELATED TECHNIQUES 9

2.1 Magnetic resonance spectroscopy of point defects 9
2.1.1 ODMR and EDMR 10
2.2 Scanning probe microscopy techniques 12
2.2.1 Non-contact atomic force microscopy 13
2.2.2 Quantum tunneling and scanning tunneling microscopy 16
2.2.3 Single–electron tunneling force microscopy 16
2.3 Single–spin magnetic resonance tunneling force microscopy with atomic resolution 20
2.3.1 Spin–selection rule based single–spin detection 21
2.3.2 The experimental setup for SSTFM 22
2.3.3 The measurement principle behind SSTFM 22
2.4 References 30

3. SYNTHESIS OF THIN SILICON DIOXIDE LAYERS WITH HIGH DENSITIES OF PARAMAGNETIC E′ CENTER WITH LONG SPIN–RELAXATION TIMES 36

3.1 Introduction 36
3.2 Experimental techniques 40
3.3 Materials preparation: Synthesis of thin SiO_2 films with very high E′ center densities 41
3.4 Thermal and light induced stability of very high E′ center density films 44
3.5 Spin relaxation dynamics of E′ centers at high–densities 48
3.6 Transverse spin relaxation 49
3.7 Longitudinal spin relaxation 51
3.8 Summary and conclusions 55
3.9 References 56

4. IN–SITU ABSOLUTE MAGNETOMETRY IN A UHV SCANNING PROBE MICROSCOPE BASED ON A CONDUCTING POLYMER THIN–FILM . . . 59
4.1 Introduction . . . 59
4.2 Experiment . . . 61
4.3 Field calibration and vector magnetometry . . . 65
4.4 Distribution of magnetic field . . . 69
4.5 Conclusions and summary . . . 69
4.6 References . . . 71

5. ELECTRICAL CURRENT THROUGH INDIVIDUAL PAIRS OF PHOSPHORUS DONOR ATOMS AND SILICON DANGLING BONDS . . . 73
5.1 Introduction . . . 73
5.2 Sample and tip preparation . . . 74
5.2.1 Conduction AFM . . . 74
5.2.2 Probe preparation . . . 75
5.2.3 Sample preparation . . . 75
5.3 Experimental details . . . 76
5.4 Detection of surface dangling bond states . . . 82
5.4.1 The current-voltage characteristics of P-db pairs . . . 89
5.5 Reproducibility and uniqueness of I-V curves . . . 91
5.6 Discussion and conclusions . . . 92
5.7 References . . . 95

6. BARRIER WIDTH DEPENDENCE OF INDIVIDUALLY OBSERVED SINGLE ELECTRON TUNNELING EVENTS . . . 98
6.1 Introduction . . . 98
6.2 Theoretical prediction of the cantilever frequency shift due to a single elementary charge transition . . . 100
6.3 Experiment . . . 102
6.4 Single electron tunneling force spectroscopy/microscopy . . . 103
6.5 Random tunneling signal (RTS) . . . 106
6.6 Conclusion . . . 110
6.7 References . . . 111

7. SUMMARY AND OUTLOOK . . . 113

LIST OF FIGURES

2.1 Illustration of a standard AFM setup. A micromechanical oscillating metal cantilever probe is placed above the investigated surface. A focused laser beam is incident onto the cantilever and reflected back to the detector in order to measure the cantilever oscillation. An amplitude feedback control loop maintains a constant oscillation amplitude by compensation of attenuation losses through an excitation piezo element. The frequency modulation (FM) demodulator measures the change of the cantilever resonance frequency caused by tip–sample interaction forces. The X and Y feedback control facilitates the lateral scan across the sample surface. 14

2.2 Illustration of a metal cantilever probe that is placed above a localized state within a dielectric sample surface. The cantilever is oscillating at its resonance frequency f_0. A negative bias is applied to the metal probe and its Fermi energy is raised. The probe height is then ramped vertically up and down by a few nm. When the tunneling conditions are fulfilled, electron will tunnel from the metal probe to a defect state or vice versa and an electrostatic force change will introduce an abrupt frequency change of the cantilever. 17

2.3 Illustration of an electron wavefunction within the energy band diagram of a metal probe–to–sample system with a localized state in surface proximity. Tunneling of an electron from the metal probe to the localized electronic state in the dielectric surface becomes likely for a sufficiently small gap (<2nm). The electron in the metal probe is approximated for a free electron gas as represented by a sinusoidal wave. Throughout the gap, this wave decays exponentially due to the vacuum barrier. On the right–hand side of the figure, the energy diagram of the SiO_2 layer is displayed with a bandgap 8.8eV and a localized unoccupied state that, in presence of an appropriate bias, is below the Fermi level of the electron gas, and can be occupied through an electron tunnel transition from the metal probe. 18

2.4 Band–diagram of a metal probe/gap/silicondioxide system illustrating how electron tunneling to and from localized states in silicondioxide depends on the applied probe bias. (Left panel) When a negative bias is applied to the tip, the Fermi energy of the metal probe rises above the unoccupied state in the dielectric and electrons in the probe will tunnel into empty states in the dielectric. (Right panel) Under positive bias conditions, the probe Fermi energy is lowered and any occupied state in the dielectric that is within the probe–tunneling rage will eventually lose its occupation. 19

2.5 [Adapted from Payne et al.,[49] and partially modified] Illustration of an SSTFM consisting of a scanning probe setup that includes a cantilever with a single paramagnetic state at its tip and a magnetic resonance setup (RF and DC magnetic field coils). 23

2.6 [Adapted from Payne et al.,[49] and partially modified] Illustrations of three possible charge and spin configurations of the probe spin/test spin pair when an energetic resonance and a spatial proximity is given. Top, left: A spin pair with mixed permutation symmetry allows for tunneling of the electron but also spin relaxation which turns the pair into a pure triplet state. Right: Tunneling creates a doubly occupied diamagnetic singlet state and a single elementary charge transfer which results in a cantilever frequency shift. The singlet state is maintained until one of the two electrons tunnels back into the probe. Bottom, left: When the spin pair exhibits high triplet content, Pauli blockade prohibits tunneling but spin relaxation allows for spin transitions into states with singlet content. 24

2.7 [Adapted from Payne et al.,[49]] Simulation of the spin-dependent tunneling noise and its power spectral density. (a) Simulation of the tunneling induced RTS noise transient due to spin–dependent tunneling between a paramagnetic probe state (the so–called probe spin) and a test spin at the sample surface for the absence (red) and presence (blue) of magnetic resonance conditions. The details on the simulation was described by Payne et al. [49]. (b,c) Plots of the tunneling charge power spectral density obtained from the simulations when magnetic resonance is absent (b) and present (c). The spectral noise density at lower frequencies displays a significant reduction under magnetic resonance. 26

2.8 [Adapted from Payne et al.,[49]] Simulation of the tunneling charge noise RMS for various bandwidths and as functions of the applied radio frequency (RF). (a) Simulated frequency shift noise (RMS) caused by tunneling induced RTS noise in presence (blue) and absence (red) of magnetic resonance and the measured system frequency shift noise (black) connected by a guide to the eye (black lines). All data were obtained for four different cantilever–to–tip distances. (b) Simulations of the total frequency shift noise (RMS) consisting of the telegraph–noise signal as well as experimentally determined system–noise levels as functions of the applied RF frequency for three bandwidth regimes. For the assumed constant magnetic field of 5mT, the RF frequency range covers the $g = 2$ electron spin resonance condition. The widths of the displayed electron spin resonance are solely governed by power broadening. The bars connected to the data points indicate the standard deviation of the fluctuation of the noise power for an assumed finite integration time of 10ms. In order to discriminate on- from off–magnetic resonance conditions needed for the single–spin detection, the on–resonance charge noise and the system noise need to be significantly lower than the off-resonance charge noise. This condition is fulfilled between ≈10 Hz and ≈1kHz bandwidth. 27

3.1 Illustration of the SSTFM concept as outlined in detail by Payne et al. [27]. (a) Illustration of the setup which includes mutually perpendicular coils that allow the generation of static and oscillating magnetic fields B_0 and B_1, respectively, for low–magnetic field magnetic resonance and a force detector with a dielectric tip that has a highly localized probe spin close to its apex. Payne et al. have proposed SiO_2 as dielectric tip material and the E' center therein as probe spin. (b) and (c) illustrate that the density of the randomly generated E' centers in the amorphous SiO_2 layer must be high enough such that an E' center is likely to be located within a minimal distance d of the tip apex such that enough exchange between probe spin and test spins can be established by tip positioning such that significant spin–dependent tunneling rates are possible. 38

3.2 Plots of X-Band EPR spectra of 60mm x 3mm x 0.3mm large ^{31}P doped c-Si(111) samples measured at a temperature T = 20K with a field modulation frequency f = 10kHz, a modulation amplitude of 0.1mT, and a weak microwave power of 4μW to avoid saturation. The samples had 60nm thin layers of thermally grown SiO_2. The black data points represent measurements of the as prepared thermal oxide. The blue data points show a measurements under identical conditions after the sample was been exposed to an argon ion plasma for 5 minutes. 43

3.3 Distribution of the E' center density as a function of the oxide thickness. (a) Plot of the measured E' center area density as a function of the different oxide thicknesses and an offset–free linear fit (red line). The agreement of the measured data and the linear fit indicates that the observed paramagnetic defects created by the Ar^+ plasma are bulk defects. (b) Plots of the EPR spectra measured on SiO_2 samples that have been exposed for different durations to dilute HF. The remaining oxide thickness on each sample was measured by ellipsometry. 45

3.4 Decay of E' center density as a function of thermal annealing temperature. (a) Integrated lock–in detected cw EPR spectra measured after different annealing temperatures (black lines) and fit of the data with three Gaussian peaks. The density of the E' centers decreases with temperature and at 290°C, it is reduced by an order of magnitude. (b) Plot of the E' center densities obtained from the fit results displayed in (a) as a function of the temperature. (c) Arrhenius plot of the density loss, the difference of the room temperature sample, and the annealed samples as a function of the anneal temperature. The fit with an Arrhenius function reveals a resonable agreement and a defect anneal activation energy of 0.176(1)eV. 46

3.5 EPR spectra of high E' center density SiO_2 films measured before (black data) and after (red data) a one hour exposure with UV light (a) and visible light (b). Both photo–bleaching experiments show that the light exposure leads to a reduction of the E' center densities. However, this effect is significantly stronger for UV light exposure. 47

3.6 Plot of EPR measured E' center densities of an SiO_2 layer after plasma treatment over the course of approximately five weeks. A gradual decline of the density is observed. However, the decay is slow enough such that even after about five weeks, the absolute volume density still exceeds 10^{18}cm^{-3}. 49

3.7 Plot of the measured transverse E' center spin relaxation rate coefficients T_2^{-1} and their error margins as a function of the inverse temperature. The red line represents a fit with an Arrhenius function. The inset displays a sketch of the Hahn–spin echo sequence that was used to measure T_2 as well as a plot of the measured Hahn–echo intensity as a function of the pulse separation time τ for T = 5K and T = 10K, with the plots of fits of these data sets with exponential decay functions. Within the given error margins, no temperature dependence of the T_2 relaxation is observed. 50

3.8 Plot of the measured longitudinal E' center spin relaxation rate coefficients T_1^{-1} and their error margins as a function of the inverse temperature. The red line represented a fit with an Arrhenius function. The dashed line indicates the room temperature value of T_1 that is extrapolated from the measurements conducted at lower temperatures. The inset displays a sketch of the inversion recovery pulse sequence that was used to measure T_1 as well as a plot of the Hahn-echo intensity as a function of the inversion delay time t for T = 5K, T = 10K, and T = 15K as well as plots of the fit results with exponential recovery functions. 51

4.1 Illustration of the experimental setup. (a) Sketch of the experimental setup which combines a scanning probe system with organic semiconductor based magnetic resonance magnetometry. The experiment was based on a low–temperature, ultra–high–vacuum scanning probe setup built by Omicron Nanotechnology GmbH (now ScientaOmicron), controlled by a customized LabView software. The inset described the stack of organic and metal layer used for the generation of spin–dependent currents. (b) Image of the superconducting magnet. (c) Image of the RF coil attached to the sample plate. (d) Image of the sensors and the red box represent the active measurement area. 62

4.2 Low–temperature scanning probe setup using quartz tuning fork cantilever. The cantilever is glued to an electrically insulating ceramic substrate which in turn is glued to a metal magnetic tip holder. A layer of gold is located on the side of the cantilever in order to collect all the piezo electric charge while the cantilever oscillates vertically. The permanent magnet attached to the scanner keeps the tip holder in place and facilitates the electrical connection to the tip that is needed for the bias application. 63

4.3 Illustration of the low–temperature scanning probe microscope and superconducting magnet with RF coil. (a) Image of the UHV-AFM low–temperature q-plus sensor system. (b) Image of the superconducting magnet above the sample that is used to produce the static magnetic field that is needed to establish magnetic resonance. (c) Image of the four-contact sample plate with a small RF coil added next to the sample for RF excitation . . . 64

4.4 Lock-in detected derivative functions of ΔI as functions of I_a, recorded for various RF frequencies between 70MHz and 175MHz. The applied DC current I_a was superimposed with a harmonic AC current with amplitude $I_m = 25$ mA in order to generate both a static magnetic field and a small modulation needed for lock-in detection. The modulation frequency $f = 30$Hz while $I_m = 25$mA. The inset represents the forward curves of the probed organic thin–film patches. The operating bias of the sensor layer for all measurements was kept consistently at a voltage $V = 9$V. . . . 66

4.5 Determination of the offset magnetic field and its direction. (a) Plot of B_n^2 as a function of the on–resonance coil current I_a for the different RF excitation frequencies ν displayed in Fig. 4.4. The red line represents a fit of the data with Eq. (1). The green lines indicate the strength of the offset magnetic field $B_0^{\perp}$ in absence of a coil current ($I_a = 0$). The inset sketch illustrates and defines the different magnetic field contributions and its relative orientation to the RF field. Note that $\vec{B}_a$ is oriented such that it lies fully within the detection plane defined by the direction of $\vec{B}_1$. (b) Plot of the lock–in detected derivative function of the current change for a fixed RF frequency ν =90 MHz after I_a was swept with a positive and negative domain. The shifts of the baselines $\pm\delta I$ are cause by the nonvanishing slope of the current change due to organic magnetoresistance [12]. This finite slope is confirmed the measurement of the $\Delta I(I_a)$ that is plotted in (c). The fit results displayed in (a) reveal that the smallest achievable value of B_n is 0.78(1)mT occuring when $B_0^{\perp}$ is maximally compensated and the magnetocurrent ΔI reaches a minimum. . . . 68

4.6 Plots of α (a), $B_0^{\perp}$ (b), θ (c), B_0^x (d), and B_0^y (e) as functions of the $\hat{x}$- and $\hat{x}$-coordinates within a 1.5mm x 0.9mm large area of the sample plane. The solid line represent guides to the eyes. The data allow the determination of magnetic field gradients of both $B_0^{\perp}$ as well as B_a (through α and the applied coil current I_a. . . . 70

5.1 Schematic of the low-temperature current imaging experiment conducted on a phosphorus doped silicon substrate. (a) A quartz tuning fork (qPlus sensor) with a Pt tip attached oscillates at $f_0 \approx 30$ kHz. When a bias V is applied to the probe, electrons tunnel from highly localized silicon dangling bond (blue ellipsoids) into the Pt tip. Due to high density of P dopants (indicated by green spheres), the substrate allows for percolation (path indicated by yellow halo) of charges through the bulk. Thus, recharging of the emptied dangling bond state through recombination is possible from a nearby P atom if the donor-dangling bond proximity permits. (b) Current map of a P doped, flash cleaned c-Si substrate without any silicon dioxide at 4.3K in darkness. The bright patches represent the spatial distribution of charge percolation endpoints indicating electronic states consistent with the localization and density of P donor atoms. (c) AFM topography image taken simultaneously using the interaction between surface and probe. The individual step edges are resolved. Note the absence of correlation between the current map and the surface topography. We also note that this AFM topography image displays a very weak, albeit recognizable ghost image in the upper right corner of the imaged area. (d) Line profile of one patch as indicated by the black line in (b). The FWHM of the Gaussian fit (red) of this patch is ≈18nm, corresponding to approximately 3 Bohr diameters of the P donor wave function. (e) High–resolution image of the area indicated by the yellow box in (b). A distinct, seemingly random fine structure for some of the patches attributed to the P donors is visible. 77

5.2 Conduction AFM images of c-Si samples with different P surface and bulk concentrations prepared by ion implantation. (a) [P] = $5\text{x}10^{14}$ cm^{-3}. No recognizable current maxima with significance above the noise level are observed. (b) [P] =$3\text{x}10^{17}$ cm^{-3}. Current maxima with areal density of about $4\text{x}10^{10}$ patches/cm^2 are observed. (c) [P] = $5\text{x}10^{18}$ cm^{-3}. Current maxima with a high areal density $2\text{x}10^{11}$ cm^{-2} are observed, compared to sample studied in (b). The observed densities of the patches fluctuate within a 12% range for different locations of the same sample, consistent with stochastic fluctuations expected from the given samples sizes. 80

5.3 Comparison of conduction AFM and STM images of c-Si surface. (a) to (c): Conduction AFM images of c-Si surfaces acquired in darkness at 4.3K. Applied tip voltage is 1.3V for panels (a) to (c). (d) to (f): STM topography images acquired under illumination at 2V tip voltage, corresponding to the areas shown in (a) to (c), respectively. The broad (≈30nm) 'patches' seen in (a) to (c) do not correlate with the STM topography of the surfaces displayed in (d) to (f), respectively. (b), (c), (e), and (f) are the high–resolution images taken in the respective black and yellow box regions shown in (a), (b), (d) and (e), respectively. . . . 82

5.4 Comparison of 100x100nm conduction AFM and STM image combinations taken on different samples taken from the same wafer. All images were acquired on samples from the same wafer under nominally identical measurement conditions. The top row displays conduction AFM images; the bottom row displays STM images at locations corresponding to the respective images in the top row. The STM images reveal that all three surfaces have different atomic scale structure and display different surface point defect densities. This variation is due to the fact that the three samples were flash annealed separately. The locations of the large current patches do not correlate with the terrace steps observed in the STM images. 83

5.5 STM images and conduction AFM images of a surface of a P–doped c-Si crystal right after a flash anneal (a,b) and after one day (c,d). Initially, the surface has very few defects apart from step edges (a). After a day, the surface has more defects present (c). (b) A dark conduction AFM image taken at the same location and shortly after image (a). It shows that current maxima occur only at a few point-like defects which exist at the surface and at step edges. (c) After a day, a higher defect density has developed and now the P-donor patches appear in the conduction AFM image (d). 84

5.6 Conduction AFM image on a thin SiO_2 layer grown on top of a P–doped Si substrate. (a) Current map obtained from the P–doped c-Si substrate in darkness at 4.3K after a thin SiO_2 film was grown. Large (>20nm) patches surrounded by low-current regions still exist, yet the fine structure of these patches is significantly more isolated. Overall, the measured current densities are lower as seen in (b), which represents an current map with higher scanning resolution obtained on the subarea of (a) marked by the yellow square. (c) Imaged zoomed into the subarea marked by a white square in (b). (d) Plot of the current marked in (c) by the red line as a function of lateral position. The displayed individual current maximum has a full width at half maximum of about 6Å. 87

5.7 Conduction AFM images of P–doped ([P]$\approx 10^{17}$cm^{-3} to 10^{18}cm^{-3}) c-Si surfaces with thin native oxide layers at 4.3K without light illumination. Panels (a) to (c) and (d) to (f) represent data sets collected at two different locations. Panel (a) and (d) both contain areas where patch-like clusters of local current maxima are observed while other areas show few localized current maxima. The local current maxima are due to highly localized electronic states in the oxide or at the c-Si oxide interface which are in electronic contact with nearby phosphorus atoms. They are attributed to silicon dangling bond states. Panels (b) and (e) are high–resolution images taken from samples areas indicated by the yellow squares in panels (a) and (d), respectively. Panels (c) and (f) display line profiles of the local current maxima taken in the regions highlighted by the lines in panels (b) and (e), respectively. The widths of these local current maxima are indicative for the strong localization of dangling bond states. 88

5.8 Different types of I-V curves and their distribution. (a) to (d) display samples of four qualitatively different types of I-V curves of more than 800 measured different I-V curves acquired on SiO_2 covered Si(100) surfaces. (a) I-V curve with a single flat plateau region; (b) I-V curve without plateau as expected from a macroscopic silicon to platinum Schottky diode; (c) I-V curve with tilted plateau which consists of a local maximum followed by a local minimum; (d) I-V curve with double plateau. (e) Bar diagrams indicating the actual number of qualitatively distinct I-V curves shown in (a) to (d) based on the acquired data. The error bars represent the square root of the actual number. (f) Energy diagram of the doped silicon sample and tip including donor state and the interface dangling bond state (Pb center). (g) Histograms of the plateau-onset (brown) and -end (green) voltages of the 415 plateaus from data sets of I-V curves that display a single flat plateau similar to the data seen in (b). (h) Histogram (blue data) displaying the plateau widths of the given data sets (difference between plateau-onset and end voltage of each curve) as well as the fit (orange line) with a two Gaussian functions (black lines). The good agreement indicates that there are at least two qualitatively different types of highly localized interface states responsible for the local current maxima at the surface. The two Gaussian functions are centered at 300(5) mV and 420(19) mV. 90

5.9 Repetition of current-voltage (I-V) measurements using conduction AFM for two randomly chosen surface locations 'Defect-1' and 'Defect-2'. While the two locations display different I-V characteristics, they display very reproducible characteristics for each location. Each curve has identical vertical axes. Since the curves are offset along the vertical axis, no vertical axis level is printed in the plot. 92

5.10 Plots of I-V curves measured under nominally identical conditions at various locations of one sample. Each column of the figure represents four measurements performed at locations within a proximity of a few hundred micrometers. While all measured I-V functions are quantitatively different, measurements conducted at each location could be categorized into four qualitatively different sets of curves as discussed in the main text. The double plateau curve shown in the fourth row has been consistently rare (< 4% of all measurements). 93

6.1 Illustration of the experimental setup. (a) The force sensor based on a quartz tuning fork oscillator with sharp Pt probe is oscillating at resonant frequency (f_0=30kHz) at a fixed oscillation amplitude of ≈1 nm. The sample surface consists of 10nm thick SiO_2 film grown on a highly doped crystalline (100) silicon wafer. A DC voltage source was connected between probe and substrate to control the tip bias. Tunneling took place between localized electronic states in the SiO_2 layer (indicated by green spheres). (b) Band diagram of the experiment at positive and negative applied bias. At negative bias, the Fermi energy of the Pt probe is above the energy level of the localized state and an electron can tunnel into the empty state (orange arrow). At positive bias, the Fermi energy of the tip is below the localized energy level and the electron tunnels out (orange arrow). 101

6.2 Cantilever frequency shift curve as a function of tip-to-surface gap and bias voltage. (a) Plot of measured cantilever frequency shift $\Delta f(d)$ as a function of the cantilever tip–to–surface distance d for decreasing d (the probe moved towards the surface) with bias $V = -4$V applied between tip and the sample. A single electron tunneling event is observed when an offest of the frequency shift appears due to the electrostatic force change caused by the single electron transition. The blue bar represents the calculated offset to Δf based on Ref. [27] for the Q-plus cantilever assuming a spring constant $k = 1200\text{Nm}^{-1}$ and oscillation amplitude of 1nm, a tip radius of 12nm, and an SiO_2 film thickness of 10nm. (b) Measurements of the cantilever frequency shift $\Delta f(V)$ as a function of the DC bias voltage V for positive (black) and negative (blue) sweeps while the tip position (laterally and vertically) remains unchanged relative to the SiO_2 surface. Single electron tunneling events are observed around $V \approx -3.6$V, with a hysteresis that is highlighted by the inset plot (c) that shows the same data as (b) on magnified scales. 104

6.3 RTS at different tip-to-sample gap and corresponding histogram and noise spectra. (a) RTS signal with metal tip and a dielectric sample at different tip-sample gaps at 77K in darkness. The extra noise in Δf is due to a single electron shuttling back-and-forth between probe and sample. At smaller gap, the shuttling rate is very high which leads to the unresolved step and while tip–sample gap increased, the rate goes down which results in a step like Δf. (b) Histograms of the frequency shift data with 10mHz bin size. The histograms show the relative amount of time the electron spends in the tip and trap state as a function of height. It also reveals the discrete nature (bimodal) of electron tunneling. Two discrete peaks confirms that there is only one electron shuttling back-and-forth between tip and sample. The two peaks in the smallest gap are smeared due to the finite bandwidth in the detection system. (c) Plot of the square of Fast Fourier Transforms of the RTS signal. The higher frequency components at smaller tip-sample gap compared to lower frequency component at larger tip-sample gap confirms that rate of electron shuttling increased while reducing the gap. 107

6.4 Integrated RTS spectra and electron shuttling rate calculation. (a) to (d): The black data points represent the integrated RTS power spectra for different cantilever distances d obtained from the data in Fig. 6.3(c). The integration interval was 0.6Hz to 300Hz. The red lines present the result of fits with integrated Lorentzian functions centered around 0Hz. (b) Semilogarithmic plot of the Lorentzian decay width r obtained from the fit results shown in (a) to (d)) as a function of the tip–to–sample gap d. The agreement of the data with a linear fit reveals the exponential dependence of the tunneling probability on d. 109

ACKNOWLEDGMENTS

The process of getting my Ph.D. has really been an interesting experience. This has been directly related to the individuals with whom I have had the opportunity of working. They have all been world class and I would like to acknowledge them.

I want to thank my adviser Dr. Christoph Boehme for giving me a chance to do such interesting work and for always being available for discussions. On many occasions, his insight has been the reason for my rapid progress. I have learned how important keeping an open door is to the progression of a project and hope to continue the friendship and collaboration.

I would also like to thank Dr. Clayton C. Williams for the opportunity to discover new physics in such a rich and interesting field of study. I have benefited from his attention to detail and his broad scope of understanding. I want to thank him for his motivational speeches and for the excellent mentoring. I also hope to continue the friendship and collaboration.

I would like to thank Dr. Philipp Rahe for taking the time to walk me through "AFM101". I understand now how hard it can be to provide training to a new student. Your training for me will be remembered forever. The things I cherish most about our collaboration have been the off-the-cuff conversations and your patience and expertise that you showed every time we have had a discussion. I feel lucky to have had you around.

I would furthermore like to thank all members of the Williams' and Boehme Groups for their help that they have always provided.

Last but not the least, I would like to thank my Mom, my Dad, and my sister who have always encouraged me to better myself and who have been very supportive throughout my entire educational career. Also, thanks to my friends who have given meaningful advice and helped me relax during difficult times. Finally, and most importantly, I would like to thank my wife Moumita Kundu who has been my constant

companion over the last few years. She has been there through all of the ups and downs of graduate school and has been indispensable to me.

CHAPTER 1

INTRODUCTION

Due to the technological importance of point defects in semiconductor materials, their physical behavior has been investigated extensively for more than half a century. Great contributions to this research have been made by the use of magnetic resonance spectroscopy, scanning probe–based microscopy, and also optical and electrical spectroscopy techniques, all of which together have revealed a huge wealth of insights about the microscopic nature of defects, the electronic processes in which they are involved, their chemical, optical, and magnetic properties, and in particular, how all these properties affect the macroscopic physical materials behavior. The wealth of information that has been created has had a strong impact on the technological application of these defects and the resulting evolution of a global semiconductor industry which is the foundation for many modern technologies.

In spite of all the existing knowledge about point defects in semiconductors, there are still many open questions about how some of them affect macroscopic materials properties, oftentimes because these questions cannot be answered without separating the individual constituents of defect ensembles (the individual defect states) from the ensemble behavior that is typically observed with the spectroscopy of macroscopic ensembles. Moreover, next to unanswered questions about the physical behavior of point defects, an entirely new set of questions has evolved about the ability of these defects' quantum mechanical properties to be utilized for various technological applications such as new transistors [22], sensors [10, 12, 13, 27], or quantum information concepts [15]. As these new quantum device concepts aim to utilize in particular the spin–degree of freedom of both electrons in the form of charge carriers or defects states as well as nuclei that interact with charge carriers or defects in their environment through hyperfine interaction, studying the spin–properties of defect states, in particular of individual defects that are not coupled to an ensemble, has

become a widely pursued research effort [15, 31, 34, 37, 22, 24].

The systematic application of spin spectroscopy of ensembles of point defects has been conducted for more than 60 years, since first EPR experiments on donor states in silicon were demonstrated [11, 7] and about a decade after the first EPR experiments had been demonstrated [38]. By the end of the 1950s, it had become clear that the spin degree of freedom is capable of controlling electronic transitions due to spin-selection rules and researchers therefore had started to use indirect spin–detection techniques such as optically detected magnetic resonance (ODMR) [2] and eventually, electrically detected magnetic resonance (EDMR) [20] to study paramagnetic point defects. These indirect EPR–based spectroscopies are not only far superior in sensitivity compared to EPR [1] (an important aspect for materials which are prepared mostly as thin films and other quasi–2–dimensional systems) but also, they reveal insights into which paramagnetic states control optical or electrical material properties and which paramagnetic states do not [25, 9, 28, 21]. Although these indirect spectroscopy techniques are powerful for gaining insights about the different microscopic electronic processes in the investigated materials, it is sometimes nevertheless challenging to extrapolate insights gained from ensembles to those of a single defect. Therefore, the need for a single–paramagnetic point–defect spectroscopy has evolved and given the almost lattice–site localization of some defects (e.g., silicon dangling bonds at surfaces of silicon crystals [19]) this needed precision for the spatial resolution of such techniques ranges on the atomic scale. During the past 20 years, a series of successful experimental demonstrations of single–spin detection and single–spin readout [22, 36, 30] have been reported; however, the detection of a single electron spin with atomic spatial resolution has remained an unsolved challenge to date.

1.1 Finding pathways for a single–spin spectroscopy with atomic spatial resolution

A method that provides atomic scale access to electronic states at the surface of various materials systems is scanning tunneling microscopy (STM) [8, 33, 3], an imaging technique based on quantum tunneling: By measuring the quantum

mechanical tunneling current between a metallic probe (the tip) and a conducting surface as a function of the surface location, a scanning probe image can be obtained. For STM surface morphology measurements, a metal probe is continuously adjusted in height (=probe-to-sample gap, which is the distance of its tip from the surface) in order to maintain a constant tunneling probability and thus, a constant tunneling current. The electron tunneling probability depends exponentially on the gap between the tip and the sample [32]. Therefore, the strong gap dependence on the tunneling current leads to a very high vertical resolution, significantly below atomic resolution. Typical tunneling currents are in the range of pA to nA. Therefore, the direct applicability of STM to the measurement of current-voltage characteristics of localized electronic states like dopant states within a semiconductor bulk or dangling bonds in the Si/SiO_2 interface is very limited. Transitions through these surface and interface states around the $c\text{-}Si/SiO_2$ interface typically take place on the time scale of hundreds of ns to hundreds of μs. Moreover, the reliance of the spatial precision of STM on constant currents makes STM nearly inapplicable to materials with low or nearly zero conductivity.

The limitations of STM with regard to the characterization of nonconductive surfaces were among the main driving forces behind the invention and the development of Atomic Force Microscopy (AFM). AFM is based on the measurement of forces and force gradients between a scanning probe tip and a sample surface. By using micromechanical oscillators, the sensitive detection of very small electromagnetic forces between atoms of a scanning probe tip and atoms within the scanned surface becomes possible. A surface morphology image of a solid sample surface can then be obtained when the probe is scanned laterally across a selected surface area while the probe height is adjusted in order to keep the force constant. There are two modes in which the traditional AFM is typically conducted: The contact–mode AFM, where the repulsive force between the probe and the sample are used, while in non-contact mode AFM, both the electrostatic and the attractive force between the probe and the surface are used. Since AFM is based on the detection of force, it has, in contrast to STM, the advantage that it can produce atomically resolved surface morphology images without the need for an electrical current. However, also compared to STM,

it also has the disadvantage that it does not produce information about the electronic properties of the scanned surface and it also does not reveal information about current percolation or the presence of localized electronic states on or beneath the surface.

In recent years, there have been more and more reports of hybrid scanning probe techniques utilizing current measurements and force measurement in different or combined ways [29, 23, 18, 33, 14, 35, 4, 30] which have been applied not just for the microscopy of surface morphologies of objects but also for the detection of electronic states [23, 18], including defect states [14, 35, 4], spin–states, or charge transitions [30, 4]. The most straightforward extension of traditional AFM and STM is conduction (c)-AFM where force detection is used in order to control a defined surface position, while a probe current is used in order to measure the surface conductivity. C-AFM is excellently suited for the measurement of microscopic lateral differences of the surface conductivity as it allows us to obtain the current–voltage (IV) characteristics as a function of the surface position. In contrast to STM, c-AFM does not suffer from small currents. When the current drops below the detection limits (typically in the sub-pA range), the position control of the probe is maintained through force measurements. As c-AFM is one of the crucial experimental methods used in the study presented in the following chapters, there will be more details on this in direct reference to the executed experiments.

Another modern hybrid scanning probe microscopy technique that has been developed over the past decade and that was used for the experiments presented in the following is single electron tunneling force microscopy (SETFM) [16, 17, 4, 5, 6, 35]. This technique was developed in order to gain access to the information such as lateral dimention (imaging), depth distribution, occupation, and spectroscopic information (the eigen–energies) of localized electronic states in nonconductive or semiconductive surfaces. It is based on the detection of single electron charge transitions between individual electronic states and metal cantilever probe using force microscopy. As force microscopy is capable to detect the minute Coulomb forces of individual electrons, SETFM allows us to observe tunneling of single electrons; it is therefore like a single–electron STM experiment (rather than a trillions-of-electrons per second STM as it is the case conventionally) and thus, it is applicable to entirely nonconducting

sample surfaces.

In the following chapter, the experimental methods will be discussed that have been the foundation for this work. This includes a more detailed discussion of EPR and other defect spectroscopy techniques. Then, the basic theory behind non-contact mode AFM and the detection scheme of SETFM, including its supporting theory, are reviewed before a recently described single–spin detection scheme that is based on SETFM is introduced which aims to combine the sensitivity of SETFM to single charge transitions with magnetic resonant control of spin–dependent transitions in order to provide an experiment that will not only be able to detect single paramagnetic defects with the spatial precision of conventional AFM and STM experiments but also allow for their energetic and spin–spectroscopies. Thus, this recently proposed single–spin tunneling force microscope [26] (SSTFM) will allow for the characterization of most relevant parameters of a defect state that characterize its physical behavior.

The central goal of the work presented in this dissertation are Chapters 3 to 6, which represent a series of studies aiming at the feasibility demonstration of experimental conditions which will allow for SSTFM. These include (i) the demonstration that a silicon dioxide layer can be prepared on the surface of a crystalline silicon scanning probe, that provides a high–enough density of localized, paramagnetic silicon dangling bond states, such that they can be utilized as probe spins for SSTFM; (ii) that a low–magnetic field (<20mT) EPR setup can be built into a low–temperature, ultra–high vacuum scanning probe microscope; (iii) that this setup can be used in order to image and identify individual phosphorus donor states as well as individual silicon dangling bond states at the interface of crystalline silicon and amorphous silicondioxide using the c-AFM technique; and (iv) that individual tunneling transitions of electrons into and out of surface states can be observed using the SETFM technique. The study concludes short of the demonstration of an SSTFM experiment. However, it lays the foundations of a future successful demonstration by demonstrating the feasibility of most of the fundamental challenges of this goal.

1.2 References

[1] W. J. Baker, K. Ambal, D. P. Waters, R. Baarda, H. Morishita, K. S. van Schooten, D. R. McCamey, J. M. Lupton, and C. Boehme. Robust absolute magnetometry with organic thin-film devices. *Nat. Commun.*, 3:898, 2012.

[2] J. Brossel, S. Geschwind, and A. L. Schawlow. Optical detection of paramagnetic resonance in crystals at low temperatures. *Phys. Rev. Lett.*, 3:548, 1959.

[3] G. W. Brown, H. Grube, and M. E. Hawley. Observation of buried phosphorus dopants near clean Si(100)-(2×1) surfaces with scanning tunneling microscopy. *Phys. Rev. B*, 70:121301, 2004.

[4] E. Bussmann, D. J. Kim, and C. C. Williams. Single-electron tunneling to insulator surfaces measured by frequency detection electrostatic force microscopy. *Appl. Phys. Lett.*, 85:2538, 2004.

[5] E. Bussmann and C. C. Williams. Single-electron tunneling force spectroscopy of an individual electronic state in a nonconducting surface. *Appl. Phys. Lett.*, 88:263108, 2006.

[6] E. B. Bussmann, N. Zheng, and C. C. Williams. Imaging of localized electronic states at a nonconducting surface by single-electron tunneling force microscopy. *Nano Lett.*, 6:2577, 2006.

[7] J. G. Castle, D. W. Feldman, P. G. Klemens, and R. A. Weeks. Electron spin$-$lattice relaxation at defect sites; E' centers in synthetic quartz at 3 kilo-Oersteds. *Phys. Rev.*, 130:577, 1963.

[8] C. J. Chen. *Introduction to Scanning Tunneling Microscopy.* New York, Oxford., 1993.

[9] C. J. Cochrane and P. M. Lenahan. Spin counting in electrically detected magnetic resonance via low-field defect state mixing. *Appl. Phys. Lett.*, 104:093503, 2014.

[10] F. Dolde, H. Fedder, M. W. Doherty, T. Nobauer, F. Rempp, G. Balasubramanian, T. Wolf, F. Reinhard, L. C. L. Hollenberg, F. Jelezko, and J. Wrachtrup. Electric-field sensing using single diamond spins. *Nat. Phys.*, 7:459, 2011.

[11] G. Feher and A. F. Kip. Electron spin resonance absorption in metals. I. experimental. *Phys. Rev.*, 98:337, 1955.

[12] M. S. Grinolds, S. Hong, P. Maletinsky, L. Luan, M. D. Lukin, R. L. Walsworth, and A. Yacoby. Nanoscale magnetic imaging of a single electron spin under ambient conditions. *Nat. Phys.*, 9:215, 2013.

[13] M. S. Grinolds, M. Warner, De. Greve, K., Y. Dovzhenko, L. Thiel, L. R. Walsworth, S. Hong, P. Maletinsky, and A. Yacoby. Subnanometre resolution in three-dimensional magnetic resonance imaging of individual dark spins. *Nat. Nano.*, 9:279, 2014.

[14] J. P. Johnson, D. W. Winslow, and C. C. Williams. Measurement of depth and energy of buried trap states in dielectric films by single electron tunneling force spectroscopy. *Appl. Phys. Lett.*, 98:052902, 2011.

[15] B. E. Kane. A silicon-based nuclear spin quantum computer. *Nature*, 393:133, 1998.

[16] L. J. Klein and C. C. Williams. Single electron tunneling detected by electrostatic force. *Appl. Phys. Lett.*, 79:1828, 2001.

[17] L. J. Klein and C. C. Williams. Single-electron tunneling to insulator surfaces detected by electrostatic force. *Appl. Phys. Lett.*, 81:4589, 2002.

[18] H. Labidi, M. Taucer, M. Rashidi, M. Koleini, L. Livadaru, J. Pitters, M. Cloutier, M. Salomons, and R. A. Wolkow. Scanning tunneling spectroscopy reveals a silicon dangling bond charge state transition. *New J. Phys.*, 17:073023, 2015.

[19] P. M. Lenahan and J. F. Conley. What can electron paramagnetic resonance tell us about the Si/SiO_2 system. *J. Vac. Sci. Technol. B*, 16:2134, 1998.

[20] R. Maxwell and A. Honig. Neutral-impurity scattering experiments in silicon with highly spin-polarized electrons. *Phys. Rev. Lett.*, 17:188, 1966.

[21] D. R. McCamey, G. W. Morley, H. A. Seipel, L. C. Brunel, J. van Tol, and C. Boehme. Spin-dependent processes at the crystalline Si-SiO_2 interface at high magnetic fields. *Phys. Rev. B*, 78:045303, 2008.

[22] A. Morello, J. J. Pla, F. A. Zwanenburg, K. W. Chan, K. Y. Tan, H. Huebl, M. Mttnen, C. D. Nugroho, C. Yang, J. A. van Donkelaar, A. D. C. Alves, D. N. Jamieson, C. C. Escott, L. C. L. Hollenberg, R. G. Clark, and A. S. Dzurak. Single-shot readout of an electron spin in silicon. *Nature*, 467:687, 2010.

[23] T. H. Nguyen, G. Mahieu, M. Berthe, B. Grandidier, C. Delerue, D. Stiévenard, and Ph. Ebert. Coulomb energy determination of a single si dangling bond. *Phys. Rev. Lett.*, 105:226404, 2010.

[24] P. Ovartchaiyapong, K. W. Lee, Bryan A. Myers, and Ania C. Bleszynski Jayich. Dynamic strain-mediated coupling of a single diamond spin to a mechanical resonator. *Nat. Commun.*, 5:1, 2014.

[25] S.-Y. Paik, S.-Y. Lee, W. J. Baker, D. R. McCamey, and C. Boehme. T_1 and T_2 spin relaxation time limitations of phosphorous donor electrons near crystalline silicon to silicon dioxide interface defects. *Phys. Rev. B*, 81:075214, 2010.

[26] A. Payne, K. Ambal, C. Boehme, and C. C. Williams. Atomic-resolution single-spin magnetic resonance detection concept based on tunneling force microscopy. *Phys. Rev. B*, 91:195433, 2015.

[27] M. Pelliccione, B. A. Myers, L. M. A. Pascal, A. Das, and A. C. Bleszynski Jayich. Two-dimensional nanoscale imaging of gadolinium spins via scanning probe relaxometry with a single spin in diamond. *Phys. Rev. Applied*, 2:054014, 2014.

[28] T. A. Pomorski, B. C. Bittel, C. J. Cochrane, P. M. Lenahan, J. Bielefeld, and S. W. King. Defects and electronic transport in hydrogenated amorphous SiC films of interest for low dielectric constant back end of the line dielectric systems. *J. Appl. Phys.*, 114:074501, 2013.

[29] B. Rezek, J. Stuchlik, A. Fejfar, and J. Kocka. Microcrystalline silicon thin films studied by atomic force microscopy with electrical current detection. *J. Appl. Phys.*, 92:587, 2002.

[30] D. Rugar, R. Budakian, H. J. Mamin, and B. W. Chui. Single spin detection by magnetic resonance force microscopy. *Nature*, 430:329, 2004.

[31] K. Saeedi, S. Simmons, J. Z. Salvail, P. Dluhy, H. Riemann, N. V. Abrosimov, P. Becker, H.-J. Pohl, J. J. L. Morton, and M. L. W. Thewalt. Room-temperature quantum bit storage exceeding 39 minutes using ionized donors in silicon-28. *Science*, 342:830, 2013.

[32] J. J. Sakurai. *Modern Quantum Mechanics*. 1993.

[33] S. R. Schofield, P. Studer, C. F. Hirjibehedin, N. J. Curson, G. Aeppli, and D. R. Bowler. Quantum engineering at the silicon surface using dangling bonds. *Nat. Commun.*, 4:1649, 2013.

[34] A. R. Stegner, C. Boehme, H. Huebl, M. Stutzmann, K. Lips, and M. S. Brandt. Electrical detection of coherent ^{31}P spin quantum states. *Nat. Phys.*, 2:835, 2006.

[35] R. Wang, S. W. King, and C. C. Williams. Atomic scale trap state characterization by dynamic tunneling force microscopy. *Appl. Phys. Lett.*, 105:052903, 2014.

[36] J. Wrachtrup, C. von Borczyskowski, J. Bernard, M. Orritt, and R. Brown. Optical detection of magnetic resonance in a single molecule. *Nature*, 363:244, 1993.

[37] M. Xiao, I. Martin, E. Yablonovitch, and H. W. Jiang. Electrical detection of the spin resonance of a single electron in a silicon field-effect transistor. *Nature*, 430:435, 2004.

[38] Z. Zavoiski. *J. Phys. USSR*, 9:211, 1945.

CHAPTER 2

EXPERIMENTAL METHODS AND RELATED TECHNIQUES

In the following, experimental methods are discussed which have either been used in the course of this study or are closely related. As this dissertation describes the study of prerequisites for single–spin magnetic resonance tunneling force microscopy, various magnetic resonance as well as scanning probe microscopy techniques are important for its implementation. The following first section of this chapter focuses on magnetic resonance spectroscopy techniques which have been important for this work, while the second section will then outline the scanning probe methods that have been employed.

2.1 Magnetic resonance spectroscopy of point defects

There are several magnetic resonance based methods that allow for the investigation of the microscopic nature of point defects in condensed matter systems, which, broadly, can be categorized into electron spin resonance (EPR) spectroscopy based and nuclear magnetic resonance (NMR) spectroscopy based approaches. The foundations of magnetic resonance spectroscopy goes back to the work of Felix Bloch who developed the theory of resonant nuclear induction [3] and carried out the first NMR experiments [4] in 1946. While this was certainly the starting point of a scientific revolution which lead to 8 Nobel Prizes and various significant breakthroughs, it must be emphasized that the first reported magnetic resonance experiment was actually an EPR measurement recorded by Zavoiski [73] in 1945. The first NMR demonstration was soon followed by a time-domain NMR experiment on coherence time scales of nuclear spins, which, for the first time, revealed effects such as spin–coherence decays,

coherent dephasing, and longitudinal spin–relaxation processes. After these initial discoveries, research and development of NMR–based methods expanded dramatically and led to the development of many applications such as for the structural analysis of chemical compounds or magnetic–resonant imaging that today is mostly applied to medical diagnostics. Due to the technologically more challenging nature of microwave radiation sources and detection electronics, the development of EPR spectroscopy occurred slower than NMR and it took until about the 1980s for EPR spectroscopy to be routinely conducted as pulsed experiment. Soon after this technological advancement, time resolved EPR spectroscopy followed the NMR spectroscopy techniques with regard to the application of complex pulse sequences needed for Fourier transform spectroscopy. Since then, both NMR and EPR have been expanded to larger and larger magnetic field and frequency ranges [53, 43, 21], concatenated [70, 68], and adiabatic [11] and increasingly, both NMR and EPR are employed in complex combinations with other spectroscopic techniques such as in double-, and triple-resonance experiments, electrically (EDMR) [39, 62, 46, 47, 52] and optically detected magnetic resonance (ODMR) [71, 26, 65, 13, 67] experiments, or in combination with scanning probe techniques. The latter development was driven mostly by the limitation of NMR and EPR – while these techniques allow access to microscopic information of point defects, they provide only limited information about the involvement of these centers in electronic processes such as trapping or recombination. In contrast, combined methods such as ODMR and EDMR, which connect EPR and NMR with other methods such as photoconductivity, luminescence, or electrical conductivity measurements, take advantage on the spin–dependency that many electronic processes possess as their transition probability is governed by spin–selection rules.

2.1.1 ODMR and EDMR

The discovery of spin–dependent recombination goes back to the first observation of ODMR made by Geschwind et al. in 1959 [22, 7]. In this experiment, the spin configuration of electronic excitations in a $Cr^{3+}INAl_2O_3$ crystal was manipulated with EPR and the resulting recombination rate change was then detected by luminescence measurements. Since ODMR is applicable in electronic transitions in both atomic and

molecular systems, it has become a widely used experimental tool for the investigation of various gaseous and condensed matter systems. Since the first demonstration of ODMR, the development of transient ODMR has progressed significantly, and due to the availability of fast and sensitive photo-detectors, this development has taken place parallel to the evolution of pulsed EPR.

EDMR is the electrical equivalent to ODMR where magnetic resonantly manipulated spin–dependent charge carrier recombination or transport rates are measured by detection of electric currents. The development of EDMR methods is closely related to ODMR and began when Maxwell and Honig [37] demonstrated EPR induced conductivity changes of a silicon crystal in 1966. Following this discovery, an extended body of work was produced that aimed to produce an understanding of this effect. Initially, the impact of EPR was attributed to spin–dependent scattering of charge carriers at impurities. Later, spin–dependent recombination based on spin–selection rules was invoked by Lepine [34] who proposed a recombination model in which spin–dependent transition rates change when magnetic resonance diminishes thermal spin–polarization of charge carriers, causing an enhancement of the singlet manifold among electron–hole pairs, which in turn leads to an enhancement of recombination. While this recombination enhancement invoked by Lepine as the origin of the EDMR signal was later confirmed by photoconductivity measurements, neither the strengths nor the predicted polarization dependencies of most observed EDMR signals followed Lepine's predictions and the physics of EDMR measurements remained not understood until Kaplan, Solomon, and Mott (KSM) created an extension of the Lepin model in 1978 that is based on intermediate pairs [31] with very weak spin–exchange and spin–dipolar interactions. Since then, most EDMR but also ODMR signals found in condensed matter systems have been found to be adequately described by the KSM process.

In contrast to time–resolved ODMR, time-resolved EDMR had not been demonstrated on the times scale of coherent spin motion. This delay of pulsed (p) EDMR was due, on one hand, to the lack of appropriate sample contact schemes that could sustain high–power microwave radiation, while on the other hand, due to the limited time resolution that most semiconductor materials would provide (in terms of the

dielectric relaxation time) for the real–time observation of spin–coherent control of spin–dependent transition rates. Only when spin–pump/ current–probe schemes for EDMR were applied, the development of pEDMR techniques followed those previously made for the pODMR and pEPR spectrocopies [5, 6, 62, 46].

Over the past 50 years, all magnetic resonance–based techniques, but in particular ODMR and EDMR, have always been applied to the study of localized states (point defects) in various inorganic [64, 30, 16, 63] and organic [39, 24] semiconductors, semiconductor heterostructures [17, 23], devices [54, 35, 44], and interfaces [61]. In the course of this process, much microscopic insight about the nature of spin–dependent recombination has been obtained. However, in spite of all this progress on gaining microscopic information about the nature of point defects as well as the electronic processes in which they are involved, most traditional magnetic resonance spectroscopy experiments have taken place on spin ensembles and the specific microscopic location of the probed defects has remained elusive. Typical sensitivity limits for the widely used X-band EPR spectroscopy are reached at ensemble sizes containing about 10^9 paramagnetic centers. ODMR and EDMR are significantly more sensitive - when applied to macroscopic electric devices or optically detected ensembles, sensitivity limits of 100 to 1000 paramagnetic centers are routinely achieved. For special defects such as the NV center [26], for quantum dots states [60, 51], single–spin transistor devices [41, 72], or using magnetic resonance force microscopy [55], even single–spin sensitivities have been demonstrated. However, all of these experiments fail to identify the location of the detected centers on atomic scales and for magnetic resonance experiments, in particular EDMR and ODMR experiments, there appears to be a tradeoff between ensemble size or spatial resolution.

2.2 Scanning probe microscopy techniques

Lack of spatial resolution has traditionally been a challenge of microscopy techniques. Microscopy, originally developed solely as an optical technique using light in the visible wavelength range, was limited by diffraction. While this could be overcome to a certain degree by utilization of radiation with shorter wavelengths, giving rise to electron microscopy and other radiation detected microscopy tech-

niques [40, 1, 58]), it was ultimately a problem which motivated the development of surface–contact and near–surface contact–microscopies which generate images by means of scanning probes. The first STM experiment was recorded by Gerd Binnig and Heinrich Rohrer at IBM Zurich [2, 15] in 1981. For this measurement, atomic resolution was achieved by sending a tunneling current from a sharp metal tip to a clean conductive surface. While this demonstration was a huge breakthrough for microscopy, it worked only for the microscopy of conductive materials. Thus, soon after STM, imaging of nonconducting surfaces was demonstrated using AFM in 1986. For AFM, the force between surface atoms of the tip and the surface are measured using a micromechanical cantilever probe. When the measured force is regulated to stay constant by adjustment of the tip–to–surface gap, high–resolution surface images [42] can be obtained by the measurement of the gap as a function of the surface location. Soon after the discovery of AFM, an entire family of scanning probe methods (scanning capacitance microscopy (SCM) [36, 32], magnetic force microscopy (MFM) [59, 55] and others) were developed in order to investigate and characterize surfaces and interfaces of various condensed matter systems. For the experiments presented in this dissertation, the following scanning–probe techniques were used.

2.2.1 Non-contact atomic force microscopy

The observable of non–contact (NC)-AFM is the frequency shift (Δf) of the cantilever resonance frequency that results from the interaction force F between the tip and the substrate. The interaction force comes from different forces, most significantly electrostatic forces and Van–der–Waals forces. The frequency shift Δf depends on the cantilever resonance frequency (f_0), the spring constant(k), and the oscillation amplitude (A) of the cantilever. For the different applications of NC-AFM, different force contributions are dominant; for instance, for the case of SETFM that is to be discussed below, the force of interaction is purely electrostatic due to the tunneling of a single electron in the presence of an electrostatic field between the tip and sample. For these experiments, a setup was used that allowed for AFM under ultra–high–vacuum (UHV) conditions with a pressure of $\approx 10^{-10}$ mBar. Fig. 2.1 shows the sketch of this UHV-AFM setup. A laser beam or a tightly focused light is directed

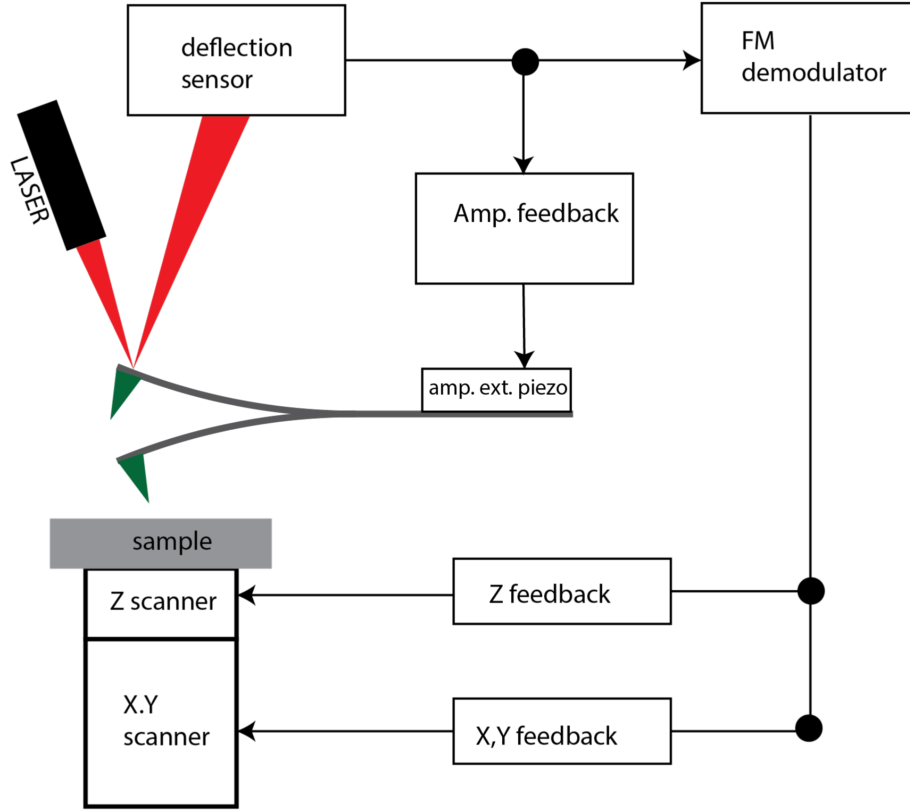

Figure 2.1. Illustration of a standard AFM setup. A micromechanical oscillating metal cantilever probe is placed above the investigated surface. A focused laser beam is incident onto the cantilever and reflected back to the detector in order to measure the cantilever oscillation. An amplitude feedback control loop maintains a constant oscillation amplitude by compensation of attenuation losses through an excitation piezo element. The frequency modulation (FM) demodulator measures the change of the cantilever resonance frequency caused by tip–sample interaction forces. The X and Y feedback control facilitates the lateral scan across the sample surface.

onto the back of the oscillating cantilever which reflects the beam and sends it to a split silicon detector capable of detecting the deflection angle and hence, oscillatory motion of the cantilever. For the force–free, uncoupled cantilever, the unperturbed oscillation is determined by its equation of motion

$$m^{*}\ddot{Z} + \frac{k}{Qw_o}\dot{Z} + kZ = F_d \tag{2.1}$$

in which $m*$ is the effective mass, k is the spring constant, Q is the quality factor, and ω_0 is the unperturbed resonance frequency of the cantilever. F_d is the externally applied driving force. An external feedback mechanism allows us to cancel out any

damping and maintain an oscillation with constant amplitude. Because of this, the equation of motion of an unperturbed cantilever simplifies to

$$m^* \ddot{Z} + kZ = 0 \tag{2.2}$$

where $Z = A\cos(\omega_0 t)$ and A is the amplitude. When the probe approaches the sample and starts to interact with the surface through a force F, the equation of motion of the cantilever is modified and becomes

$$m^* \ddot{Z} + kZ = F \tag{2.3}$$

causing the the external feedback mechanism to maintain a constant oscillation amplitude A by shifting the resonance frequency to a new value ω. Under the assumption of a small perturbation, ω is close to the unperturbed resonance frequency ω_0 and it can therefore be approximated as $\omega = \omega_0 + \Delta\omega$ with $\Delta\omega$ being the frequency shift of the cantilever resonance frequency caused by the interaction force F. Substituting $Z = A\cos(\omega t)$ in Equ. 2.3 and Equ. 2.2 yields

$$(\omega^2 - {\omega_0}^2)\cos(\omega t) = \frac{-{\omega_0}^2}{Ak} F \tag{2.4}$$

when the experimental condition that $\omega_0 >> \Delta\omega$ is assumed. Thus, $\omega^2 \cong {\omega_0}^2 + 2\omega_0\Delta\omega$ and Equ. 2.4 assumes the form

$$2\Delta\omega\cos(\omega t) = \frac{-\omega_0}{Ak} F. \tag{2.5}$$

Therefore, the average frequency shift over a cantilever oscillation period can be calculated by multiplication of both sides with $\cos(\omega t)$ and subsequent integration yielding

$$< \Delta\omega >= \frac{-\omega_0}{Ak} < F\cos(\omega t) > \tag{2.6}$$

where the time average of the right–hand side is independent of ω. Thus, substituting $\omega \rightarrow \omega_0$ into Equ. 2.6 yields

$$\Delta f = \frac{f_0}{\pi A k} \int_{-1}^{+1} \frac{F(u)u}{\sqrt{1-u^2}} du \tag{2.7}$$

where A is the cantilever oscillation amplitude, F is the interaction force between probe and sample, and $u = cos(\omega_0 t)$ is the substitution made to take the tip oscillation [42] into account. Equation 2.7 can be used to determine changes in the

probe–to–surface interaction force from the measured frequency shift when a constant oscillation amplitude is maintained. Using this approach provides a highly sensitive force detection technique that is sensitive enough to measure an electrostatic force change caused by individual elementary charge transitions (e.g., due to single–electron tunneling) between the surface and the probe or vice versa [33, 9, 10, 8].

2.2.2 Quantum tunneling and scanning tunneling microscopy

Quantum tunneling is a phenomenon where a particle moves through a potential barrier that is higher than the particles total mechanical energy [57]. Quantum tunneling has found many technological applications in various modern day applications like tunnel diodes [20] or scanning tunneling microscopy [15]. There are two very important tunneling conditions that have to be satisfied in order to make tunneling of an electron between two electronic states likely: (I) the energy of the two electronic states must be equal, within the magnitude of the thermal energy (kT). (II) The localization gap between the two electronic states must be sufficiently close such that there is significant overlap between their respective electronic wavefunctions, i.e., the exchange interaction between the two electronic states must be high such that tunneling probability, therefore the tunneling rate, is significantly higher.

2.2.3 Single–electron tunneling force microscopy

As introduced above, single–electron tunneling force microscopy (SETFM) allows for the observation of individual electron tunneling transitions between the scanning probe and the sample surface by detection of electrostatic force change caused by the elementary charge displacement. For SETFM, a metal cantilever probe is oscillated at its resonance frequency at a constant amplitude. The probe is positioned above the sample surface (see Fig. 2.2) and in close proximity of the surface using the AFM force feedback for the gap control. A DC voltage is then applied to the probe in order to raise/lower its Fermi level. When the probe is moved vertically by a few nanometers through application of a linear ramp function to the probe's Z-direction, the tunneling conditions discussed above can be fulfilled provided a localized state lies underneath the probe apex. Once an electron tunnels into or out of the localized

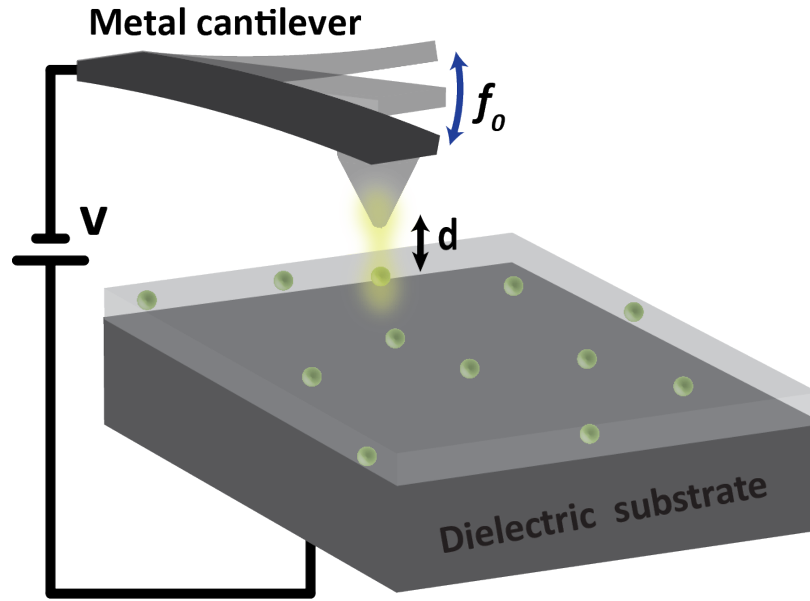

Figure 2.2. Illustration of a metal cantilever probe that is placed above a localized state within a dielectric sample surface. The cantilever is oscillating at its resonance frequency f_0. A negative bias is applied to the metal probe and its Fermi energy is raised. The probe height is then ramped vertically up and down by a few nm. When the tunneling conditions are fulfilled, electron will tunnel from the metal probe to a defect state or vice versa and an electrostatic force change will introduce an abrupt frequency change of the cantilever.

surface state, a change of the local electrostatic force causes a detectable cantilever frequency shift Δf [33, 9].

2.2.3.1 Tunneling between a metal probe and a dielectric substrate

For the theoretical prediction of tunneling rates as needed for the description of tunneling microscopy experiments presented in the following chapters, textbook quantum mechanics [57] is applied to a tip–sample model system, for which the electrons in the tip are assumed to be delocalized in a Fermi sea and in which all states below the Fermi energy are occupied. The trap states in the dielectric are assumed to be localized in a square well potential. The energy band-diagram for the tunneling case is shown in Fig. 2.3. Quantitative details of this approach are described by N. Zheng et al. [74] which confirms that the tunneling probability and thus the tunneling rate from the metal probe to the localized state depends exponentially on the physical gap between tip and sample surfaces. For the given parameters, the

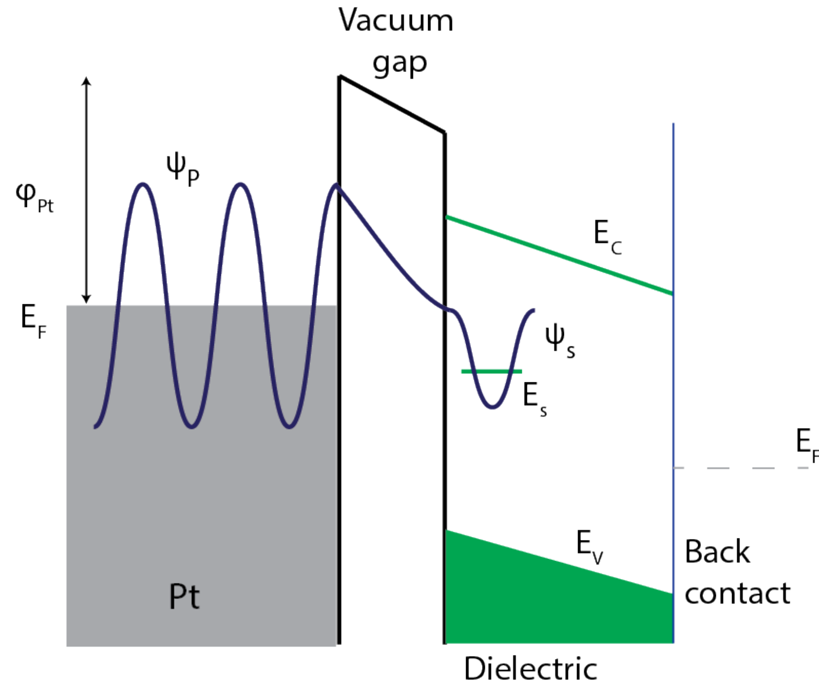

Figure 2.3. Illustration of an electron wavefunction within the energy band diagram of a metal probe–to–sample system with a localized state in surface proximity. Tunneling of an electron from the metal probe to the localized electronic state in the dielectric surface becomes likely for a sufficiently small gap (<2nm). The electron in the metal probe is approximated for a free electron gas as represented by a sinusoidal wave. Throughout the gap, this wave decays exponentially due to the vacuum barrier. On the right–hand side of the figure, the energy diagram of the SiO_2 layer is displayed with a bandgap 8.8eV and a localized unoccupied state that, in presence of an appropriate bias, is below the Fermi level of the electron gas, and can be occupied through an electron tunnel transition from the metal probe.

electron–tunneling probability drops to almost zero within a gap size of ≈2nm and states beyond 2nm are essentially out of the tunneling domain. For SETFM as for STM, it is the confinement of significant tunneling probabilities to small gap distances which allow imaging of localized states with atomic spatial resolution.

2.2.3.2 Tunneling spectroscopy

SETFM is not only capable to image localized states, it can also provide access to the eigenenergies of near surface defect states. Single–electron tunneling force spectroscopy (SETFS) [27, 66] is conducted by observation of tunneling transition probabilities as a function of the applied probe bias. In order to illustrate this approach, an energy band–diagram is shown in Fig. 2.4. The Fermi gas in the metal

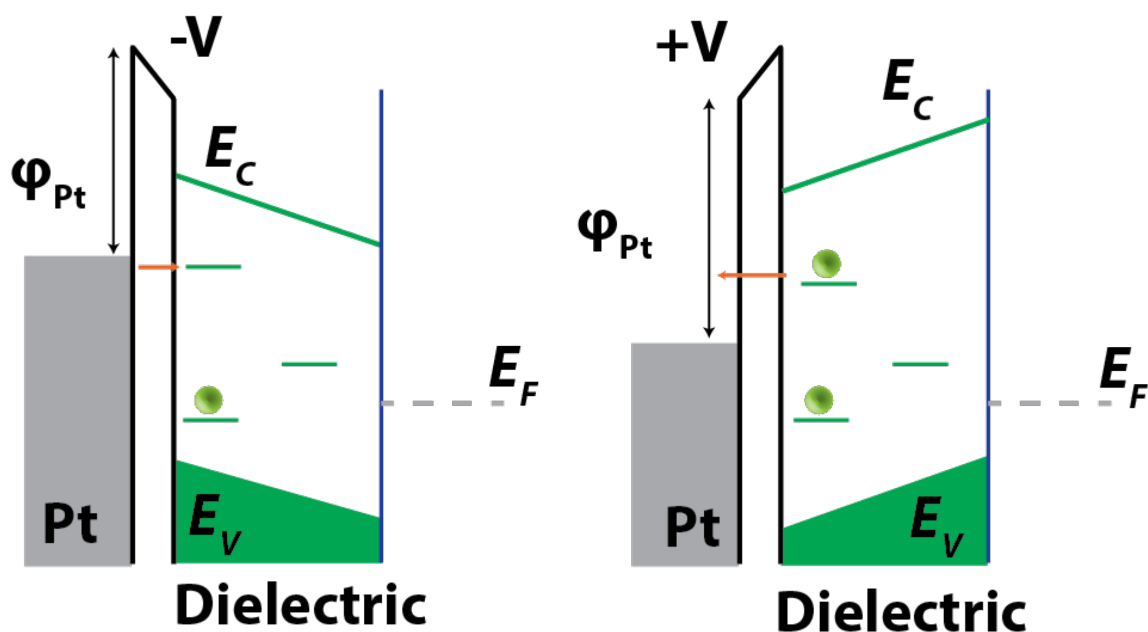

Figure 2.4. Band–diagram of a metal probe/gap/silicondioxide system illustrating how electron tunneling to and from localized states in silicondioxide depends on the applied probe bias. (Left panel) When a negative bias is applied to the tip, the Fermi energy of the metal probe rises above the unoccupied state in the dielectric and electrons in the probe will tunnel into empty states in the dielectric. (Right panel) Under positive bias conditions, the probe Fermi energy is lowered and any occupied state in the dielectric that is within the probe–tunneling rage will eventually lose its occupation.

tip is represented by the gray area on the left side while the right side represents the dielectric SiO_2 substrate with a band gap of 8.8eV. A constant DC bias is applied to the tip with respect to the metallic back contact of the SiO_2 substrate. When this bias is negative (left panel), the Fermi energy of the probe increases relative to the defect states in the dielectric. Note that the applied bias voltage drops across both vacuum gap between the probe and the surface as well as across the dielectric substrate. If there is an empty electronic state in the SiO_2 below the Fermi energy of the metal probe and the gap is small enough, then an electron will eventually tunnel and occupy the state as shown in Fig. 2.4 (left). When a positive bias is applied to the probe, the Fermi energy of the probe is lowered with respect to the dielectric substrate and the occupied electronic states above the Fermi energy are eventually emptied (see the right panel of Fig. 2.4). Therefore, by applying a voltage ramp

to the probe for a known tip–surface gap, the energy of the localized states can be measured [27, 69, 66]. Further discussion of this defect spectroscopy approach is given in Chapter 6.

In conclusion, SETFM is a powerful tool which allows us imaging and spectroscopy of individual localized electronic states and this allows us to identify point defects with atomic scale spatial resolution in nonconductive substrates. Using SETFM, spatial and energy distributions of defects can be measured. However, the chemical identity (g factor) of defects, as obtained from magnetic resonance spectroscopy, or the identification of the spin–manifold of a defect cannot be obtained with this method. Therefore, as discussed in the following section, a new scanning probe technique has been proposed that aims to combine SETFM and magnetic resonance spectroscopy, such that the spin of a single localized electron state cannot only be detected but also characterized.

2.3 Single–spin magnetic resonance tunneling force microscopy with atomic resolution

The detection and the readout of spin–states of paramagnetic point defects in semiconductors is currently a strongly pursued research area, not just because of its significance for understanding electronic processes and their influence on electronic materials properties, but also because point defects in condensed matter systems, in particular paramagnetic impurities, are currently the most coherent quantum bit (qubit) implementations that are found in nature [56]. However, for both defect spectroscopy as well as for using these systems for quantum applications, the availability of single–spin detection and readout schemes as well as atomic scale spatial resolution that allows to discriminate between adjacent point defects is a crucial requirement. It is well known from electrically detected magnetic resonance (EDMR) spectroscopy [62, 46, 47, 52, 25] that electron tunneling and recombination transitions at or within silicon dioxide layers are strongly dependent on spin–selection rules [38].

As explained in the last section, it has also been demonstrated that single–electron tunneling can be detected by measuring the electrostatic force with sub-nanometer spatial resolution [33, 9, 28]. Therefore, a scanning probe–based single–spin detection scheme based on electrostatic force detection of single electronic charges using spin–

selection rules was proposed by Payne et al. [49]. This approach has the potential to achieve better sensitivity for single–electron spins than the existing magnetic–force based single–spin microscopy [55] since electrostatic forces are many orders of magnitude larger than magnetic dipolar forces. This method, referred to in the following as single–spin tunneling force microscopy (SSTFM), is based on bringing a paramagnetic state in a dielectric AFM probe tip within the tunneling range of a paramagnetic state in a dielectric surface under appropriate energetic conditions (the two states must be in resonance). When one of the unpaired electrons can randomly tunnel between the two states, a change of the local electrostatic force can be detected as a random telegraph signal (RTS) on the AFM cantilever frequency shift (Δf). Under magnetic resonance of one of the two paramagnetic states, the tunneling rate dynamics will then be modified and a change of the tunneling dynamics can cause a change of the magnitude of the RTS noise power for a finite bandwidth. As quantum tunneling is not directly dependent on temperature, this method is expected to be applicable over a wide temperature range and for a wide range of paramagnetic defect states.

2.3.1 Spin–selection rule based single–spin detection

Several single–spin detection concepts utilizing spin–selection rules have been developed in the past [41, 19, 72, 60, 29]. Some of these methods have already been demonstrated experimentally, including for point defects in silicon [41, 72], diamond [50], and for single– electron spins in charge quantum dots [19, 60]. The core idea behind of all of these techniques is to use the Pauli–spin blockade in order to convert a spin–state into an electronic charge state. Usually, this spin–to-charge conversion is based on bringing a test spin and a probe spin in sufficiently close proximity such that the two adjacent paramagnetic states can undergo a transition into a doubly occupied diamagnetic singlet state. If the host system is weakly spin-orbit coupled, the probability of this transition will depend strongly on the permutation symmetry of the spin pair before the transition; in a more classical sense, it depends on the relative orientation of the two spins. A spin detection of the test spin can therefore be performed by measuring the spin–controlled charge transfer.

The detection of individual elementary charges can be achieved with the SETFM experiment [33, 9] described above. SETFM allows us to determine the change of local electrostatic force due to an individual electron movement from or to the cantilever to the substrate. When an individual elementary charge moves from or into a probe state, and therefore into or from a surface state, the change in local electrostatic force gradient causes a change in the cantilever resonance frequency.

2.3.2 The experimental setup for SSTFM

SSTFM combines SETFM with magnetic resonance spectroscopy, and therefore, an experimental setup is needed as conceptually illustrated in Fig. 2.5 and described by Payne et al. [49] in detail. The basic platform of this instrument is a commercially available ultra–high–vacuum (UHV) AFM instrument. The cantilever used for SSTFM must be made out of a weakly spin–orbit coupled material (e.g., SiO_2, Silicon, etc.) and it will host the single paramagnetic state (probe/test spin) from which spin–dependent tunneling occurs into the test state. Two mutually perpendicular magnetic field coils for the generation of the static magnetic field B_0 and the oscillating magnetic field B_1 are added to the system as needed to establish magnetic resonance conditions. The cantilever is driven by a piezo element in order to continuously oscillate at a constant oscillation amplitude and a resonance frequency f_0. Since the paramagnetic centers in SiO_2 have positive correlation energies around $\approx$1eV [45, 48], it is necessary to shift the energy level of the test spin and the probe spin with respect to each other in order to establish the resonance condition for tunneling. Therefore, a constant voltage (V) is applied between the back contact of the substrate and the probe such that the two paramagnetic centers become energetically aligned. Using a height control, the probe will be brought in proximity of the substrate and if the probe spin and the test spin align spatially, electron tunneling will occur between the two states. This shuttling of a single elementary charge will be detectable by monitoring the resonance frequency of the cantilever.

2.3.3 The measurement principle behind SSTFM

Figure 2.6 displays an illustration of three possible spin and charge occupation scenarios which can occur when the probe spin is brought within the tunneling range

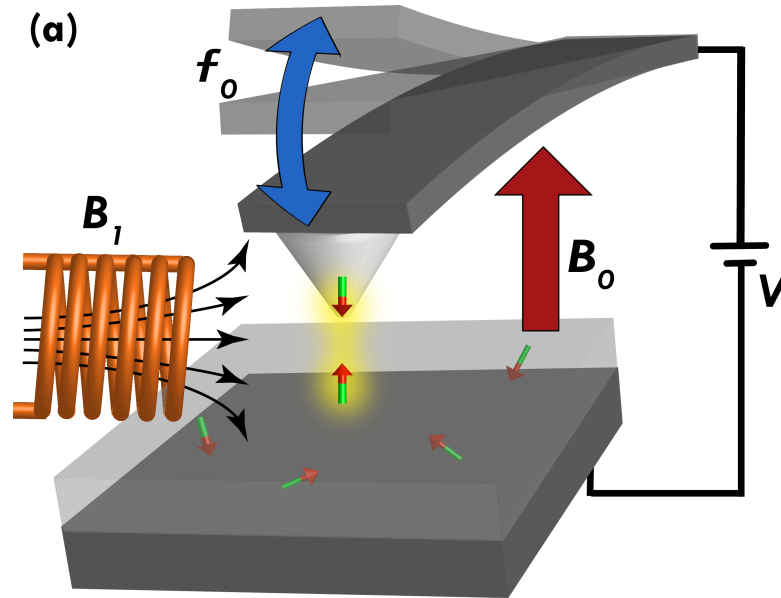

Figure 2.5. [Adapted from Payne et al.,[49] and partially modified] Illustration of an SSTFM consisting of a scanning probe setup that includes a cantilever with a single paramagnetic state at its tip and a magnetic resonance setup (RF and DC magnetic field coils).

of the test spin. When the spin pair state of the two paramagnetic centers has high permutation symmetry (high triplet content) the Pauli blockade caused by the weak spin-orbit coupling quenches the electron tunneling probability between the tip and the substrate. In contrast, when the two centers form a pair with a high degree of permutation antisymmetry (high singlet content) the tunneling probability is high and randomly occurring tunneling events can be observed as a random telegraph signal (RTS) on the shifted cantilever resonance frequency due to the local electrostatic force change. The orientation of either one of these two weakly coupled spin centers can abruptly change due to spin–lattice relaxation with a relaxation probability T_1^{-1} where T_1 is the longitudinal spin relaxation time. Therefore, as long as the two electrons in the probe state and the test state are separated, the tunneling probability is actually modulated by the randomly changing longitudinal spin–relaxation events. Given the rate diagram in Fig. 2.6, there are three possible spin permutation symmetry configurations that this electron pair of paramagnetic centers can assume, namely (1) a pure singlet configuration when two electrons occupy one state, (2) a triplet configuration when the two electrons are separated, and (3) a mixed symmetry state

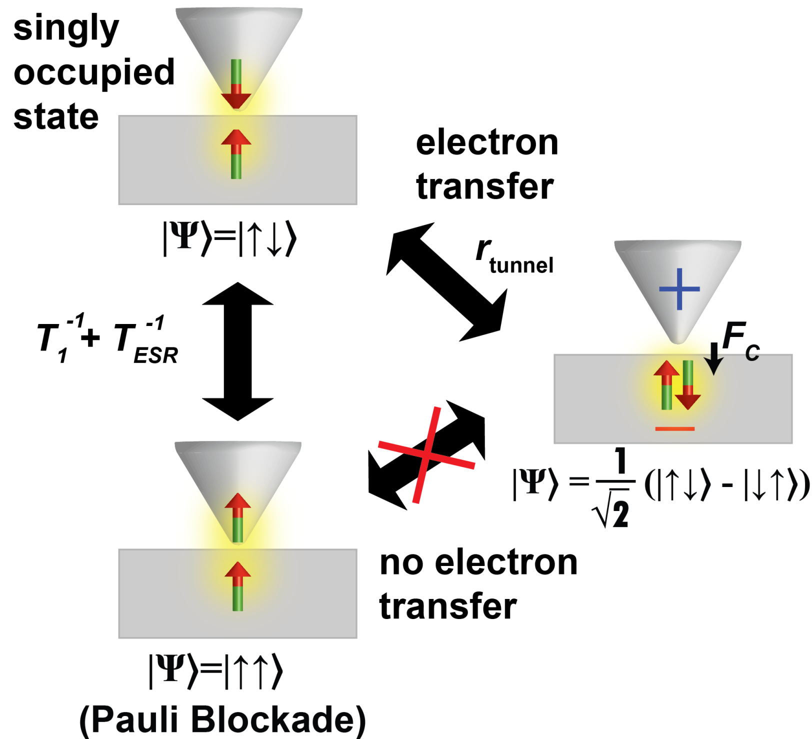

Figure 2.6. [Adapted from Payne et al.,[49] and partially modified] Illustrations of three possible charge and spin configurations of the probe spin/test spin pair when an energetic resonance and a spatial proximity is given. Top, left: A spin pair with mixed permutation symmetry allows for tunneling of the electron but also spin relaxation which turns the pair into a pure triplet state. Right: Tunneling creates a doubly occupied diamagnetic singlet state and a single elementary charge transfer which results in a cantilever frequency shift. The singlet state is maintained until one of the two electrons tunnels back into the probe. Bottom, left: When the spin pair exhibits high triplet content, Pauli blockade prohibits tunneling but spin relaxation allows for spin transitions into states with singlet content.

that can also only be attained when the charges are separated. On a statistical average, each configuration is equally probable. Therefore, the probability of each configuration at any given time is $\frac{1}{3}$, which implies for the average charge localization of the tunneling electron that it has a 2/3 probability to reside in the separated configuration (when the defects are neutral) and a 1/3 probability that they doubly occupy one defect (which makes this defect negative while the other defect is positive).

Under sufficiently strong magnetic resonant drive of either one of the separated defect centers, the modulation of the tunneling probability by spin relaxation disappears since the tunneling probability is then simply averaged between the singlet and

triplet tunneling probabilities. As a result, the tunneling dynamics changes. While this does not influence the average charge localization since the odds of having two neutral defects is still 2/3 probability versus 1/3 for having a doubly occupied state, and therefore, SSTFM cannot work by measuring the average charge or the magnitude of the cantilever resonance frequency shift, it does allow for force detected magnetic resonance by recording of the tunneling induced random telegraph signal noise.

In order to investigate this spin detection scheme, Payne et al. simulated the cantilever frequency shift noise (RTS) for random tunnel and spin relaxation transitions between the three spin and charge configurations illustrated in Fig. 2.6. We assumed that an oxidized crystalline silicon cantilever is used which has a paramagnetic center (E' center) located within a thin SiO_2 layer at its tip. E' centers are known to exhibit very long longitudinal spin relaxation times ($T_1 \approx 200\mu$s) even at room temperature [18, 12]. Single–spin detection requires the tunneling time T_t to be much shorter than the spin–relaxation time of either of the paramagnetic defects. Since the tunneling rate depends on the distance between the probe spin and the test spin, it can be well controlled with a state of the art scanning probe setup; therefore, assume that $T_t = 10\mu$s. Figure 2.7 displays the plot of the simulated cantilever charge fluctuation (1 and 0 indicating the separated and nonseparated charge cases, respectively) as functions of time during simulated time intervals of 100ms for the off- and on-resonance cases, respectively (note that only the first 2ms are displayed to better visualize the two cases). In the off–resonant case, the RTS undergoes blinking which means that there are time intervals where Pauli blockade prevents tunneling. In contrast, in the on–resonance case, tunneling occurs frequently and the blinking effect vanishes. For the simulation, the RF driving field was assumed to be intensive enough to make the resonantly induced singlet-triplet flip time T_f much shorter than the intrinsic spin–relaxation times of either one of the pair partners ($T_1 >> T_f$).

The simulated RTS transients shown in Fig. 2.7(a) represent the off- (blue) and on–resonance (red) behaviors of random tunneling events. Due to the change of the blinking behavior between the off–resonance and on–resonance case, the noise power spectral density of the RTS noise changes significantly as well, as shown by the noise spectral density plots obtained from the data in Fig. 2.7(a), that is displayed in

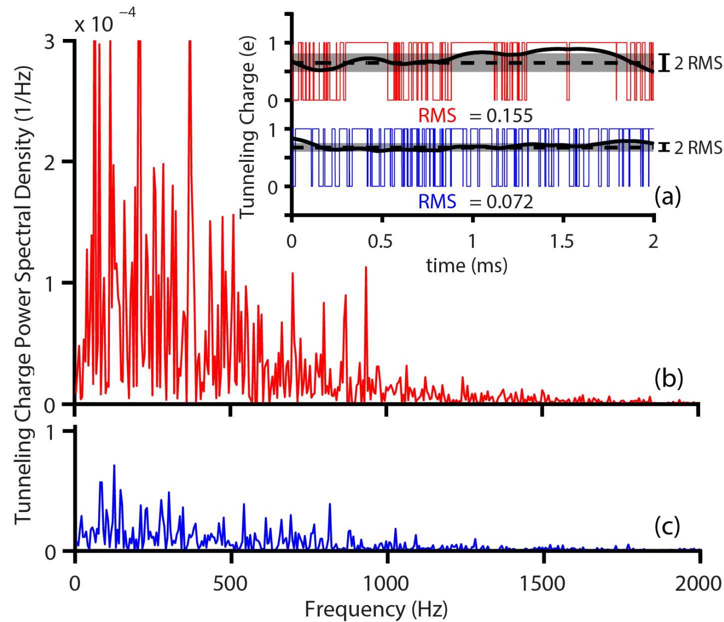

Figure 2.7. [Adapted from Payne et al.,[49]] Simulation of the spin-dependent tunneling noise and its power spectral density. (a) Simulation of the tunneling induced RTS noise transient due to spin–dependent tunneling between a paramagnetic probe state (the so–called probe spin) and a test spin at the sample surface for the absence (red) and presence (blue) of magnetic resonance conditions. The details on the simulation was described by Payne et al. [49]. (b,c) Plots of the tunneling charge power spectral density obtained from the simulations when magnetic resonance is absent (b) and present (c). The spectral noise density at lower frequencies displays a significant reduction under magnetic resonance.

Fig. 2.7(b) & (c). In absence of magnetic resonance, intensive low-frequency noise components appear compared to the on–resonance case. Hence, detection of magnetic resonance and thus, of single spins, will be possible by measuring the noise power (integrated root means square, RMS) of the RTS within an appropriate low–frequency bandwidth. Note that the gray shaded areas around the average charge localizations indicated in Fig. 2.7(a) represent the RMS values obtained from the simulated data with an assumed bandwidths of 1kHz.

The simulation was repeated and displayed in Fig. 2.7 and calculated the tunneling charge noise RMS for various bandwidths and as functions of the applied radio frequency (RF). The result of these simulations are displayed in Fig. 2.8. Panel (a) displays the results of these simulations for two RF frequencies corresponding to off- (red) and on- (blue) resonance cases. As shown, there is a recognizable difference

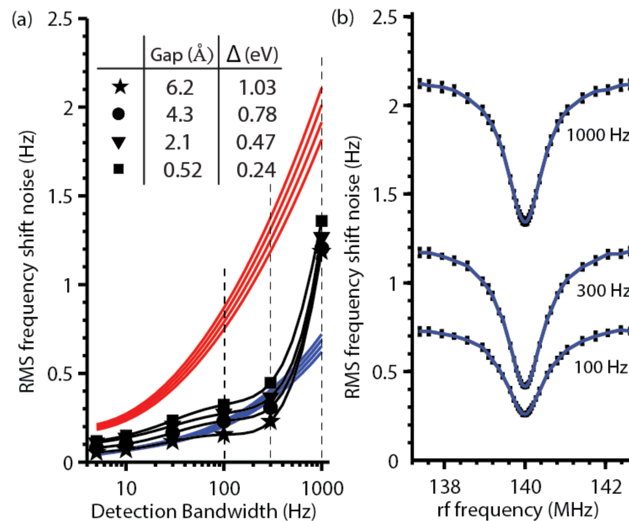

Figure 2.8. [Adapted from Payne et al.,[49]] Simulation of the tunneling charge noise RMS for various bandwidths and as functions of the applied radio frequency (RF). (a) Simulated frequency shift noise (RMS) caused by tunneling induced RTS noise in presence (blue) and absence (red) of magnetic resonance and the measured system frequency shift noise (black) connected by a guide to the eye (black lines). All data were obtained for four different cantilever–to–tip distances. (b) Simulations of the total frequency shift noise (RMS) consisting of the telegraph–noise signal as well as experimentally determined system–noise levels as functions of the applied RF frequency for three bandwidth regimes. For the assumed constant magnetic field of 5mT, the RF frequency range covers the $g = 2$ electron spin resonance condition. The widths of the displayed electron spin resonance are solely governed by power broadening. The bars connected to the data points indicate the standard deviation of the fluctuation of the noise power for an assumed finite integration time of 10ms. In order to discriminate on- from off–magnetic resonance conditions needed for the single–spin detection, the on–resonance charge noise and the system noise need to be significantly lower than the off-resonance charge noise. This condition is fulfilled between ≈10 Hz and ≈1kHz bandwidth.

between the predicted noise power of the two cases. It is also shown that the difference between off- and on–resonance gets bigger at larger bandwidth. Each set of four curves represents simulation results for four different probe–to–surface gaps with curves at the top representing the largest gap of 6.2 Å and the bottom curve representing the lowest tip–sample gap of about 0.52Å. The simulation results show that the signals do not change significantly with the gap. The simulated tunneling noise RMS as obtained from the RTS transients was converted into a cantilever frequency shift RMS (df_{RMS}) using a calibration constant that was calculated assuming an SiO_2 thickness of 10nm

in both tip and sample, a 10nm oscillation amplitude of the cantilever, an externally applied voltage between tip and sample of 10V, and both the probe state as well as the test state being located 0.2nm inside the surfaces of the probe and the sample, respectively. Since these simulations did not account for the presence of system noise found in a real AFM, the system noise was experimentally determined [black data points in 2.8(a)] using a modified commercial scanning probe microscope (Omicron UHV STM/AFM) and then added to the simulated RTS noise through geometric addition.

Figure 2.8(a) shows that for larger detection bandwidths, the AFM system noise can exceed the on–resonance RTS noise power and it even approaches the off–resonance RTS noise power. Similarly, as also shown in Fig. 2.8(a), the system noise causes a detectability loss of the magnetic resonance signal at very small bandwidths. The inset table of Fig. 2.8(a) shows various gaps and corresponding band–bending parameters. Figure 2.8(b) shows that the RMS value of the RTS noise power as a function the frequency of an applied RF field reveals the magnetic resonance spectrum of the probed spin. The error bars in these plots represent the standard deviation of RMS fluctuations as obtained from repeated simulations. As shown by the three data sets, single–spin detection will be possible up to a bandwidth of approximately 1KHz with the signal–to–noise being larger than one. Since the RTS noise is truncated by narrowing the bandwidth, the signal–to–noise ratio deteriorates at lower bandwidth. However, assuming the experimental parameters discussed above and given a bandwidth range of approximately 10Hz to 1kHz, force–detected single–spin resonance spectroscopy will be possible even at room temperature [49]

The simulations described above support the hypothesis that SSTFM is possible and given the experimentally proven spatial resolution of SETFM, it could allow for the observation of single paramagnetic centers with atomic scale spatial resolution. The SSTFM concept is the main motivation for the studies presented in Chapters 3 to 6 which have been focused on: (i) the demonstration that silicon dangling bond states in silicondioxide have all properties required to be used a probe spins (Chapter 3): (ii) the demonstration that a low–magnetic field domain magnetic resonance setup can be integrated into a high–resolution, ultra–high–vacuum, low–temperature (liquid

Helium-4) scanning probe facility (Chapter 4): (iii) the demonstration that this setup can be used for conduction-AFM experiments which allow to identify the locations of P donor states as well as silicon dangling bond states (Chapter 5): and (iv) the observation of RTS between silicon dangling bond states and a metal cantilever in darkness (using a Q-plus quartz tuning fork sensor).

2.4 References

[1] E. Bauer, M. Mundschau, W. Swiech, and W. Telieps. Surface studies by low-energy electron microscopy (LEEM) and conventional UV photoemission electron microscopy (PEEM). *Elsevier*, 31:49, 1989.

[2] G. Binnig, H. Rohrer, Ch. Gerber, and E. Weibel. Surface studies by scanning tunneling microscopy. *Phys. Rev. Lett.*, 49:57, 1982.

[3] F. Bloch. Nuclear induction. *Phys. Rev.*, 70:460, 1946.

[4] F. Bloch, W. W. Hansen, and M. Packard. The nuclear induction experiment. *Phys. Rev.*, 70:474, 1946.

[5] C. Boehme and K. Lips. Spin-dependent recombination − an electronic readout mechanism for solid state quantum computers. *Phys. Status Solidi B*, 233:427, 2002.

[6] C. Böhme. *Dynamics of Spin-Dependent Charge Carrier Recombination.* Cuvillier, 2003.

[7] J. Brossel, S. Geschwind, and A. L. Schawlow. Optical detection of paramagnetic resonance in crystals at low temperatures. *Phys. Rev. Lett.*, 3:548, 1959.

[8] E. Bussman. *Single Electron Tunneling Force Microscopy, Thesis.* University of Utah, 2006.

[9] E. Bussmann, D. J. Kim, and C. C. Williams. Single-electron tunneling to insulator surfaces measured by frequency detection electrostatic force microscopy. *Appl. Phys. Lett.*, 85:2538, 2004.

[10] E. Bussmann and C. C. Williams. Single-electron tunneling force spectroscopy of an individual electronic state in a nonconducting surface. *Appl. Phys. Lett.*, 88:263108, 2006.

[11] I. D. Campbell. Adiabatic rapid passage ESR of natural diamond. *J. Magn. reson.*, 74:155, 1969.

[12] J. G. Castle and D. W. Feldman. Temperature dependence of paramagnetic relaxation at point defects in vitreous silica. *J. Appl. Phys.*, 36:124, 1965.

[13] B. C. Cavenetta. Optically detected magnetic resonance (o.d.m.r.) investigations of recombination processes in semiconductors. *Adv. Phys.*, 30, 1981.

[14] A. M. Chang, H. D. Hallen, L. Harriott, H. F. Hess, H. L. Kao, J. Kwo, R. E. Miller, R. Wolfe, J. van der Ziel, and T. Y. Chang. Scanning hall probe microscopy. *Appl. Phys. Lett.*, 61:1974, 1992.

[15] C. J. Chen. *Introduction to Scanning Tunneling Microscopy.* New York, Oxford, 1993.

[16] H. Dersch, L. Schweitzer, and J. Stuke. Recombination processes in *a*-Si:H: Spin-dependent photoconductivity. *Phys. Rev. B*, 28:4678, 1983.

[17] M. Dobers, K. V. Klitzing, J. Schneider, G. Weimann, and K. Ploog. Electrical detection of nuclear magnetic resonance in $GaAs - Al_xGa_{1-x}As$ heterostructures. *Phys. Rev. Lett.*, 61:1650, 1988.

[18] S. S. Eaton and G. R. Eaton. Irradiated fused-quartz standard sample for time-domain EPR. *J. Magn. Reson. Ser. A*, 102:354, 1993.

[19] J. M. Elzerman, R. Hanson, L. H. Willems van Beveren, B. Witkamp, L. M. K. Vandersypen, and L. P. Kouwenhoven. Single-shot read-out of an individual electron spin in a quantum dot. *Nature*, 430:431, 2004.

[20] L. Esaki. New phenomenon in narrow germanium $p - n$ junctions. *Phys. Rev.*, 109:603, 1958.

[21] G. T. Genov, D. Schraft, T. Halfmann, and N. V. Vitanov. Correction of arbitrary field errors in population inversion of quantum systems by universal composite pulses. *Phys. Rev. Lett.*, 113:043001, 2014.

[22] S. Geschwind, R. J. Collins, and A. L. Schawlow. Optical detection of paramagnetic resonance in an excited state of Cr^{3+} in Al_2O_3. *Phys. Rev. Lett.*, 3:545, 1959.

[23] C. F. O. Graeff, M. S. Brandt, M. Stutzmann, M. Holzmann, G. Abstreiter, and F. Schäffler. Electrically detected magnetic resonance of two-dimensional electron gases in Si/SiGe heterostructures. *Phys. Rev. B*, 59:13242, 1999.

[24] I. Hiromitsu, Y. Kaimori, M. Kitano, and T. Ito. Spin-dependent recombination of photoinduced carriers in phthalocyanine/C_{60} heterojunctions. *Phys. Rev. B*, 59:2151, 1999.

[25] F. Hoehne, J. Lu, A. R. Stegner, M. Stutzmann, M. S. Brandt, M. Rohrmüller, W. G. Schmidt, and U. Gerstmann. Electrically detected electron-spin-echo envelope modulation: a highly sensitive technique for resolving complex interface structures. *Phys. Rev. Lett.*, 106:196101, 2011.

[26] F. Jelezko, T. Gaebel, I. Popa, A. Gruber, and J. Wrachtrup. Observation of coherent oscillations in a single electron spin. *Phys. Rev. Lett.*, 92:076401, 2004.

[27] J. P. Johnson, D. W. Winslow, and C. C. Williams. Measurement of depth and energy of buried trap states in dielectric films by single electron tunneling force spectroscopy. *Appl. Phys. Lett.*, 98:052902, 2011.

[28] J P Johnson, N Zheng, and C C Williams. Atomic scale imaging and spectroscopy of individual electron trap states using force detected dynamic tunnelling. *Nanotechnology*, 20:055701, 2009.

[29] B. E. Kane. A silicon-based nuclear spin quantum computer. *Nature*, 393:133, 1998.

[30] P. Kanschat, K. Lips, and W. Fuhs. Identification of non-radiative recombination paths in microcrystalline silicon (μc-Si:H). *J. Non-Cryst. Solids*, 266:524, 2000.

[31] D. Kaplan, I. Solomon, and N. F. Mott. Explanation of the large spin-dependent recombination effect in semiconductors. *J. Physique Lett.*, 39:51, 1978.

[32] J. Kim, J. S. McMurray, C. C. Williams, and J. Slinkman. Two-step dopant diffusion study performed in two dimensions by scanning capacitance microscopy and tsuprem iv. *J. Appl. Phys.*, 84, 1998.

[33] L. J. Klein and C. C. Williams. Single electron tunneling detected by electrostatic force. *Appl. Phys. Lett.*, 79:1828, 2001.

[34] D. J. Lepine. Spin-dependent recombination on silicon surface. *Phys. Rev. B*, 6:436, 1972.

[35] K. Lips and W. Fuhs. Transport and recombination in amorphous p-i-n-type solar cells studied by electrically detected magnetic resonance. *J. Appl. Phys.*, 74:3993, 1993.

[36] J. R. Matey and J. Blanc. Scanning capacitance microscopy. *J. Appl. Phys.*, 57:1437, 1985.

[37] R. Maxwell and A. Honig. Neutral-impurity scattering experiments in silicon with highly spin-polarized electrons. *Phys. Rev. Lett.*, 17:188, 1966.

[38] D. R. McCamey, G. W. Morley, H. A. Seipel, L. C. Brunel, J. van Tol, and C. Boehme. Spin-dependent processes at the crystalline Si-SiO_2 interface at high magnetic fields. *Phys. Rev. B*, 78:045303, 2008.

[39] D. R. McCamey, H. A. Seipel, S.-Y. Paik, M. J. Walter, N. J. Borys, J. M. Lupton, and C. Boehme. Spin rabi flopping in the photocurrent of a polymer light-emitting diode. *Nat. Mater.*, 7:723, 2008.

[40] D. McMullan. Scanning electron microscopy 19281965. *Scanning*, 17:175, 2006.

[41] A. Morello, J. J. Pla, F. A. Zwanenburg, K. W. Chan, K. Y. Tan, H. Huebl, M. Mttnen, C. D. Nugroho, C. Yang, J. A. van Donkelaar, A. D. C. Alves, D. N. Jamieson, C. C. Escott, L. C. L. Hollenberg, R. G. Clark, and A. S. Dzurak. Single-shot readout of an electron spin in silicon. *Nature*, 467:687, 2010.

[42] S. Morita and F. J. Giessible. *Non–Contact Atomic Force Microscopy*. Springer, 2009.

[43] G. W. Morley, L.-C. Brunel, and J. van Tol. A multifrequency high-field pulsed electron paramagnetic resonance/electron-nuclear double resonance spectrometer. *Rev. Sci. Instrum.*, 79:064703, 2008.

[44] J. R. Mueller, P. Kanschat, S. Von Aichberger, K. Lips, and W. Fuhs. Identification of transport and recombination paths in homo- and heterojunction silicon solar cells by electrically detected magnetic resonance. *J. Non-Cryst. Solids*, 266-269:1124, 2000.

[45] C. J. Nicklaw. *IEEE Transaction of nuclear science*, 49:2667, 2002.

[46] S.-Y. Paik, S.-Y. Lee, W. J. Baker, D. R. McCamey, and C. Boehme. T_1 and T_2 spin relaxation time limitations of phosphorous donor electrons near crystalline silicon to silicon dioxide interface defects. *Phys. Rev. B*, 81:075214, 2010.

[47] S.-Y. Paik, S.-Y. Lee, D. R. McCamey, and C. Boehme. Electrically detected crystal orientation dependent spin-rabi beat oscillation of c-Si (111)/SiO_2 interface states. *Phys. Rev. B*, 84:235305, 2011.

[48] S. T. Pantelides. The E$'$ center and oxygen vacancies in SiO_2. *J. Non-Cryst. Solids*, 354:217, 2008.

[49] A. Payne, K. Ambal, C. Boehme, and C. C. Williams. Atomic-resolution single-spin magnetic resonance detection concept based on tunneling force microscopy. *Phys. Rev. B*, 91:195433, 2015.

[50] M. Pelliccione, B. A. Myers, L. M. A. Pascal, A. Das, and A. C. Bleszynski Jayich. Two-dimensional nanoscale imaging of gadolinium spins via scanning probe relaxometry with a single spin in diamond. *Phys. Rev. Applied*, 2:054014, 2014.

[51] J. R. Petta et al. Coherent manipulation of coupled electron spins in semiconductor quantum dots. *Science*, 309:2180, 2005.

[52] T. A. Pomorski, B. C. Bittel, C. J. Cochrane, P. M. Lenahan, J. Bielefeld, and S. W. King. Defects and electronic transport in hydrogenated amorphous SiC films of interest for low dielectric constant back end of the line dielectric systems. *J. Appl. Phys.*, 114:074501, 2013.

[53] M. Rohrer, J. Krzystek, V. Williams, and L.-C. Brunel. Fabry-perot resonator for high-field multi-frequency EPR at millimeter and sub–millimeter wavelengths. *Measurement Science and Technology*, 10:275, 1999.

[54] F. C. Rong, G. J. Gerardi, W. R. Buchwald, E. H. Poindexter, M. T. Umlor, D. J. Keeble, and W. L. Warren. Electrically detected magnetic resonance of a transition metal related recombination center in Si $p-n$ diodes. *Appl. Phys. Lett.*, 60:610, 1992.

[55] D. Rugar, R. Budakian, H. J. Mamin, and B. W. Chui. Single spin detection by magnetic resonance force microscopy. *Nature*, 430:329, 2004.

[56] K. Saeedi, S. Simmons, J. Z. Salvail, P. Dluhy, H. Riemann, N. V. Abrosimov, P. Becker, H.-J. Pohl, J. J. L. Morton, and M. L. W. Thewalt. Room-temperature quantum bit storage exceeding 39 minutes using ionized donors in silicon-28. *Science*, 342:830, 2013.

[57] J. J. Sakurai. *Modern Quantum Mechanics*. 1993.

[58] A. Scholl, H. Ohldag, F. Nolting, J. Stohr, and H. A. Padmore. X-ray photoemission electron microscopy, a tool for the investigation of complex magnetic structures (invited). *Rev. Sci. Instrum.*, 73:1362, 2002.

[59] J. A. Sidles, J. L. Garbini, K. J. Bruland, D. Rugar, O. Züger, S. Hoen, and C. S. Yannoni. Magnetic resonance force microscopy. *Rev. Mod. Phys.*, 67:249, 1995.

[60] C. B. Simmons, J. R. Prance, B. J. Van Bael, T. S. Koh, Z. Shi, D. E. Savage, M. G. Lagally, R. Joynt, M. Friesen, S. N. Coppersmith, and M. A. Eriksson. Tunable spin loading and T_1 of a silicon spin qubit measured by single-shot readout. *Phys. Rev. Lett.*, 106:156804, 2011.

[61] J. H. Stathis. Electrically detected magnetic resonance study of stress–induced leakage current in thin SiO_2. *Appl. Phys. Lett.*, 68:1669, 1996.

[62] A. R. Stegner, C. Boehme, H. Huebl, M. Stutzmann, K. Lips, and M. S. Brandt. Electrical detection of coherent ^{31}P spin quantum states. *Nat. Phys.*, 2:835, 2006.

[63] B. Stich, S. Greulich-Weber, and J.-M. Spaeth. Electrical detection of electron nuclear double resonance in silicon. *Appl. Phys. Lett.*, 68:1102, 1996.

[64] M. Stutzmann, M. S. Brandt, and M. W. Bayerl. Spin-dependent processes in amorphous and microcrystalline silicon: a survey. *J. Non-Cryst. Solids*, 266-269:1, 2000.

[65] L. S. Swanson, J. Shinar, and K. Yoshino. Optically detected magnetic resonance study of polaron and triplet-exciton dynamics in poly(3-hexylthiophene) and poly(3-dodecylthiophene) films and solutions. *Phys. Rev. Lett.*, 65:1140, 1990.

[66] R. Wang, S. W. King, and C. C. Williams. Atomic scale trap state characterization by dynamic tunneling force microscopy. *Appl. Phys. Lett.*, 105:052903, 2014.

[67] X. Wei, B. C. Hess, Z. V. Vardeny, and F. Wudl. Studies of photoexcited states in polyacetylene and poly(paraphenylenevinylene) by absorption detected magnetic resonance: The case of neutral photoexcitations. *Phys. Rev. Lett.*, 68:666, 1992.

[68] S. Wimperis. Broadband, narrowband, and passband composite pulses for use in ddvanced NMR experiments. *J. Magn. Reson.*, 109:221, 1994.

[69] Dustin W. Winslow. *A Single Electron Tunneling Force Spectroscopy Study of Dielectric Materials, Thesis.* University of Utah, 2012.

[70] G. Wolfowicz, H. Maier-Flaig, R. Marino, A. Ferrier, H. Vezin, J. J. L. Morton, and P. Goldner. Coherent storage of microwave excitations in rare-earth nuclear spins. *Phys. Rev. Lett.*, 114:170503, 2015.

[71] J. Wrachtrup, C. V.Borczyskowski, J. Bernard, M. Orritt, and R. Brown. Optical detection of magnetic resonance in a single molecule. *Nature*, 363, 1993.

[72] M. Xiao, I. Martin, E. Yablonovitch, and H. W. Jiang. Electrical detection of the spin resonance of a single electron in a silicon field-effect transistor. *Nature*, 430:435, 2004.

[73] Z. Zavoiski. *J. Phys. USSR*, 9:211, 1945.

[74] N. Zheng, C. C. Williams, E. G. Mishchenko, and E. Bussmann. A three-dimensional model of single-electron tunneling between a conductive probe and a localized electronic state in a dielectric. *J. Appl. Phys.*, 101:093702, 2007.

CHAPTER 3

SYNTHESIS OF THIN SILICON DIOXIDE LAYERS WITH HIGH DENSITIES OF PARAMAGNETIC E$'$ CENTER WITH LONG SPIN–RELAXATION TIMES

The suitability of the spin–dynamics of paramagnetic silicon dangling bonds (E' centers) in high E'-density amorphous silicon dioxide (SiO_2) for SSTFM is studied. Following the synthesis of SiO_2 thin films on (111) oriented crystalline silicon substrates with room–temperature stable densities of $[E'] > 5 \times 10^{18} cm^{-3}$ throughout the 60nm thin film, pulsed electron paramagnetic resonance spectroscopy was conducted on the E' centers at temperatures between $T = 5K$ and $T = 70K$. The measurements revealed that the spin coherence (the transverse spin-relaxation time T_2) of these centers is significantly shortened compared to low-E' density SiO_2 films and within error margins not dependent on temperature. In contrast, the spin–flip times (the longitudinal relaxation times T_1) are dependent on the temperature but with much weaker dependence than low–density SiO_2, with greatest deviations from low–density SiO_2 seen for $T = 5K$. These results, discussed in the context of the spin–relaxation dynamics of dangling bond states of other silicon–based disordered solids, indicate the suitability of E' centers in high-density SiO_2 as probe spins for SSTFM. This work presented in this chapter was published recently [1], together with co-authors A. Payne, D. P. Waters, C. C. Williams, and C. Boehme who also have made significant contributions to this work.

3.1 Introduction

Over the past two decades, the promise of quantum information applications based on localized paramagnetic states has been one of the driving forces behind the rapid

development of various and single-spin detection and readout schemes [37, 30, 28, 23]. Experimentally demonstrated readout schemes differ conceptually significantly. Most utilize various spin–to–charge or spin–to–optical photon transition mechanisms in order to convert the weak interaction energies of electron and nuclear spins into straightforwardly detectable observables (by means of charge [23] or photon detection [37]). Other spin–detection schemes are based on scanning probe microscopy [30, 3]. For instance, magnetic resonance force microscopy is capable of directly measuring the minute magnetic force produced by a single–spin. This, however, is only possible with limited spatial resolution (nm scales rather then atomic scales) and long measurement times [22] or they require sufficiently conductive probes or substrates [16, 36] whose charge carrier reservoirs can be detrimental for the coherence times of localized spin–qubits.

We have therefore described recently [27] a force detected scanning probe based single–spin–readout that combines the advantages of high spatial resolution with the advantage of using spin–selection rules for the conversion of spin–states into straightforwardly detectable charge states. An illustration of this concept is shown in Fig. 3.1(a). It consists of a low–magnetic field magnetic resonance setup combined with a scanning force probe whose tip consists of a dielectric material with a highly localized paramagnetic electron state, the so–called probe spin, right at the apex. The idea behind this concept is to utilize scanning probe force microscopy for the detection of individual charge transitions and to then detect spin states through spin–selection rules that control these charge transitions [4, 32]. By adjustment of the electronic energy levels of probe spin and test spin, spin–dependent tunneling causes electrostatically induced force noise which reveals the spin dynamics of the test/probe spin pair [27]. The contrast of this single–spin tunneling force microscopy (SSTFM) detection approach to existing force–microscopy based spin–detection schemes is that those are based on the direct detection of very weak dipolar magnetic forces [30] or combinations of spin–selection rule governed optical transitions with scanning probe techniques [22], while SSTFM relies on the measurement of Coulomb–forces which are many orders of magnitude stronger. We note that for the presence of pronounced spin–selection rules, weak spin–orbit coupling is needed in order to op-

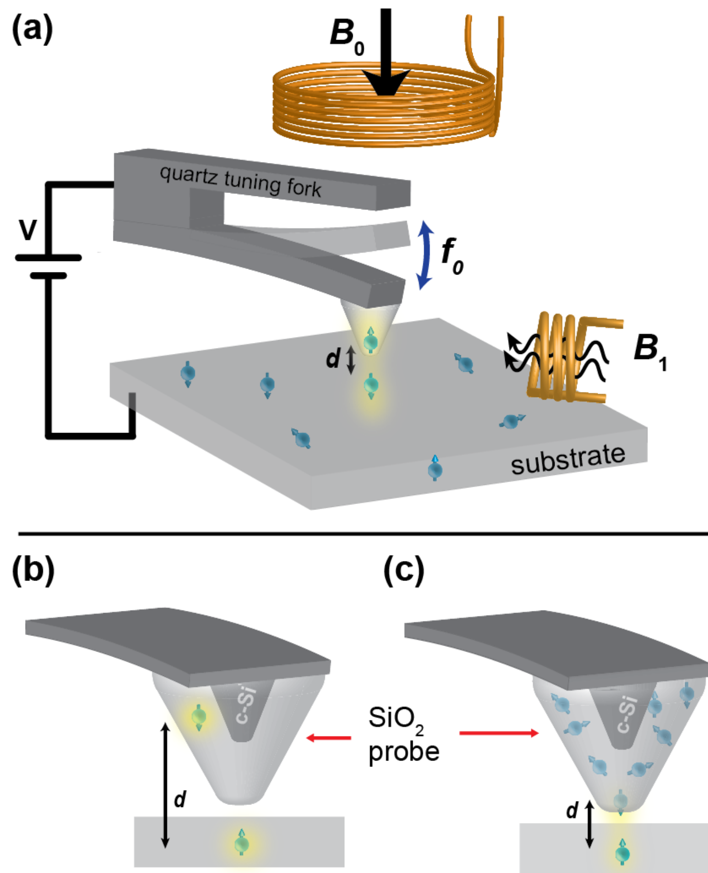

Figure 3.1. Illustration of the SSTFM concept as outlined in detail by Payne et al. [27]. (a) Illustration of the setup which includes mutually perpendicular coils that allow the generation of static and oscillating magnetic fields B_0 and B_1, respectively, for low–magnetic field magnetic resonance and a force detector with a dielectric tip that has a highly localized probe spin close to its apex. Payne et al. have proposed SiO_2 as dielectric tip material and the E' center therein as probe spin. (b) and (c) illustrate that the density of the randomly generated E' centers in the amorphous SiO_2 layer must be high enough such that an E' center is likely to be located within a minimal distance d of the tip apex such that enough exchange between probe spin and test spins can be established by tip positioning such that significant spin–dependent tunneling rates are possible.

press spin–orbit transitions. This is the case for instance in silicon based materials (mono-, poly, micro-, and nano-crystalline as well as amorphous silicon, silicondioxde, siliconnitride combinations thereof) where many spin–dependent transitions between localized paramagnetic states are known [4, 32, 26, 12].

For the implementation of SSTFM, Payne et al. [27] suggested to use a crystalline silicon (c-Si) scanning probe tip with an amorphous silicondioxide (SiO_2) film in which

a single E' center [17, 19, 35, 34] would be used as probe spin, located at the apex. E' centers exhibit positive correlation energies and are therefore paramagnetic, a property that allows them to be studied with electron paramagnetic resonance (EPR) spectroscopy [2, 31]. As E' centers have been studied extensively with regard to their behavior as trap states in SiO_2–based electronic devices (e.g., the gate dielectric of silicon thin film transistors [19]), most studies of E' center properties in the past have focused primarily on how E' center densities can be minimized by SiO_2 preparation and treatment. Few studies have focused on the dynamic properties of this spin $s = 1/2$ system, but those that have show that E' centers exhibit remarkably long longitudinal (T_1) spin relaxation times over large temperature ranges [7, 6, 8, 10, 34]. At room temperature, T_1 times on the order of hundreds of microseconds have been reported [8]. This is long compared to the T_1 times of silicon dangling bonds at the SiO_2 to crystalline silicon (c-Si) interface [26] (the so–called P_b centers) and it is comparable to other bulk silicon dangling bond states, e.g., in amorphous silicon [33] or microcrystalline silicon [21, 5].

Since E' centers develop at random sites within the continuous random network of SiO_2, Payne et al. [27] suggested to obtain an individual probe spin within a few Ångstroms of the tip apex by growth of an SiO_2 layer on a c-Si cantilever with high enough density [E'] of E' centers such that a sufficiently large probability exists that a single E' center is close enough to the apex. An appropriate proximity would be defined by a distance d such that significant tunneling probability to a localized state outside of the tip material is possible [see illustration in Fig. 3.1(b) and (c)]. Thus, [E'] must be high enough such that the probability to find an E' center within appropriate apex vicinity is within the order of unity. For this density, the E' centers must be chemically and optically stable over long time scales (weeks or months), preferably at room temperature. Furthermore, E' centers in such high-[E'] SiO_2 must exhibit similarly long transverse spin relaxation times (T_1) as E' centers in low–[E'] SiO_2. If the mutual proximity of the E' states significantly increases spin relaxation rates, applicability for spin readout will be limited [27].

In the following sections, we present measurements of the spin–relaxation dynamics of E' centers for high-[E'] films. Both T_1 and T_2 are studied after we first describe

the synthesis of SiO_2 thin films with highest thermally and optically stable densities of E' centers. The results of this study will then be discussed with regard to the suitability of the created high–[E'] SiO_2 for SSTFM.

3.2 Experimental techniques

For the corroboration of E' center densities as well as the measurements of spin–relaxation times, continuous wave (cw) EPR [2] and pulsed (p) EPR experiments [31] were carried out, respectively. The experiments were conducted at X-band frequencies using a cylindrical dielectric resonator as part of a Bruker Flexline EPR probehead, a Bruker Elexsys E580 EPR spectrometer, and an Oxford flow cryostat for the temperature adjustment. The cw EPR experiments were conducted using a lock–in detected modulation of the quasi–static magnetic field B_0 with an amplitude of ≈ 0.1mT and a frequency of 10KHz. The quasi static field B_0 was then adiabatically swept in order to find the EPR resonance condition where the Zeeman splitting of the paramagnetic centers is tuned to the applied microwave radiation.

For each cw EPR measurement, the sample was inserted into the dielectric resonator and the resonator was critically coupled to the microwave circuit. Because of the field modulated lock–in detection, all cw EPR absorption spectra display the first derivative of the real absorption function. Integrating lock–in detected absorption spectra produces the real EPR absorption spectra and the areas under these functions are proportional to the number of paramagnetic centers in the observed EPR line. For the absolute quantification of the density of paramagnetic states that belong to an observed resonance line, the line integral is scaled by a reference line integral that stems from the spectrally well–separated phosphorous (^{31}P) donor resonance that is caused by the well–known donor bulk density in the crystalline silicon sample substrate as outlined in detail below.

For the pEPR experiments, the dielectric resonator was decoupled in order to increase its band width. For the measurements, brief ($\sim$ 16ns) high–power (up to 1kW) microwave pulses or pulse sequences were irradiated under resonant condition. The radiation response of the sample was then detected using solid state detection diodes and recorded using a Bruker Specjet transient recorder. For the determination of the

longitudinal and transverse spin–relaxation times T_1 and T_2, an inversion–recovery sequence and a standard two–pulse Hahn–echo sequence were used, respectively, as described in the literature [31].

3.3 Materials preparation: Synthesis of thin SiO_2 films with very high E′ center densities

An estimate for the active tip volume in which a single E' center can be utilized as a probe spin for SSTFM in the grown oxide layer can be obtained from the product of a typical tip surface area of less than $300nm^2$ for a 25nm tip radius and a typical tunneling depth of less than 2nm [27]. Thus, $[E'] \approx 10^{18}cm^{-3}$ to $10^{19}cm^{-3}$ is needed. This is higher than the highest previously reported values for [E'] [19] which were generated via electric currents through SiO_2 gate dielectrics, a procedure that is hardly applicable to cantilever surfaces. These unprecedented high values for [E'] needed for the proposed spin–readout concept raise the question if continuous random SiO_2 networks can even exits under these conditions or whether quick recombination of E' centers into silicon–silicon bonds will put an upper limit on [E'].

Theoretical calculations do not prohibit the existence of such SiO_2 layers: Constraint Theory [29] applied to thin SiO_2 layers only imposes lower limits on silicon dangling bond densities in both the bulk (the E' states) as well as the crystalline silicon to SiO_2 interface [20] (where silicon bonds are called P_b centers), predominantly due to the flexibility of the wide range of the oxygen bond–angles. Furthermore, due to the bond length constraint in the lower Å–range, recombination of adjacent E' states into Si–Si bonds is not expected either for $[E'] \leq 10^{19}cm^{-3}$. However, under the assumption of dangling bond distances below 5nm ($[E'] \sim 10^{19}cm^{-3}$), the continuous random network is expected to be significantly underconstrained causing the resulting network to soften to a degree where local network elements will undergo localized motion (through wagging, streching, and rocking transitions) that departs entirely from the phonon mode structure of low-[E'] SiO_2.

For the study of various E' preparation techniques that can induced very high [E'], we used n-type, ^{31}P–doped ($[^{31}P] \approx 10^{15}cm^{-3}$) Czochralski grown c-Si(111) wafers. The use of ^{31}P–doped material allowed a very accurate determination of the E' densities from EPR spectra since the well–known hyperfine split ^{31}P resonance could

be used as an in-sample spin-standard. The 300 micrometer thick 3" wafers were first annealed in oxygen at atmospheric pressure and 1000°C in order to form an approximately 60nm thick (profilometer measured) thermally grown SiO_2 layer. The oxidized samples were then diced into 60mm x 3mm size EPR compatible rectangles. The black data points of Fig. 3.2 display an EPR spectrum of the as prepared thermal oxides. The two peaks are due to the hyperfine split ^{31}P resonance that, due to the known ^{31}P bulk density and therefore areal density ($\approx 3 \times 10^{13}$cm^{-2}), can be used to calibrate the magnetic field and density scales for the E' center measurements. The black data points show almost no resonant features next to the ^{31}P hyperfine peaks which means that E' densities in as grown samples are below the detection limit which is $\approx 1 \times 10^{12}$cm^{-2} for the given measurement conditions. This corresponds to an average volume density below $\approx 1.67 \times 10^{17}$cm^{-3} within the 60nm thin film. Thus, given that previous reports of E' densities in thermally grown SiO_2 are all significantly below the 10^{17}cm^{-3} limit, we expected no significantly different EPR signals from E' centers for the as grown oxide layers.

In order to explore how to create E' densities $> 10^{17}$cm^{-3}, the thin SiO_2 layer was exposed to (i) ultraviolet (UV) radiation [38] (produced by a NdYAG laser with 264nm wave length) for six hours, (ii) gamma radiation produced by a ^{137}Cs sample for 24 hours, producing an overall irradiation dose of about 10-12Mrad [39], (iii) different growth temperatures during the thermal growth, and (iv) an Ar-ion discharge plasma excited by a 300W 13.56MHz RF excitation at 0.5sccm gas flow and a pressure of 10mTorr [15, 13]. We then conducted EPR measurements similar to those shown in Fig. 3.2 on the samples treated according to (i), (ii), and (iii). These measurements revealed similar results compared to the as grown sample, represented by the black data in Fig. 3.2. This again confirmed the previous reports that treatment of SiO_2 layers following these methods may increase the E' center densities but not beyond the 10^{17}cm^{-3} range.

In contrast, the application of the Ar-ion plasma treatment (method iv) caused a significant increase of the E' density, as indicated by the blue circled data points in Fig. 3.2. The plot displays a feature at a magnetic field of approximately 348mT, corresponding to a Landé-factor of $g \approx 2.001$ which is attributed to plasma induced E'

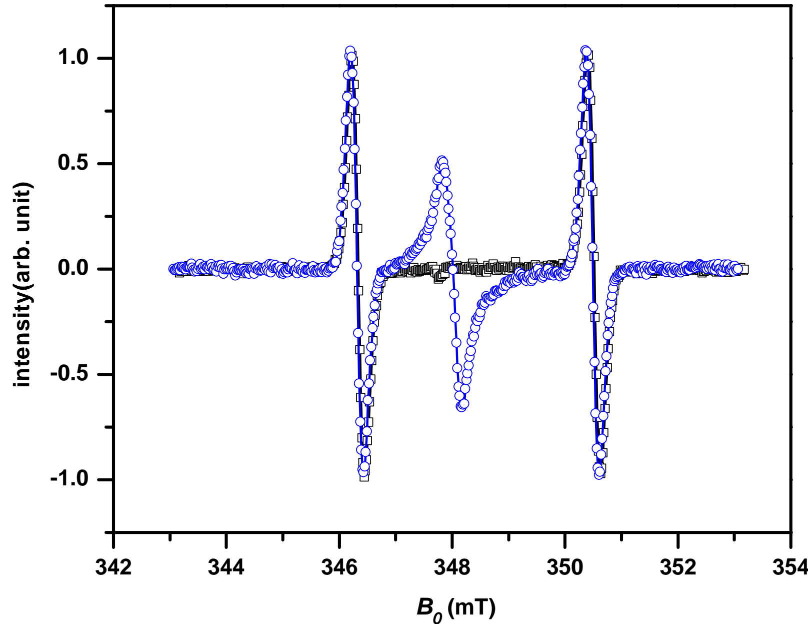

Figure 3.2. Plots of X-Band EPR spectra of 60mm x 3mm x 0.3mm large ^{31}P doped c-Si(111) samples measured at a temperature $T = 20$K with a field modulation frequency $f = 10$kHz, a modulation amplitude of 0.1mT, and a weak microwave power of 4μW to avoid saturation. The samples had 60nm thin layers of thermally grown SiO_2. The black data points represent measurements of the as prepared thermal oxide. The blue data points show a measurements under identical conditions after the sample was been exposed to an argon ion plasma for 5 minutes.

centers. The average E' center volume density in this film derived from the measured areal density per film thickness is 6×10^{18}cm^{-3}, determined by using the ^{31}P donor spins in the silicon substrate as a reference. While this observation shows that the plasma exposure of the oxide film is able to generate a large quantity of paramagnetic species at the g-factor anticipated for E' centers, it is not clear whether these states are all E' centers (silicon dangling bonds within the SiO_2 bulk). Other paramagnetic species such as interface defects between the SiO_2 layer and the c-Si bulk (if the etch has not removed the entire oxide) or the plasma etched c-Si surface states (if the oxide was completely removed) could also contribute to the observed signal. In order to explore this question, the depth distribution of the plasma induced paramagnetic states was studied by repetition of the EPR determined density measurement as a function of several oxide thicknesses after the partial removal of the oxide by a wet chemical etch. For this step etch experiment, a dilute HF solution was used. After

each HF-etch step, the oxide thickness was measured by ellipsometry and the areal density of the paramagnetic centers was determined by EPR spectroscopy. Figure 3.3 displays the results of these measurements for both the area concentration as a function of remaining oxide thickness (a) and the raw data given by the EPR spectra of the sample recorded after the individual etch steps (b).

Figure 3.3(a) also displays an offset–free linear fit which shows good agreement with the data. This agreement is indicative of a homogeneous distribution of the plasma–generated centers throughout the oxide layer. From the slope of the fit, we obtain a volume density $6.2(3) \times 10^{18}\text{cm}^{-3}$. Based on the measurements presented in Fig. 3.3, we conclude that we have found a method to generate SiO_2 layers with very large densities of paramagnetic E' centers as needed.

3.4 Thermal and light induced stability of very high E′ center density films

In order to study the thermal stability of the large Ar^{+} plasma induced E' center densities, we conducted a series of anneal experiments on high–density samples that were plasma treated for 5 minutes with the plasma parameters described above. The thermal anneal was then conducted for 20 minutes under ambient conditions at various temperatures between room temperature and 290°C. Using lock–in detected cw EPR, the E' center's area density was then measured as described above and the measured spectra were integrated in order to determine absorption peak areas. The results of these measurements are displayed in Fig. 3.4(a). The set of spectra illustrates how the plasma generated ensemble of paramagnetic states gradually disappears with increasing anneal temperature. The plot in Fig. 3.4(b) displays the E' center densities that were derived from the integrated lock–in detected cw EPR measurements as a function of the preceding anneal temperatures. From the difference of the E' densities of the nonannealed sample and these data, one can obtain the density loss as a function of temperature, which is displayed as an Arrhenius plot in Fig. 3.4(c). The fit of these data with an Arrhenius function reveal an activation energy of $\Delta = 176(1)$meV. The anneal experiments show that plasma induced high E' center densities can be annealed at comparatively low temperature. However, since $\Delta > k_{\mathrm{B}}T_{\mathrm{room}}$, room temperature stability of the defects is observed. We note

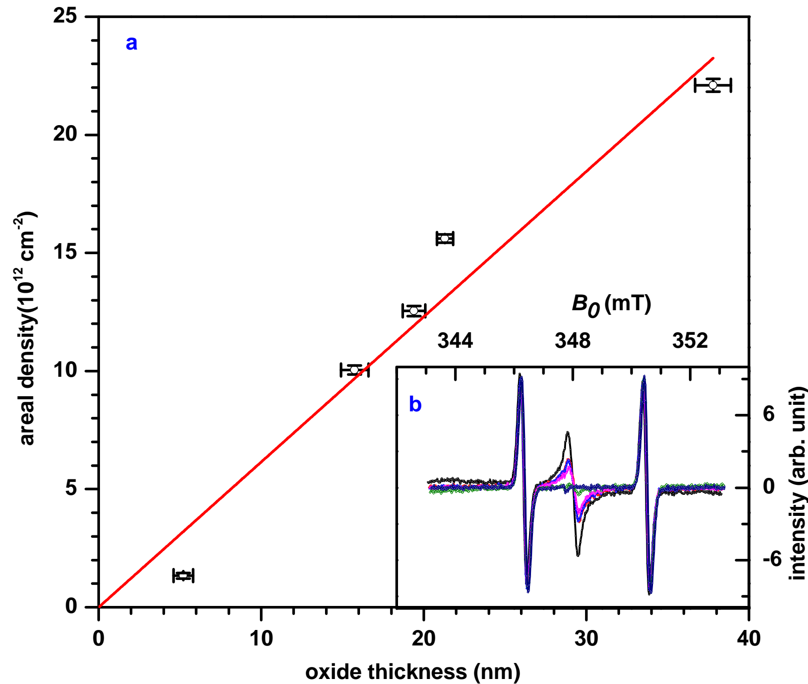

Figure 3.3. Distribution of the E' center density as a function of the oxide thickness. (a) Plot of the measured E' center area density as a function of the different oxide thicknesses and an offset–free linear fit (red line). The agreement of the measured data and the linear fit indicates that the observed paramagnetic defects created by the Ar^+ plasma are bulk defects. (b) Plots of the EPR spectra measured on SiO_2 samples that have been exposed for different durations to dilute HF. The remaining oxide thickness on each sample was measured by ellipsometry.

that the observed low activation threshold for E' center recombination appears to be analogous to that of P_b centers at the crystalline silicon to SiO_2 interface. For the latter, Lenahan and Dressendorfer observed a significant reduction of the γ-radiation induced P_b densities (with initial nearest neighbor distances corresponding to those of the E' centers studied here) for similar anneal temperatures ($\approx 250°$C) [18].

In order to further scrutinize the stability of the plasma induced high E' center densities, we have conducted photo–bleaching experiments. We exposed plasma treated but not annealed SiO_2 layers for 60 minutes to two different light sources: (a) a UV source with two strong emission maxima at around 174nm and 254nm, and (b) an incandescent spectral light lamp which emits mostly in the visible wavelength range. Figure 3.5 displays two plots, each of which contain two EPR spectra of the plasma etched but otherwise untreated sample and the bleached samples, respectively. The

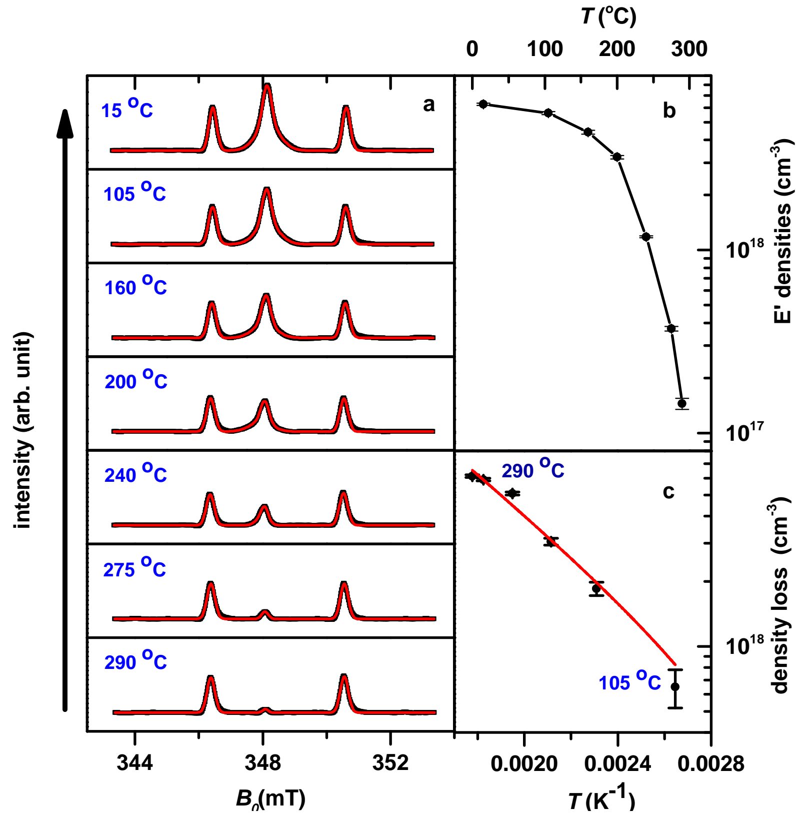

Figure 3.4. Decay of E' center density as a function of thermal annealing temperature. (a) Integrated lock–in detected cw EPR spectra measured after different annealing temperatures (black lines) and fit of the data with three Gaussian peaks. The density of the E' centers decreases with temperature and at 290°C, it is reduced by an order of magnitude. (b) Plot of the E' center densities obtained from the fit results displayed in (a) as a function of the temperature. (c) Arrhenius plot of the density loss, the difference of the room temperature sample, and the annealed samples as a function of the anneal temperature. The fit with an Arrhenius function reveals a resonable agreement and a defect anneal activation energy of 0.176(1)eV.

two plots (a) and (b) correspond to the UV bleaching experiment and the visible light experiment, respectively. The data sets show that photo bleaching has a significant effect for both light sources as both postexposure spectra exhibit smaller E' center resonances. However, in comparison to the comparatively minor loss for the visible spectral lamp (b), the exposure by UV light causes a reduction of the E' density by a significantly larger amount. This realization that bleaching can have similar effects as annealing could be significant for the development of low–temperature adjustment of well–defined E' center densities.

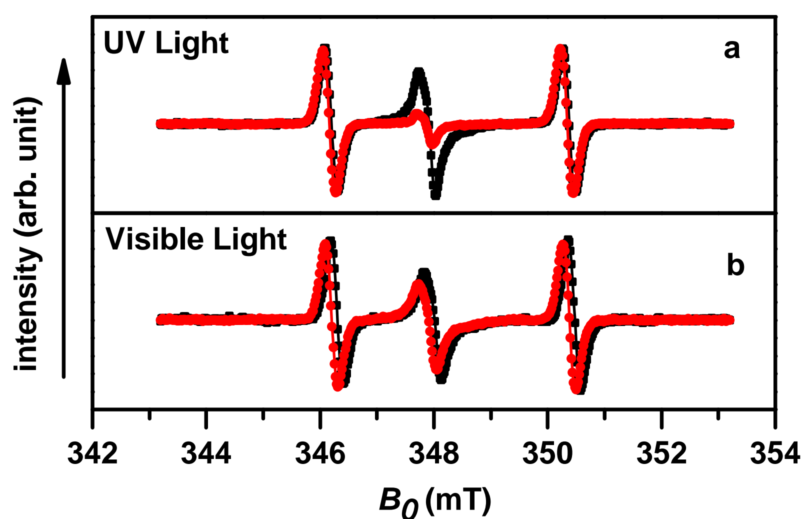

Figure 3.5. EPR spectra of high E' center density SiO_2 films measured before (black data) and after (red data) a one hour exposure with UV light (a) and visible light (b). Both photo–bleaching experiments show that the light exposure leads to a reduction of the E' center densities. However, this effect is significantly stronger for UV light exposure.

Finally, we tested the long–term stability of the plasma generated high E' center densities at room temperature. Using EPR, we measured repeatedly the density of a plasma treated sample over a time of approximately five weeks. During this time, the sample was kept at ambient conditions and at room temperature. The results of these measurements are displayed in the plot of Fig. 3.6. Over the course of about month, a clear decline of the E' density to about half of its original value is recognizable. While this is a significant decrease, the resulting half life of the generated E' center densities exceeds by far the expected duration of the single–spin experiments for which the high E' center densities are needed.

3.5 Spin relaxation dynamics of E′ centers at high–densities

The application of high–density E' center SiO_2 layers for scanning probe based spin readout requires sufficiently long spin relaxation times T_1 and T_2 [27]. The magnetic resonance spectra discussed above give no indication that there is any microscopic difference between E' centers in the high–density material reported here compared to previously studied low–density materials as resonance line and inhomogeneous line widths are comparable. Consequently, one may hypothesize that the intrinsic relaxation behavior of an individual E' center could be similar or identical in high- and low-density films. However, the decreased average distance between the E' centers at high–densities could increase their mutual spin interactions, mostly because of spin–dipolar coupling that becomes significant below 5nm nearest neighbour distances, to a lesser extent because of exchange, since the latter is weak due to the strong localization [17] of the E' center. Spin–spin interaction can directly quench T_2 relaxation times, while T_1 times can be affected by electronic interactions between the localized E' states.

Figures 3.7 and 3.8 show the results of both longitudinal (T_1) and transverse (T_2) spin relaxation times on the high–density SiO_2 reported above. For these measurements, we have applied pEPR experiments in a temperature range of $T = 5$K to $T = 70$K. Due to the temperature dependence of equilibrium polarization, spin echo measurements could be conducted on the very small spin ensemble of the thin

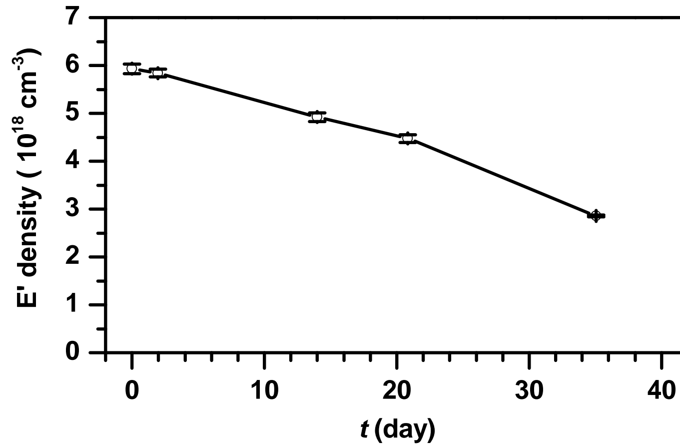

Figure 3.6. Plot of EPR measured E' center densities of an SiO_2 layer after plasma treatment over the course of approximately five weeks. A gradual decline of the density is observed. However, the decay is slow enough such that even after about five weeks, the absolute volume density still exceeds $10^{18}\mathrm{cm}^{-3}$.

film samples only up to about 70K. We displayed the data in Fig. 3.7 and 3.8 as Arrhenius plots with extrapolations of the experimental data to room temperature and Arrhenius fits, even though we note that with the overall weak temperature dependencies of the observed spin relaxation dynamics and the given measurement errors, an Arrhenius activation of the observed processes cannot be claimed with high significance, nor is it expected in absence of a rigorous theoretical treatment of the E' relaxation dynamics at these very high [E'].

We note that because of the time–dependence of [E'] that was discussed above, the spin–relaxation times were acquired for all measurements within a few hours after the materials preparation. As the measurements for T_1 and T_2 required averaging times on the order of hours, we repeatedly prepared new samples in order to limit the sample age for each measured value to less than 12 hours, a procedure that ensured that [E'] errors due to defect recombination remained low for the reported measurements.

3.6 Transverse spin relaxation

In order to measure T_2 relaxation times, a two pulse Hahn–echo experiment was performed. Figure 3.7 displays the results of these measurements (the relaxation rate coefficient T_2^{-1}) as a function of the inverse temperature ($1/T$). The data points in this plot were obtained by execution of Hahn–echo decay experiments where a

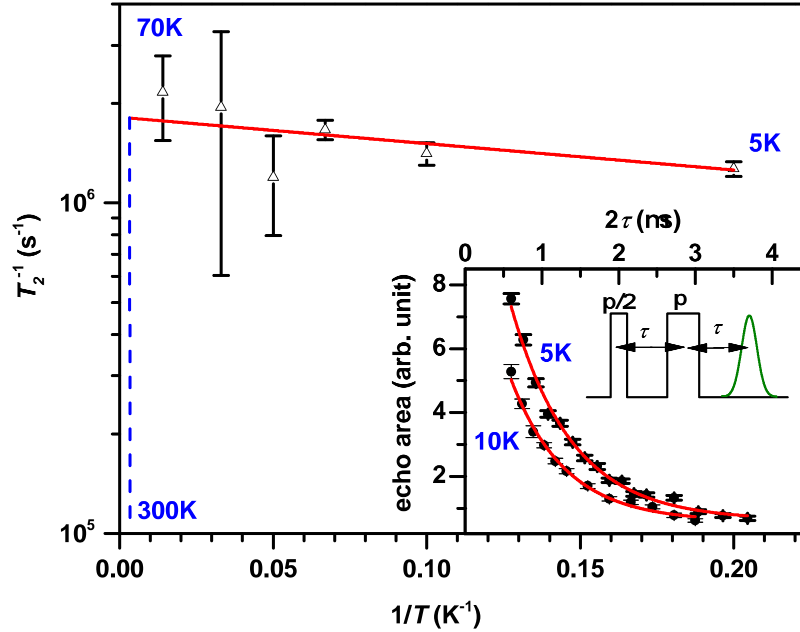

Figure 3.7. Plot of the measured transverse E' center spin relaxation rate coefficients T_2^{-1} and their error margins as a function of the inverse temperature. The red line represents a fit with an Arrhenius function. The inset displays a sketch of the Hahn–spin echo sequence that was used to measure T_2 as well as a plot of the measured Hahn–echo intensity as a function of the pulse separation time τ for $T = 5$K and $T = 10$K, with the plots of fits of these data sets with exponential decay functions. Within the given error margins, no temperature dependence of the T_2 relaxation is observed.

standard Hahn-echo pulse sequence consisting of a $\pi/2 - \pi$ is applied on resonance to the spin ensemble and the integrated intensity of the resulting spin–echo is then measured as a function of the pulse separation time τ. For the examples at low temperature ($T = 5$K, $T = 10$K), the employed pulse sequence as well as the decay data of the Hahn–echo amplitude are displayed in the inset, along with a fit by an exponential decay function which shows agreement with the experimental data.

The measured transverse spin relaxation times of $T_2 \approx 0.5\mu$s showed no significant dependence on temperature. These measurements display significantly shorter T_2 times compared to room temperature values obtained on bulk SiO_2 [10, 14] which suggests that the much higher spin-spin interaction between E' centers due to the higher [E'] causes an increase of the transverse dephasing rate and thus, a shortened T_2. The temperature independence is indicative that phonon-processes do not play a

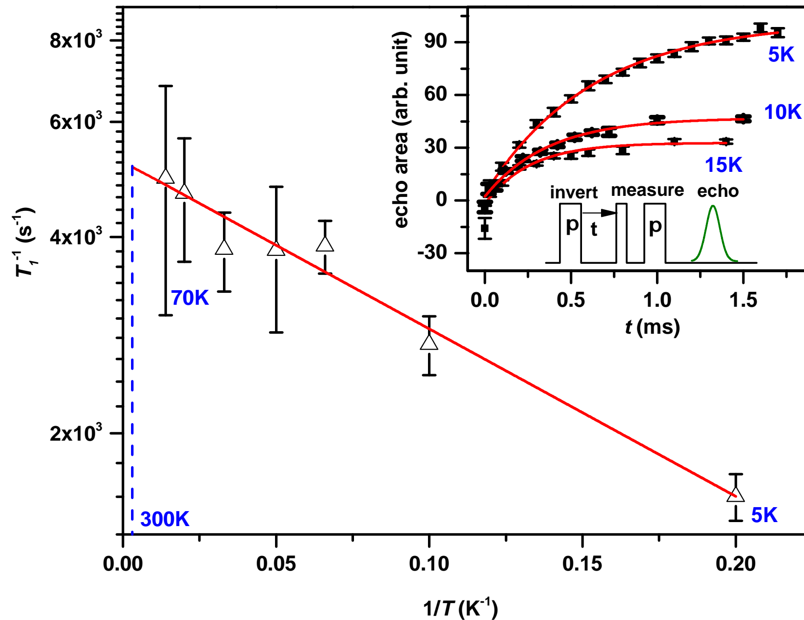

Figure 3.8. Plot of the measured longitudinal E' center spin relaxation rate coefficients T_1^{-1} and their error margins as a function of the inverse temperature. The red line represented a fit with an Arrhenius function. The dashed line indicates the room temperature value of T_1 that is extrapolated from the measurements conducted at lower temperatures. The inset displays a sketch of the inversion recovery pulse sequence that was used to measure T_1 as well as a plot of the Hahn-echo intensity as a function of the inversion delay time t for $T = 5$K, $T = 10$K, and $T = 15$K as well as plots of the fit results with exponential recovery functions.

role for T_2.

3.7 Longitudinal spin relaxation

For the measurements of the spin relaxation times T_1, the Hahn-echo pulse sequence used for the T_2 measurements was extended by one pulse such that polarization inversion recovery could be observed. The inset of Fig. 3.8 displays this pulse scheme which begins with a π-inversion pulse of the spin ensembles equilibrium polarization. After the inversion, a delay time t passes before a Hahn–echo pulse sequence is applied which reveals the residual polarization of the spin ensemble. Measurement of the ensemble polarization as a function of the delay time t will then reveal the dynamics of how the inverted spin polarization right after the inversion pulse gradually relaxes back towards a thermal equilibrium polarization. The inset of Fig. 3.8 shows plots of the measured polarization as a function of the delay time t for temperatures $T = 5$K,

$T = 10$K, and $T = 15$K. The data sets show that for small t, the measured residual polarization is less than 0, representing a negative (inverted) polarization, yet not a fully inverted polarization since not all spins can be flipped due to the amplitude of the inversion pulse. Since the width of the resonance ($\sim$ 2mT) is much larger than the highest driving field strengths that the given experimental setup is able to produce ($\sim$ 1mT), strong dephasing during a π–pulse is expected. The ensemble inversion caused by the pulse is therefore rather an ensemble scrambling that diminishes its polarization. There is also a finite detection dead time of the microwave detector after the inversion recovery sequence is executed, due to which the resonantly induced inversion can only be detected when it has already partially decayed. This reduction of the polarization applies for the detection of both inverted as well as noninverted ensemble polarization though. For long inversion times t, a positive equilibrium polarization is reestablished.

The experimental data for the inversion recovery transients are well fit by exponential recovery functions and the time constants obtained from these fits represent the measured T_1 values. The main plot of Fig. 3.8 displays the measured T_1 rate coefficients ($= T_1^{-1}$) as a function of the inverse temperature as well as a plot for an Arrhenius function that has been fit to the experimental data. The extension of this Arrhenius function to $T = 300$K reveals an extrapolated room temperature longitudinal spin relaxation time of $T_1 = 195(5)\mu$s, a value that is in good agreement with T_1 times measured on low density bulk SiO_2 [8, 10], even though this does not validate the applicability of the Arrhenius processes as discussed above. At low temperatures, the longitudinal spin relaxation times are significantly shorter compared to measurements made on low E' center–density SiO_2 [6].

The high T_1 relaxation rates as well as the overall significantly lower temperature dependence of T_1 in high–[E'] SiO_2 compared to low–[E'] SiO_2 [6] and other disordered semiconductor materials that contain silicon dangling bonds (e.g., amorphous silicon [33] or microcrystalline silicon [9]) suggest that at high [E'] and low temperatures, mechanisms other than the pure phonon scattering processes can become dominant. The agreement of T_1 for the highest measured temperature of $T = 70$K and the Arrhenius extrapolation to room temperature with order of magnitude ranges for

previously reported values for low–[E'] SiO_2 suggests that longitudinal relaxation at higher temperatures may be governed by direct spin–phonon interaction at high as well as low values of [E']. Systematic studies of the density dependence of dangling bond T_1 relaxation times in SiO_2 have been scarce, both theoretically and experimentally. However, a theoretical study by Murphy [24] pointed out that the spin–lattice relaxation rate of paramagnetic electron states located near ionic tunneling systems that undergo localized motion in SiO_2 can cause the spin–lattice relaxation rate temperature dependence to significantly weaken from the usual quadratic temperature behavior observed without the ionic impurities, towards a linear dependence. To our knowledge, the high–[E'] SiO_2 studied here does not contain any ionic impurities, it is conceivable though that the defect–induced, highly underconstrained character of the continuous random network allows for local motion of the network constituents, including those at which the E' states are located. Furthermore, the E' center can also assume local mobility by undergoing tunnel transitions between different bonding sites [24], causing a weakening of the weak temperature dependence similar to the motion of ionic species. In essence, we conclude that the weak temperature dependence of T_1 is caused by local motion effect due to rocking, wagging, and stretching of bonds in the vicinity of the E' states or mobility of the E' states.

We notice that silicon dangling bond relaxation processes have been studied to a greater extend in amorphous silicon (a-Si) networks, even though the analogy between amorphous silicon and amorphous SiO_2, is limited, given the abundance of hydrogen in most a-Si materials and the significantly different band structure which caused spin relaxation in a-Si to be affected by electronic mobility effects which do not exist in SiO_2 [11].

Effects of silicon dangling bond densities on the temperature dependencies of spin–lattice relaxation times of silicon dangling bond states in a-Si have been reported before by Stutzmann and Biegelsen [33]. In this work, the dangling bond density was adjusted by thermal annealing, yet in contrast to the study presented here on SiO_2, the anneal caused increases of dangling bond densities due to proton effusion. Similar to our observations reported here, Stutzmann and Biegelsen observed a decrease of the ratio between low–temperature and room–temperature T_1 values for very high

dangling bond densities and similar to the predictions of Murphy [24] for SiO_2, this effect was attributed to spin motion, yet not localized motion but spin diffusion. A study of continuous wave EPR detected silicon dangling bond line width in disordered silicon by Nickel and Schiff [25] also revealed a weak and, therefore, an unconventional temperature dependence for samples with high ($\approx 10^{18}$cm^{-3}) dangling bond densities.

While we stress that it is not clear to what extent the spin–lattice relaxation dynamics of silicon dangling bonds in disordered silicon is comparable to disordered SiO_2, we again conclude that the hypothesis that local motion effects caused by the underconstrained network, combined with increased spin–spin interactions due to the decreased average E' center distances, is consistent with the observed different longitudinal spin–relaxation behaviors at high and low values of [E'].

For the assessment of whether or not the E' center spin–relaxation times of high-[E'] SiO_2 presented here render the E' center suitable for their application as probe spins within for SSTFM described by Payne et al. [27], we reiterate that since spin–detection using this concept is based on the discrimination of random telegraph noise powers caused by a change of the noise power spectra under magnetic resonance, the intrinsic spin–flip rate of a probe spin is limited by the longitudinal spin relaxation time T_1 in absence of magnetic resonance, while the spin–flip rate is governed by the resonant driving field B_1 on-resonance. Thus, next to the geometric requirements of the probe spins discussed above (high localization, presence of a single center at the probe tip), the suitability of a paramagnetic state as probe spin requires that $T_1 > \gamma B1$ with γ being the electrons gyromagnetic ratio. The magnitude of T_2 poses no limitation for the readout concept since spin–phase loss has no effect on the projective measurement of a coherent spin–pair state onto an spin–pair eigenstate. For technologically straightforwardly achievable driving fields in a scanning probe setup of $B_1 \approx 0.1\mu$T, this requires $T_1 >\sim 0.1$ms. We therefore conclude that E' centers, even at the highest densities reported here and room temperature, posses adequate spin relaxation properties as spin probes for the SSTFM–based single–spin–readout proposed by Payne et al. [27].

3.8 Summary and conclusions

The suitability of the spin–relaxation dynamics of E' centers within 60nm thin amorphous SiO_2 layers for the application of E' centers as probe spins for SSTFM has been studied. The experiments have shown that for SiO_2, with Ar^+ ion plasma induced optically and chemically stable densities of $[E'] > 5 \times 10^{18}\text{cm}^{-3}$, the transverse spin–relaxation time displays an average $T_2 = 552(15)$ns, with no significant dependence on the temperature between $T = 5$K and $T = 70$K. Within the same temperature range, the spin-lattice relaxation time (T_1) exhibits a slightly stronger, yet compared to low–[E'] SiO_2, nevertheless weak temperature dependence. By extrapolation of this weak temperature dependence of T_1 to room temperature through an Arrhenius function, a room temperature value of $T_1 \approx 195(5)\mu$s is found, in good agreement with literature values for low–[E'] SiO_2. At $T = 5$K, $T_1 = 625(51)\mu$s, which is significantly shorter than the low–[E'] $T_1 \approx 1s$[6].

We conclude that the observed T_1 and T_2 times as well as the long–term stability of the E' center at high–density makes this defect an excellent candidate for applications as probe–spin in the spin–selection rule based force–detected SSTFM scheme proposed by Payne et al. [27]. SSTFM using E' centers may allow for suitable readout approaches for silicon based spin quantum information or spintronics applications, even at room temperature where for technologically achievable spin resonant driving fields, T_1 is required to exceed 100μs.

3.9 References

[1] K. Ambal, A. Payne, D. P. Waters, C. C. Williams, and C. Boehme. Spin-relaxation dynamics of E' centers at high density in SiO_2 thin films for single-spin tunneling force microscopy. *Phys. Rev. Applied*, 4:024008, 2015.

[2] N. M. Atherton. Principles of electron spin resonance, Ellis Horwood PTR Prentice Hall. 1993.

[3] M. Bode, M. Heide, K. von Bergmann, P. Ferriani, S. Heinze, G. Bihlmayer, A. Kubetzka, O. Pietzsch, S. Blugel, and R. Wiesendanger. Chiral magnetic order at surfaces driven by inversion asymmetry. *Nature*, 447:190, 2007.

[4] C. Boehme and K. Lips. Spin-dependent recombination − an electronic readout mechanism for solid state quantum computers. *Phys. Status Solidi B*, 233:427, 2002.

[5] C. Böhme. *Dynamics of Spin-Dependent Charge Carrier Recombination.* Cuvillier, 2003.

[6] J. G. Castle and D. W. Feldman. Temperature dependence of paramagnetic relaxation at point defects in vitreous silica. *J. Appl. Phys.*, 36:124, 1965.

[7] J. G. Castle, D. W. Feldman, P. G. Klemens, and R. A. Weeks. Electron spin-lattice relaxation at defect sites; E′ centers in synthetic quartz at 3 kilo-Oersteds. *Phys. Rev.*, 130:577, 1963.

[8] S. S. Eaton and G. R. Eaton. Irradiated fused-quartz standard sample for time-domain EPR. *J. Magn. Reson. Ser. A*, 102:354, 1993.

[9] F. Finger, J. Müller, C. Malten, and H. Wagner. Electronic states in hydrogenated microcrystalline silicon. *Phil. Mag. B*, 77:805, 1998.

[10] B. T. Ghim, S. S. Eaton, G. R. Eaton, R. W. Quine, G. A. Rinard, and S. Pfenninger. Magnetic field and frequency dependence of electron spin relaxation times of the E′ center in irradiated vitreous silica. *J. Magn. Reson. Ser. A*, 115:230, 1995.

[11] N. J. Harmon and M. E. Flattè. Spin relaxation in materials lacking coherent charge transport. *Phys. Rev. B*, 90:115203, 2014.

[12] T. W. Herring, S.-Y. Lee, D. R. McCamey, P. C. Taylor, K. Lips, J. Hu, F. Zhu, A. Madan, and C. Boehme. Experimental discrimination of germinate and non-germinate recombination in *a*-Si:H. *Phys. Rev. B*, 79:195205, 2009.

[13] Y. Ichihashi, Y. Ishikawa, Y. Kato, R. Shimizu, M. Okigawa, and S. Samukawa. Effects of thermal annealing for restoration of UV irradiation damage during plasma etching processes. *Jpn. J. Appl. Phys.*, 45:8370, 2006.

[14] M. Ikeya, H. Kohno, S. Toyoda, and Y. Mizuta. spin spin relaxation time of E′ center in neutron radiated quartz. *Jpn. J. Appl. Phys.*, 31:1539, 1992.

[15] Y. Ishikawa, M. Okigawa, S. Samukawa, and S. Yamasaki. Reduction of plasma-induced damage in SiO_2 films during pulse-time-modulated plasma irradiation. *J Vac. Sci. Technol. B*, 23:389, 2005.

[16] U. Kaiser, A. Schwarz, and R. Wiesendanger. Magnetic exchange force microscopy with atomic resolution. *Nature*, 446:522, 2007.

[17] P. M. Lenahan and J. F. Conley. What can electron paramagnetic resonance tell us about the Si/SiO_2 system. *J. Vac. Sci. Technol. B*, 16:2134, 1998.

[18] P. M. Lenahan and P. V. Dressendorfer. An electron spin resonance study of radiation-induced electrically active paramagnetic centers at the Si/SiO_2 interface. *J. Appl. Phys.*, 54:1457, 1983.

[19] P. M. Lenahan and J. J. Mele. E' centers and leakage currents in the gate oxides of metal oxide silicon devices. *J. Vac. Sci. Technol. B*, 18:2169, 2000.

[20] G. Lucovsky, Y. Wu, H. Niimi, V. Misra, and J. C. Phillips. Bonding constraints and defect formation at interfaces between crystalline silicon and advanced single layer and composite gate dielectrics. *Appl. Phys. Lett.*, 74:2005, 1999.

[21] C. Malten, J. Mueller, and F. Finger. Pulsed ESR studies on doped microcrystalline silicon. *Phys. Stat. Solidi B*, 201:R15, 1997.

[22] H. J. Mamin et al. Nanoscale nuclear magnetic resonance with a nitrogen-vacancy spin sensor. *Science*, 339:557, 2013.

[23] A. Morello et al. Single-shot readout of an electron spin in silicon. *Nature*, 467:687, 2010.

[24] J. Murphy. Spin-lattice relaxation due to local vibrations with temperature-independent amplitudes. *Phys. Rev.*, 145:241, 1966.

[25] N. H. Nickel and E. A. Schiff. Direct observation of dangling bond motion in disordered silicon. *Phys. Rev. B*, 58:1114, 1998.

[26] S.-Y. Paik, S.-Y. Lee, W. J. Baker, D. R. McCamey, and C. Boehme. T_1 and T_2 spin relaxation time limitations of phosphorous donor electrons near crystalline silicon to silicon dioxide interface defects. *Phys. Rev. B*, 81:075214, 2010.

[27] A. Payne, K. Ambal, C. Boehme, and C. C. Williams. Atomic-resolution single-spin magnetic resonance detection concept based on tunneling force microscopy. *Phys. Rev. B*, 91:195433, 2015.

[28] J. R. Petta et al. Coherent manipulation of coupled electron spins in semiconductor quantum dots. *Science*, 309:2180, 2005.

[29] J. C. Phillips and M. F. Thorpe. Constraint theory, vector percolation and glass formation. *Solid State Commun.*, 53:699, 1985.

[30] D. Rugar, R. Budakian, H. J. Mamin, and B. W. Chui. Single spin detection by magnetic resonance force microscopy. *Nature*, 430:329, 2004.

[31] A. Schweiger and G. Jeschke. *Principles of Pulse Electron Paramagnetic Resonance*. Oxford University Press, Oxford, 2001.

[32] A. R. Stegner, C. Boehme, H. Huebl, M. Stutzmann, K. Lips, and M. S. Brandt. Electrical detection of coherent ^{31}P spin quantum states. *Nat. Phys.*, 2:835, 2006.

[33] M. Stutzmann and D. K. Biegelsen. Electron-spin-lattice relaxation in amorphous silicon and germanium. *Phys. Rev. B*, 28:6256, 1983.

[34] R. A. Weeks, R. H. Magruder, and A. Stesmans. Review of some experiments in the 50 year saga of the E$'$ center and suggestions for future research. *J. Non-Cryst. Solids*, 354:208, 2008.

[35] R. A. Weeks, R. and C. M. Nelson. Trapped electrons in irradiated quartz and silica: II, electron spin resonance. *J. Am. Ceram. Soc.*, 43:399, 1960.

[36] R. Wiesendanger. Spin mapping at the nanoscale and atomic scale. *Rev. Mod. Phys.*, 81:1495, 2009.

[37] J. Wrachtrup, C. von Borczyskowski, J. Bernard, M. Orritt, and R. Brown. Optical detection of magnetic resonance in a single molecule. *Nature*, 363:244, 1993.

[38] K. Yokogawa, Y. Yajima, T. Mizutani, S. Nishimatsu, and K. Suzuki. Positive charges and E$'$ centers formed by vacuum ultraviolet radiation in SiCH grown on Si. *Jpn. J. Appl. Phys.*, 29:2265, 1990.

[39] M. E. Zvanut, R. E. Stahlbush, and W. E. Carlos. Radiationinduced E$'$ centers in H_2 annealed oxide films. *Appl. Phys. Lett*, 60:2989, 1992.

CHAPTER 4

IN–SITU ABSOLUTE MAGNETOMETRY IN A UHV SCANNING PROBE MICROSCOPE BASED ON A CONDUCTING POLYMER THIN–FILM

With the availability of a suitable paramagnetic probe state for SSTFM, as discussed in the previous chapter, the challenge of combining a scanning probe microscope with a magnetic resonance setup can be addressed. Thus, in this chapter, a detailed description is given about the implementation and calibration of two mutually perpendicular magnetic field coils into a commercial scanning probe microscope. For this, the in-situ measurement and control of the direction and magnitude of the magnetic field within the sample plane of a low–temperature ultra–high–vacuum scanning probe microscope is demonstrated using electrically detected magnetic resonance magnetometry based on the spin–dependent recombination current in a conducting polymer–thin film. The presented magnetometry approach allows the absolute measurement of systematic magnetic offset fields with a resolution on the order of $\approx 5\mu\mathrm{T}\sqrt{\mathrm{Hz}}$ with an angular resolution below $\approx 1°$. As the polymer film covers a macroscopic area within the sample plane, magnetometry becomes possible at various locations within the sample plane and thus, the determination of magnetic field gradients. This work was implemented in collaboration with A. Payne, C. C. Williams, and C. Boehme and will be submitted for publication.

4.1 Introduction

In recent years, scanning probe microscopy techniques have increasingly been applied to experiments which require the controlled application and the spatially

resolved detection of magnetic fields [6, 8, 15, 3, 11, 16, 5, 14, 13]. In this context, accurate local magnetometry as well as magnetic field control (with regard to the field direction, magnitude, and homogeneity) has remained a challenge due stray magnetic fields from probe and sample supports, sample stages using eddy current damping, and other spurious magnetic field sources that can be present in scanning probe instrument. The stronger the gradients of such stray magnetic fields, the more difficult the assessment of how accurately a magnetometer readout made in close proximity to a scanning probe corresponds to the conditions right at the scanning probe apex. Thus, magnetic field control for scanning probe experiments requires that the distance between the probe apex and the magnetic field sensor be minimized, that the magnetometer be ideally located within the sample plane where the scanning probe experiments takes place, and that the measurement of the magnetic field be monitored at more than one, possibly many locations in order to allow for the observation of a magnetic field gradient. To fulfill these requirements, a magnetometer should ideally be located on the scanning probe, right at or close to the probe apex. This is difficult to achieve with conventional magnetometer implementations based on Hall probes, magnetic tunnel junctions, or squid structures while the currently existing in–probe mangetometer approach that is based on NV centers [14] confines the range of possible probe materials to diamond, a good insulator.

In the following, we present and demonstrate a different magnetic field detection scheme for scanning probe experiments that is based on the application of magnetic resonance based magnetometry to spin-dependent currents through polymer thin-film layers. Spin–dependent transport and recombination currents in various organic semiconductors have extensively been studied in the past and it has recently been shown [1] that these currents, when manipulated by magnetic resonant excitation, can be utilized for highly accurate absolute magnetometry. Using this approach, it is possible to obtain robust absolute magnetic field measurements from the locations where a spin–dependent charge current percolates. Since conducting scanning probes are excellent current detection devices that can be moved laterally across the sample surface, lateral magnetic field distributions can be obtained with magnetic resonant magnetometry as long as an appropriate polymer thin–film material is distributed

in close proximity of the sample surface. Organic semiconductor layers can be thin (<100nm), yet they can extend laterally across macroscopically large areas. Magnetic field measurements therefore become possible wherever a scanning probe can touch the sensor surface. Furthermore, as shown below, the combination of this magnetometery approach with the application of additional, inductively generated magnetic offset fields also allows for the determination of the direction of background magnetic fields as well as the control of the net magnetic field.

4.2 Experiment

Figure 4.1(a) displays a sketch of the low–temperature scanning probe setup (Omicron Nanotechnology LT STM with qplus) [4] as well as a sketch of the organic layer stack that was used for the acquisition of the data presented in the following. The qplus probe allows for electrical frequency detection and, therefore, to conduct experiments in complete darkness such that no photoexcited charge carrier can exist. The cantilever is made out of a piezoelectric quartz that is cut into a small tuning fork (q-plus) as shown in Fig. 4.2. One arm of this tuning fork is fixed while the other is free to oscillate. When the free arm of the tuning fork oscillates, charge builds up across the opposite surface due to the piezoelectric effect. Therefore, a small potential difference appears across the surface that can is amplified by a pre-amplifier located right next to the cantilever as shown in Fig. 4.2. The physical dimensions of the cantilever are 2.5mm x 0.2mm x 0.07mm (length x width x height). The stiffness/spring–constant is $\approx$ 1000N/m. The cantilever typically oscillates at a frequency of $\approx$ 30KHz with a typical oscillation amplitude $\approx$ 1nm. A superconductive coil is present for the generation of an externally applied static magnetic field ($\vec{B}_a$) that is perpendicular to the scanning probe's sample plane. Perpendicular to the coil axis, therefore parallel to the sample plane, is a copper coil with 3mm diameter for the generation of an oscillating radio frequency (RF) magnetic field $\vec{B}_1$ with amplitude B_1 and frequency ν, as needed to establish magnetic resonance. The symmetry axis of this coil defines the magnetic field plane in which magnetometry becomes possible. This so-called detection plane is perpendicular to the RF–coil axis. Figure 4.3(a) displays the UHV low–temperature scanning probe microscope. Figure 4.3(b) displays

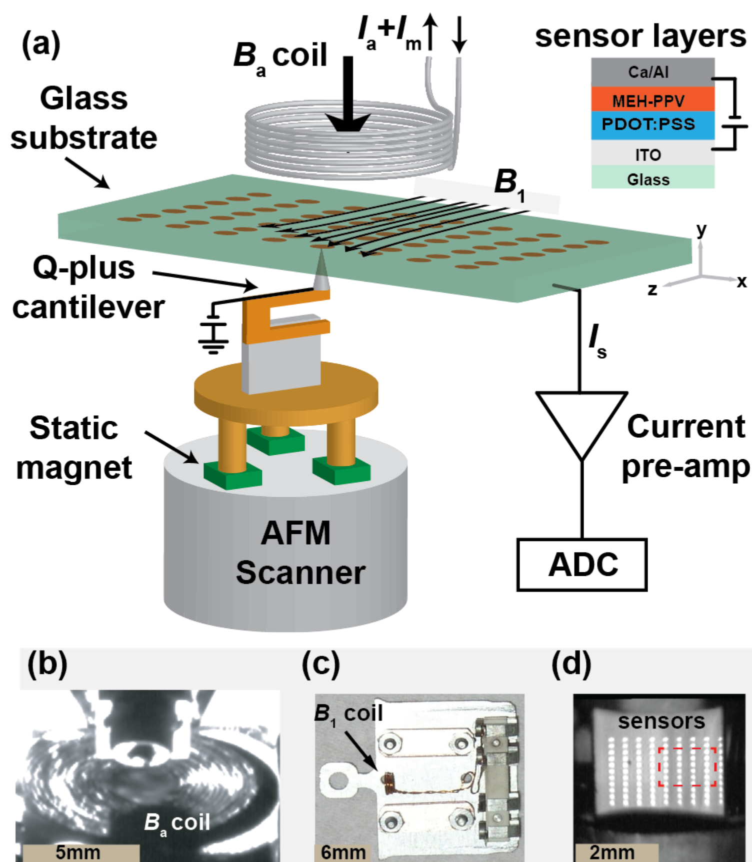

Figure 4.1. Illustration of the experimental setup. (a) Sketch of the experimental setup which combines a scanning probe system with organic semiconductor based magnetic resonance magnetometry. The experiment was based on a low–temperature, ultra–high–vacuum scanning probe setup built by Omicron Nanotechnology GmbH (now ScientaOmicron), controlled by a customized LabView software. The inset described the stack of organic and metal layer used for the generation of spin–dependent currents. (b) Image of the superconducting magnet. (c) Image of the RF coil attached to the sample plate. (d) Image of the sensors and the red box represent the active measurement area.

the superconductive coil which generates the static magnetic field (B_0) that is needed for magnetic resonance while Fig. 4.3(c) displays an image of the sample plate that contains a small coil for the application of the RF radiation.

At operation below its critical temperature, the use of a superconducting magnet prevents the development of thermal gradients within the microscope due to Ohmic heating. Because of this, all experiments presented in the following were conducted at liquid ^{4}He temperature ($T \approx 4.2$K). At higher temperatures, above the critical temperature of the magnet coil, the range of applicable magnetic field strengths to this

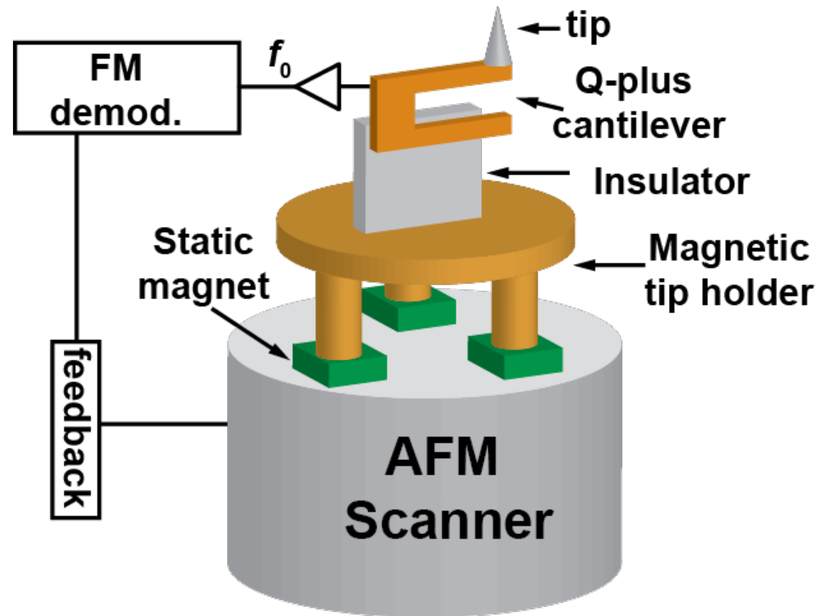

Figure 4.2. Low–temperature scanning probe setup using quartz tuning fork cantilever. The cantilever is glued to an electrically insulating ceramic substrate which in turn is glued to a metal magnetic tip holder. A layer of gold is located on the side of the cantilever in order to collect all the piezo electric charge while the cantilever oscillates vertically. The permanent magnet attached to the scanner keeps the tip holder in place and facilitates the electrical connection to the tip that is needed for the bias application.

instrument is significantly limited for the given scanning probe setup. However, this poses no principal limitation on the magnetometry scheme presented here since the utilization of spin–dependent transitions in MEH-PPV devices at room temperature has been demonstrated before [1].

The organic layer system used for the detection of spin–dependent recombination currents consisted of the π-cojugated polymer poly[2-methoxy-5-(2-ethylhexyloxy)-1, 4-phenyl-enevinylene] (MEH-PPV) as activer layer which was sandwiched between a Poly(3,4-ethyle-nedioxythiophene)-poly(styrenesulfonate)(PEDOT:PSS) hole injecting layer and a Ca electron injecting layer. This layer stack was then deposited onto an indium tin oxide layer on a glass substrate. It constitutes essentially an organic light emitting diode device that we have chosen since spin–dependent recombination currents therein are well understood [10, 9, 7, 2, 12] and have been demonstrated for magnetometry [1]. For the experiments presented here, an array of Ca/Al dots was fabricated across the sample plane as illustrated in panel Fig. 4.1(a). Each of these

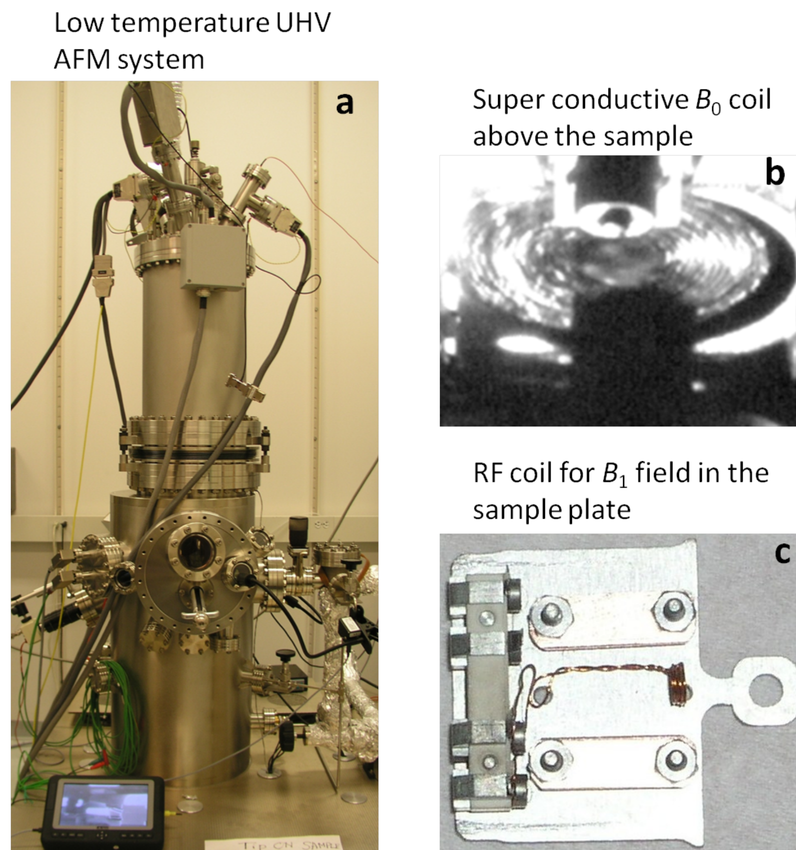

Figure 4.3. Illustration of the low–temperature scanning probe microscope and superconducting magnet with RF coil. (a) Image of the UHV-AFM low–temperature q-plus sensor system. (b) Image of the superconducting magnet above the sample that is used to produce the static magnetic field that is needed to establish magnetic resonance. (c) Image of the four-contact sample plate with a small RF coil added next to the sample for RF excitation

dots has a 100μm diameter and the structures are separated from each other by a 200μm periodicity. The patterning of the stack contacts allows for a confinement of the spin–dependent current to the area covered by the dot. We note that this dot size therefore defines the lateral resolution of magnetic field measurements for the setup, which sets a lower limit on the size of magnetic field fluctuations that can be detected with this magnetometry approach. Figure 4.1(b) and (c) are the images of the superconducting magnet, the RF coil, and the thin–film array, respectively. The bottom electrode of the sensor films was connected electrically to the sample plate while the electrical contact at the top electrode was established by physics contact between the dot and a Pt probe connected to a quartz tuning folk (qplus) sensor as

shown in Fig. 4.1(a).

4.3 Field calibration and vector magnetometry

Electric characterization of the sensor layer was conducted by measurement of the current voltage characteristics. For this, a forward DC bias was applied between the probe and the sample layer stack and swept slowly. The resulting data are shown in Fig. 4.4(f). A constant forward bias and thus, a DC offset current (the probe current I) was then applied to the sensor layer while another DC current I_a was applied to the superconducting coil together with a superimposed, harmonically oscillating magnetic modulation current with amplitude I_m. Together, the two superimposed DC and AC currents produced a static magnetic field and a harmonically oscillating modulation field, whose components perpendicular to the axis of the RF–field coil are denoted $B_a = \alpha I_a$ (the applied magnetic field) and $B_m = \alpha I_m$, (the modulation amplitude), respectively. The variable α describes the proportionality constant between B_a and I_a that is dictated by Ampere's law.

Lock–in detected changes of ΔI to the sample current I caused by changes of the spin–dependent charge carrier recombination rate were recorded as a function of I_a in presence of a fixed RF field with frequency ν. The amplitude of the RF field was chosen such that the observed spin–dependent current change became maximal. This was achieved with an RF power of 50 mW. Under magnetic resonance, the probe current change ΔI as a function of I_a is nonvanishing and thus, the lock–in detected derivative function $\left[\partial\Delta I\left(B_n^{\perp}\right)/\partial B_n^{\perp}\right]B_m$ becomes nonvanishing, too. Examples for the observation of this behavior for various values of ν are shown in Fig. 4.4(a) to (e). The obtained data reveal directly the magnitude $B_n^{\perp}$ of the measured net–magnetic field component in the detection plane that is perpendicular to $\vec{B}_1$ at the percolation regions of the probe current for those coil current values I_a where the derivative function $\left[\partial\Delta I\left(B_n\right)/\partial B_n\right]B_m$ crosses its baseline. Note that the baseline is not vanishing due to the finite slope of $\Delta I(B_n^{\perp})$ caused by the well–known organic magnetoresistance (OMAR) [12]. Magnetic resonance occurs when the applied RF photon energy $h\nu$ and the Zeeman energy $h\gamma B_n$ are equal with h being the Planck constant and $\gamma = 28.03(4)\text{GHz/T}$ the gyromagnetic ratio of charge carriers in MEH-

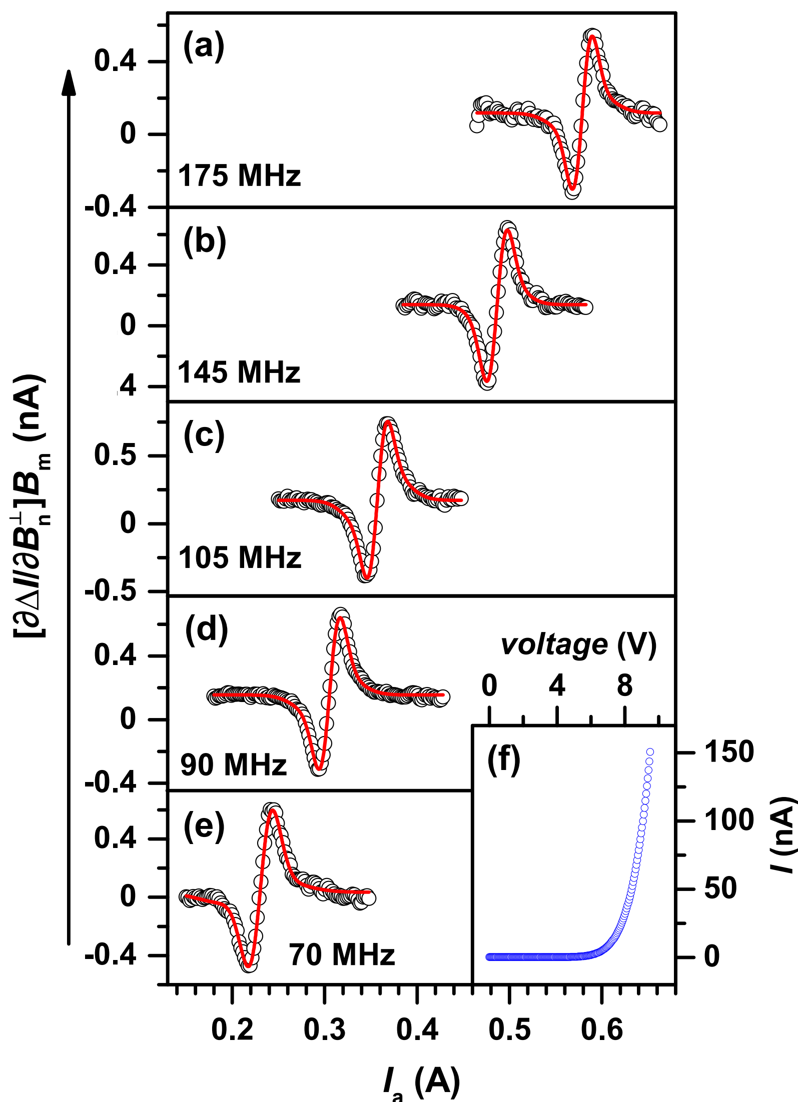

Figure 4.4. Lock-in detected derivative functions of ΔI as functions of I_a, recorded for various RF frequencies between 70MHz and 175MHz. The applied DC current I_a was superimposed with a harmonic AC current with amplitude $I_m = 25$ mA in order to generate both a static magnetic field and a small modulation needed for lock-in detection. The modulation frequency $f = 30$Hz while $I_m = 25$mA. The inset represents the forward curves of the probed organic thin–film patches. The operating bias of the sensor layer for all measurements was kept consistently at a voltage $V = 9$V.

PPV [1]. Thus, the magnitude of the net magnetic field component in the detection plane perpendicular to $\vec{B}_1$ (which is given by the symmetry axis of the RF coil), can be determined by $B_n^{\perp} = \nu/\gamma$.

The net magnetic field $\vec{B}_n = \vec{B}_a + \vec{B}_0$ is the sum of the background magnetic field $\vec{B}_0$ and the applied magnetic field $\vec{B}_a$. The components $\vec{B}_i^{\perp}$ of these magnetic fields that lie in the detection plane add up in a similar way and since $\vec{B}_a$ does not have out–of detection plane components, implying that $\vec{B}_a = \vec{B}_a^{\perp}$, we know that $\vec{B}_n^{\perp} = \vec{B}_a + \vec{B}_0^{\perp}$. Following the cosine theorem, we therefore know that the magnitudes $B_n^{\perp}$, B_a, and $B_0^{\perp}$ are related by $(B_n^{\perp})^2 = B_a^2 + (B_0^{\perp})^2 + 2B_nB_0^{\perp}\cos\theta$ and thus, $(B_n^{\perp})^2 = \alpha^2 I_a^2 + (B_0^{\perp})^2 + 2\alpha I_a B_n \cos\theta$ (1) with θ denoting the angle between $\vec{B}_0^{\perp}$ and $\vec{B}_a$ within the detection plane. A repeated measurement of $B_n^{\perp}$ for different ν and thus, different I_a as described in Fig. 4.4 will therefore allow us to fully determine α, θ and $B_0^{\perp}$. Figure 4.5(a) displays a plot of various measured $(B_n^{\perp})^2$ and the corresponding values of I_a obtained from the fits of the experimental data in Fig. 4.4 with Gaussian derivative functions. The plot in Fig. 4.5(a) is fitted with Eq.(1), revealing $B_0^{\perp} = 1.72(3)$mT, $\alpha = 11.78(4)$mT/A, and $\theta = 63.1(8)^o$.

Due to the random orientation of $\vec{B}_0^{\perp}$ relative to $\vec{B}_a$, the knowledge of θ allows for the decomposition of $\vec{B}_0^{\perp} = B_0^x\hat{x} + B_0^y\hat{y}$ into its $\hat{x}$- and $\hat{y}$-components along the directions in the detection plane that are perpendicular and parallel to the sample plane, respectively [see illustration in the inset of Fig. 4.5(a)]. For the data presented in Fig. 4.5(a), this implies that $B_0^x = 1.54(3)$mT and $B_0^y = -0.78(2)$mT. This trigonometric decomposition can be tested by comparison of the obtained $\hat{x}$-component with the minimally attainable magnetic field for $B_n^{\perp}$: Since $\vec{B}_a \parallel \hat{y}$, the $\hat{y}$-component of $\vec{B}_0^{\perp}$ can be fully compensated by application of an appropriate current I_a (which minimizes $B_n^{\perp}$), while the $\hat{x}$-component remains unchanged for any I_a (which is why $B_n^{\perp}$ can never vanish completely as long as $B_0^x \neq 0$). For the measurements in Fig. 4.5(a), the fit result reveals that for $B_a = 0.78(3)$mT (at $I_a = 66.1968$mA), this minimum of $B_n^{\perp}$ is reached. Furthermore, since minimizing $B_n^{\perp}$ implies minimizing the magnitude of the overall net-magnetic field $\vec{B}_n$, the magnetocurrent response ΔI of the polymer device should also be minimized. Figure 4.5(b) and (c) display this effect. Panel (b) displays lock–in detected derivative spectra of ΔI recorded at

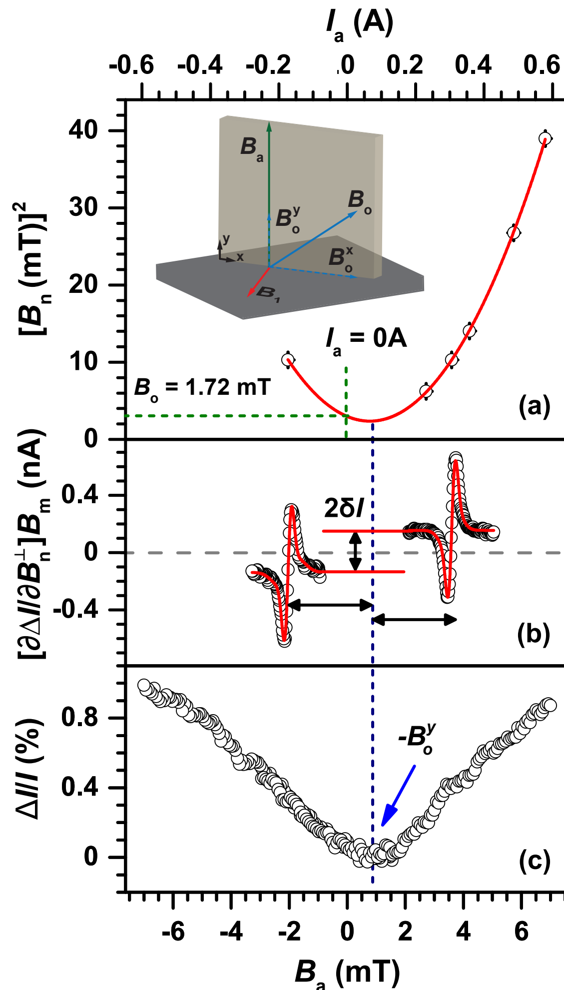

Figure 4.5. Determination of the offset magnetic field and its direction. (a) Plot of B_n^2 as a function of the on–resonance coil current I_a for the different RF excitation frequencies ν displayed in Fig. 4.4. The red line represents a fit of the data with Eq. (1). The green lines indicate the strength of the offset magnetic field $B_0^{\perp}$ in absence of a coil current ($I_a = 0$). The inset sketch illustrates and defines the different magnetic field contributions and its relative orientation to the RF field. Note that $\vec{B}_a$ is oriented such that it lies fully within the detection plane defined by the direction of $\vec{B}_1$. (b) Plot of the lock–in detected derivative function of the current change for a fixed RF frequency ν =90 MHz after I_a was swept with a positive and negative domain. The shifts of the baselines $\pm\delta I$ are cause by the nonvanishing slope of the current change due to organic magnetoresistance [12]. This finite slope is confirmed the measurement of the $\Delta I(I_a)$ that is plotted in (c). The fit results displayed in (a) reveal that the smallest achievable value of B_n is 0.78(1)mT occuring when $B_0^{\perp}$ is maximally compensated and the magnetocurrent ΔI reaches a minimum.

the same RF frequency $\nu = 90$MHz for positive and negative net fields $\vec{B}_0^{\perp}$. The spectra display positive and negative baseline offsets of an identical magnitude $\pm\delta I$ indicative of magnetoresistance of the polymer layer which is symmetric around the point that averages the resonance centers of the two derivative spectra. Indeed, this average occurs at $B_a = 0.78(2)$mT, in agreement with the value at which $B_n^{\perp}$ is minimized. Finally, direct recording of the device magnetoresistance displayed in Fig. 4.5(c) confirms the current minimum again at $B_a = 0.78(1)$mT.

4.4 Distribution of magnetic field

Following the demonstration of the electrically detected magnetic resonance magnetometry concept presented here, we have repeated the procedure for the determination of $B_x^{\perp}$, $B_y^{\perp}$, α, and θ at various points across the sample plane, for the $\hat{x}$- and $\hat{z}$-directions within a rectangular area of 1.5mm $\times$ 0.9mm with spacings governed by the Al dot array. The results of these measurements and their error bars are displayed in Fig. 4.6. They show that gradient fields caused by both the background field sources as well as the magnetic field coil (reflected by the current to field conversion factor α) can be determined with a sensitivity limit for gradient fields of 4.3 mT/m and 44 mT/m for the sensors located at z = 0mm and 0.9mm, respectively, limited by the size of the scanned area and the sensitivity of the magnetometry procedure that was determined to be $\approx 5\mu\mathrm{T}\sqrt{\mathrm{Hz}}$ and $\approx 53\mu\mathrm{T}\sqrt{\mathrm{Hz}}$ for the sensor located at z = 0mm and 0.9mm, respectively, determined from the noise power of the current, following a procedure described by Baker et al. [1]. The different sensitivity of the sensors at z= 0mm and 0.9mm is due to the decay of the RF field and, therefore, the spin dependent current change (EDMR single). Thus, the signal-to-noise (SNR) of the farthest sensors (z = 0.9mm) is poor compared to the sensors located close to the RF coil.

4.5 Conclusions and summary

In conclusion, we have demonstrated the ability to measure the strength and orientation of magnetic fields for arbitrary locations within the sample plane of a low–temperature, ultra–high–vacuum scanning probe microscope by using localized induced currents in a thin polymer layer. The measurement approach allows for the

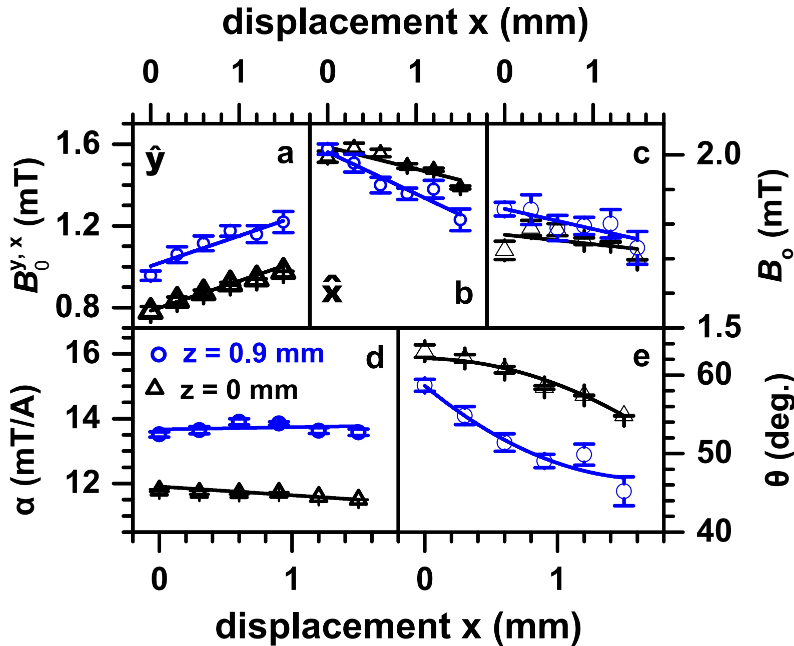

Figure 4.6. Plots of α (a), $B_0^{\perp}$ (b), θ (c), B_0^x (d), and B_0^y (e) as functions of the $\hat{x}$- and $\hat{x}$-coordinates within a 1.5mm x 0.9mm large area of the sample plane. The solid line represent guides to the eyes. The data allow the determination of magnetic field gradients of both $B_0^{\perp}$ as well as B_a (through α and the applied coil current I_a.

determination of lateral magnetic fields and gradients. In this study, the magnetic field vector $\vec{B}_0$ was determined only for the two components within the detection plane that is perpendicular to the symmetry axis of the RF coil. This poses no principal limitation of the presented magnetometry scheme. Any magnetic field component of $\vec{B}_0$ can be probed by rotation of the direction of $\vec{B}_1$, e.g., by a second RF coil whose symmetry axis is perpendicular to the symmetry axis of the first RF coil. Similarly, the low–temperature experiments presented here do not imply a limitation of the presented magnetometry concept to this temperature domain. Spin–dependent current in organic semiconductors exists over a wide temperature range, including room temperature [1].

Finally, we note that for the application of this magnetometry scheme to arbitrary scanning probe microscopy, a sample should either be mounted on top of the polymer layer or alternatively, the polymer film should be deposited on the same substrate as the investigated microscopy sample.

4.6 References

[1] W. J. Baker, K. Ambal, D. P. Waters, R. Baarda, H. Morishita, K. S. van Schooten, D. R. McCamey, J. M. Lupton, and C. Boehme. Robust absolute magnetometry with organic thin-film devices. *Nat. Commun.*, 3:898, 2012.

[2] W. J. Baker, T. L. Keevers, J. M. Lupton, D. R. McCamey, and C. Boehme. Slow hopping and spin dephasing of coulombically bound polaron pairs in an organic semiconductor at room temperature. *Phys. Rev. Lett.*, 108:267601, 2012.

[3] C. Durkan and M. E. Welland. Electronic spin detection in molecules using scanning-tunneling- microscopy-assisted electron-spin resonance. *App. Phys. Lett.*, 80:458, 2002.

[4] F. J. Giessibl. High-speed force sensor for force microscopy and profilometry utilizing a quartz tuning fork. *Appl. Phys. Lett.*, 73:3956, 1998.

[5] K. Klein, B. Hauer, B. Stoib, M. Trautwein, S. Matich, H. Huebl, O. Astakhov, F. Finger, R. Bittl, M. Stutzmann, and M. S. Brandt. The electrically detected magnetic resonance microscope: Combining conductive atomic force microscopy with electrically detected magnetic resonance. *Rev. Sci. Instrum.*, 84:103911, 2013.

[6] I. Lee, Y. Obukhov, J. Kim, X. Li, N. Samarth, D. V. Pelekhov, and P. C. Hammel. Local magnetic characterization of (Ga, Mn)As continuous thin film using scanning probe force microscopy. *Phys. Rev. B*, 85:184402, 2012.

[7] S.-Y. Lee, S.-Y. Paik, D. R. McCamey, J. Yu, P. L. Burn, J. M. Lupton, and C. Boehme. Tuning hyperfine fields in conjugated polymers for coherent organic spintronics. *J. Am. Chem. Soc.*, 133:2019, 2011.

[8] Y. Martin and H. K. Wickramasinghe. Magnetic imaging by force microscopy with 1000 resolution. *App. Phys. Lett.*, 50:1455, 1987.

[9] D. R. McCamey, S.-Y. Lee, S.-Y Paik, J. M. Lupton, and C. Boehme. Hyperfine-field-mediated spin beating in electrostatically bound charge carrier pairs. *Phys. Rev. Lett.*, 104:017601, 2010.

[10] D. R. McCamey, H. A. Seipel, S.-Y. Paik, M. J. Walter, N. J. Borys, J. M. Lupton, and C. Boehme. Spin rabi flopping in the photocurrent of a polymer light-emitting diode. *Nat. Mater.*, 7:723, 2008.

[11] S. Müllegger, S. Tebi, A. K. Das, W. Schöfberger, F. Faschinger, and R. Koch. Radio frequency scanning tunneling spectroscopy for single-molecule spin resonance. *Phys. Rev. Lett.*, 113:133001, 2014.

[12] T.D. Nguyen, G. Hukic-Markosian, F. Wang, L. Wojcik, X.G. Li, E. Ehrenfreund, and Z.V. Vardeny. Isotope effect in spin response of π-conjugated polymer films and devices. *Nat. Mater.*, 9:345, 2010.

[13] A. Payne, K. Ambal, C. Boehme, and C. C. Williams. Atomic-resolution single-spin magnetic resonance detection concept based on tunneling force microscopy. *Phys. Rev. B*, 91:195433, 2015.

[14] M. Pelliccione, B. A. Myers, L. M. A. Pascal, A. Das, and A. C. Bleszynski Jayich. Two-dimensional nanoscale imaging of gadolinium spins via scanning probe relaxometry with a single spin in diamond. *Phys. Rev. Applied*, 2:054014, 2014.

[15] D. Rugar, R. Budakian, H. J. Mamin, and B. W. Chui. Single spin detection by magnetic resonance force microscopy. *Nature*, 430:329, 2004.

[16] R. Wang, S. W. King, and C. C. Williams. Atomic scale trap state characterization by dynamic tunneling force microscopy. *Appl. Phys. Lett.*, 105:052903, 2014.

CHAPTER 5

ELECTRICAL CURRENT THROUGH INDIVIDUAL PAIRS OF PHOSPHORUS DONOR ATOMS AND SILICON DANGLING BONDS

The following chapter is focused on the investigation of single phosphorus donor electron states in crystalline silicon as well as single silicon dangling bond states at the crystalline silicon to silicondioxide interface. The main motivation behind this study is to find a suitable model system for which SSTFM can be demonstrated. The P donor system was chosen because it is paramagnetic in its ground state at liquid helium-4 temperatures and the silicon dangling bond was chosen because of its high localization [17] and also because of its well–known interaction with the P-donor at the interface of P–doped crystalline silicon to silicondioxide [28]. Both the P donor state as well as the dangling bond state have long spin–relaxation times at low temperatures compared to other defects. In fact, for the P in crystalline silicon donor, both the nuclear spin as well as the donor electron spin are among the most coherent nuclear and electron spin systems found in nature [27], respectively. The nuclear spin has been proposed to be used as qubit in scalable quantum computers [15]. Thus, the work presented in the following chapter is also motivated by the potential use of the P-donor for quantum information concepts. It was conducted in collaboration with P. Rahe, A. Payne, C. C. Williams, and C. Boehme from the University of Utah as well as J. Slinkman from IBM Research Labs who provided the crystalline silicon samples that were used for these experiments.

5.1 Introduction

Progressively longer lasting quantum coherence of impurity nuclear spins in solid state environments have been demonstrated in recent years, with coherence times on the

order of an hour observed for phosphorous (P) donors in crystalline silicon (c-Si)[27], reiterating their excellent suitability for quantum information applications [15]. While progress on the development of individual readout schemes for these silicon based spin qubits has been equally swift [25, 31, 24, 7], the selective electric addressability of individual qubits in qubit arrays that is needed for the control of interactions between qubits via electric fields [15] but also for selective readout using spin-selection rules [28] still poses a challenge. Due to the strong modulation of P qubit states by the c-Si lattice[32], establishing such controllable electrical contact to individual P-donor states requires techniques that allow for an atomic-scale positioning of individual electronic probe states in the proximities of qubits. Scanning probe techniques like atomic force microscopy (AFM) and scanning tunneling microscopy (STM) both provide this accuracy. The latter is based on electric contact to surface and interface states [1] and resolves surface morphologies by keeping a probe current constant through regulation of the probe-to-surface distance. In the following, we report the application of a hybrid scanning probe microscopy technique based on a combination of non-contact AFM and STM, the so-called conduction AFM (c-AFM) for the study of charge conduction through P impurity donors coupled to silicon dbs. When the lateral resolution of the scanning probe permits, wave functions of electronic states that are endpoints of current percolation paths become visible.

5.2 Sample and tip preparation

5.2.1 Conduction AFM

For conduction AFM, the tip-sample interaction is kept constant using the frequency shift Δf of the qPlus sensor as the topography feedback signal during the scanning of the probe laterally over the surface area. While the tip height obtained from this procedure resolves surface morphology, an electric current through electronic states in the substrate within the tunneling range does not resemble morphological information. Instead, for the samples investigated herein, it reveals an image of charge conduction paths which arrive at the sample surface [8, 5, 33]. Depending on the scanning probe resolution, the measured tunneling currents can reveal images of the electronic states (the wavefunction) at the conduction path of electronic states

closest to the scanning probe. While STM is typically based on tunneling currents in the pA to nA range, these measurements reveal average currents in the low fA range. Due to the frequency-shift feedback-controlled probe positioning, mapping the localized current paths with lateral resolutions in the sub-nanometer range is possible.

5.2.2 Probe preparation

The probes used in this study were provided by Rocky Mountain Nanotechnology, LCC. They were fabricated from a solid Pt wire, exhibiting a 20nm tip radius. The tips were glued to one arm of the tuning fork using conductive glue and placed inside the UHV chamber of the scanning probe system. While q-plus sensor is under stable oscillation, STM measurements were performed at 77K on atomically cleaned, 7x7 reconstructed Si (111) surfaces prepared using standard flash-annealed procedure [5], to verify the tip conductivity and sharpness allowing for atomic resolution. When a stable conductive tip was confirmed in this process, the scanning probe setup was cooled to liquid ^{4}He temperature with the sample being inserted in the microscope. The conduction AFM images were then acquired the following day after the setup had reached equilibrium.

5.2.3 Sample preparation

The substrates used in this study were single-side polished, prime grade, Cz grown c-Si wafers with (100) orientation. The wafers were uniformly doped with P yielding room temperature resistivity between 0.08-0.01 ohm-cm for the data presented in the main text. Different densities were used for the concentration control experiments. The wafers were cut into 10 x 1.2 mm pieces and each piece was precleaned with a standard cleaning procedure including a 20 minutes ultra-sonic bath in acetone followed by 20 minutes ultra–sonic bath in IPA, a DI water rinse, and blow drying with pure compressed N_2. All precleaning was done outside the UHV chamber under atmospheric conditions. After precleaning, the sample was clamped onto an Omicron direct-heating molybdenum sample plate and placed inside the scanning probe system. At UHV pressure (≈1x10-10 mBar), the sample was subjected to the main cleaning step involving a thermal annealing. First, the samples were kept for 2h at 550°C

on a heating stage inside the UHV chamber. Thereafter, a constant DC current (≈0.8 to 1.0 Amps) was passed through the sample for about 12 hours, increasing the sample temperature to 400 to 600°C, and followed by a flash anneal during which the DC current inside the sample was increased from 0-4.2 Amps in 0.5 Amps steps at intervals of 5s. At 4.2A, the constant current was maintained for 20-30s before rapid thermal cooling was initiated. The flash process was repeated at least three times, a procedure during which the native oxide at the surface was subsequently removed from the surface and a reconstructed atomically clean flat surface [23, 11, 21] was left behind.

For the native oxide growth, a c-Si (100) substrate was first flash-cleaned as described above and then exposed to ultrahigh-purity compressed oxygen that had been humidified by passing through a water bubbler at 80 ^{o}C. The sample surface was then exposed inside the load lock at ambient pressure with the resulting moist oxygen for two hours at room temperature, a process in which a very thin ≈2-3 native oxide was grown on top of the cleaned silicon surface[16, 30].

Silicon samples with different dopant concentration sample were made from (100) oriented p-type wafers ([B] =5x1014 cm-3) by ion implantation with P atoms at 25keV with an implantation dose of 10^{13}, 10^{14}, and 10^{15} cm^{-2}, respectively. After the ion implantation, a 100nm epitaxially grown layer was grown at 550 ^{o}C for 10 minutes followed by a spike anneal at 1050 ^{o}C for 0.1s at 100% Ar ambient and 30 minutes anneal at 550 ^{o}C at 100% N_2 ambient. Using this technique, three samples with different lower surface concentrations were fabricated which, due to the implanted P layer, still provided the good conductivity needed for the c-AFM experiments. These samples were fabricated and supplied by the Development Laboratory at IBM Microelectronics in Essex Junction, VT.

5.3 Experimental details

The experiments presented here are illustrated in Fig. 5.1(a) showing a schematic of the conduction AFM setup consisting of an Omicron Nanotechnology Oxford Instruments LT STM/AFM system using a quartz tuning fork in qPlus configuration [10] with a clean platinum (Pt) probe tip attached. The tuning fork oscillates at

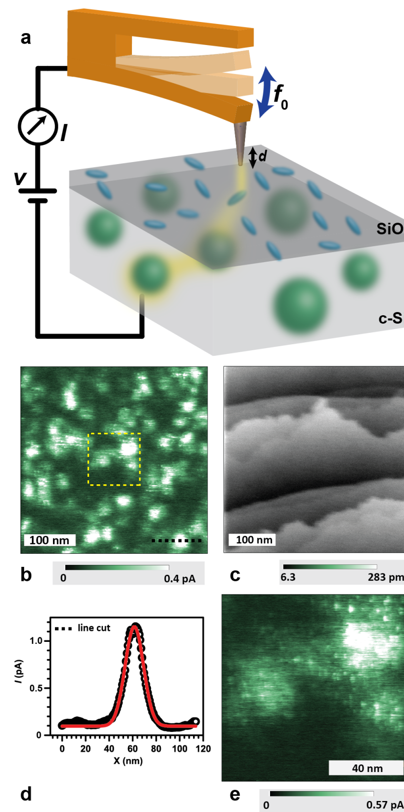

Figure 5.1. Schematic of the low-temperature current imaging experiment conducted on a phosphorus doped silicon substrate. (a) A quartz tuning fork (qPlus sensor) with a Pt tip attached oscillates at $f_0 \approx 30$ kHz. When a bias V is applied to the probe, electrons tunnel from highly localized silicon dangling bond (blue ellipsoids) into the Pt tip. Due to high density of P dopants (indicated by green spheres), the substrate allows for percolation (path indicated by yellow halo) of charges through the bulk. Thus, recharging of the emptied dangling bond state through recombination is possible from a nearby P atom if the donor-dangling bond proximity permits. (b) Current map of a P doped, flash cleaned c-Si substrate without any silicon dioxide at 4.3K in darkness. The bright patches represent the spatial distribution of charge percolation endpoints indicating electronic states consistent with the localization and density of P donor atoms. (c) AFM topography image taken simultaneously using the interaction between surface and probe. The individual step edges are resolved. Note the absence of correlation between the current map and the surface topography. We also note that this AFM topography image displays a very weak, albeit recognizable ghost image in the upper right corner of the imaged area. (d) Line profile of one patch as indicated by the black line in (b). The FWHM of the Gaussian fit (red) of this patch is ≈18nm, corresponding to approximately 3 Bohr diameters of the P donor wave function. (e) High–resolution image of the area indicated by the yellow box in (b). A distinct, seemingly random fine structure for some of the patches attributed to the P donors is visible.

its resonance frequency f_0 with constant amplitude (≈1nm) under UHV conditions ($1x10^{-10}$ mBar) whereby the tip-sample interaction leads to a frequency shift Δf used as the topography feedback signal. In contrast to optically detected AFM, using a quartz tuning fork allows for AFM measurements in the absence of light and thus, photo-charge carriers. The (100) oriented silicon substrate is doped with phosphorous with a dark resistivity of 0.08-0.01 ohm-cm at room temperature and a lower, but still significant dark conductance at 4.3K due to wave function overlap of the neutral P donor states caused by high dopant concentrations ([P]≈ 10^{17}cm^{-3} to 10^{18}cm^{-3}, see sample preparation in the methods section). We investigate pristine as well as oxide-covered (100) surfaces. For the experiments, a positive DC bias is applied to the tip with respect to the back contact of the substrate. The cantilever is then brought in proximity of the sample surface while the interaction between the Pt probe and the surface is measured by observation of Δf. The height feedback controller for the qPlus sensor uses the measured gap-dependent frequency shift to control the height of the probe (constant frequency shift) during imaging, with the assumption that each point of the surface provides an equal interaction with the probe tip. Both the tip and sample are in thermal contact with a liquid He^4 reservoir maintaining a stable temperature of 4.3K.

The image displayed in Fig. 5.1(b) represents the conduction AFM detected surface current distribution (current map) of a pristine, atomically clean silicon sample in darkness. The image reveals several ≈20nm to 30nm large areas (patches) in which localized current maxima are observed. We have calculated the maximal detectable tunneling distance (see Supplemental Information and Ref. [34]) from the probe tip to phosphorus states in the sample to be of the order of approx. three Bohr radii (the Bohr radius of the s-shaped P donor is ≈3nm [32, 2]) and find that both the diameter (FWHM) of these patches, as well as their observed areal density (≈10^{11}cm^{-2} corresponding to ≈10^{17}cm^{-3} with ≈3 Bohr radii accessible probe depth), indicate that the bright regions in the image could be caused by the randomly distributed P donor atoms near the silicon surface. The varying physical dimension and brightness of the patches could be attributed to the varied depths of the P donor atoms.

In order to corroborate that the bright patches seen of Fig. 5.1(b) are due to electronic states rather than surface structure, a surface topography image was measured simultaneously with the data in Fig. 5.1(b), by recording the probe tip height while maintaining a constant frequency shift. The result of this measurement is displayed in Fig. 5.1(c). The image reveals a clean surface with monatomic step edges due to a slight miscut of the silicon sample wafer during the fabrication process. A comparison of panels (b) and (c) in Fig. 5.1 reveals that there is no recognizable correlation between the two images recorded in the same area at the same time. Thus, the features observed in the conduction AFM image must be attributed to localized electronic states.

Figure 5.1(d) displays a line cut (black line) through one of the patches shown in Fig. 5.1(b). The peak current is about 1pA with respect to the current pre-amplifier baseline with ≈18 nm full width of half maximum (FWHM). The half current radius of the patches therefore within approximately three Bohr diameters of the P donor state [32, 2] which further supports the hypothesis that the identified patches are due to P donor atoms. Figure 5.1(e) shows a high–resolution current image taken within the area marked by the yellow box in Fig. 5.1 (b). It resolves some highly localized fine structure of the charge percolation paths within the 10-15 nm broader patch. Two possible explanations are consistent with this observation: (i) the fine structure is due to the crystal periodicity which modulates the electronic wave function of the donor electron [32] and thus, the electric current through this state. (ii) It is due to silicon surface states (e.g., dangling bond (db) states) which exist at very high densities at the pristine silicon surface for which electronic transitions from P donors are well known [28].

In order to test the assignment of the c-AFM observed current "patches" to P donor atoms, conduction AFM images were acquired on 3 samples with different doping concentration prepared as discussed in the methods section with nominal surface concentrations of [P] = 5x10^{14} cm^{-3}, 3x10^{17} cm^{-3}, and 5x10^{18} cm^{-3}, respectively. Each sample was cleaned and prepared identically. Conduction AFM measurements were then acquired under nominally identical conditions to those discussed above. The results of these experiments are shown in Fig. 5.2. They reveal that for the

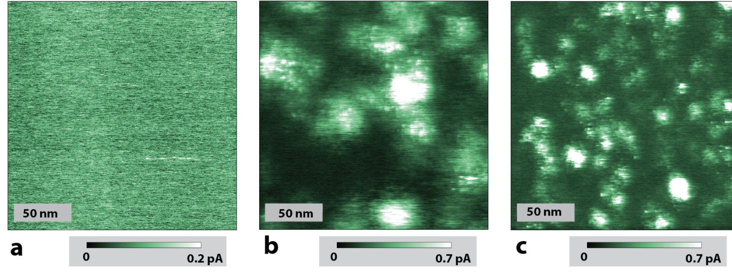

Figure 5.2. Conduction AFM images of c-Si samples with different P surface and bulk concentrations prepared by ion implantation. (a) [P] = 5x10^{14} cm^{-3}. No recognizable current maxima with significance above the noise level are observed. (b) [P] =3x10^{17} cm^{-3}. Current maxima with areal density of about 4x10^{10} patches/cm^{2} are observed. (c) [P] = 5x10^{18} cm^{-3}. Current maxima with a high areal density 2x10^{11} cm^{-2} are observed, compared to sample studied in (b). The observed densities of the patches fluctuate within a 12% range for different locations of the same sample, consistent with stochastic fluctuations expected from the given samples sizes.

two higher dopant density samples displayed in panels (b) and (c), the phosphorous concentrations of [P] = 3x10^{17} cm^{-3} and 5x10^{18} cm^{-3} correlate well with the increased concentration. The observed patch areal densities of the two more heavily doped samples are ≈4x10^{10} cm^{-2} and ≈2x10^{11} cm^{-2}, respectively, with a fluctuation of 12% between different images on the same samples. We attribute the absence of detectable current for the lowest P-concentration sample ([P] = 5x10^{14} cm^{-3}) to the lower P-donor density of this sample. This indicates that the density is too small to sustain an extended charge percolation path through the localized donor states to the back contact of the sample. Higher densities are required because all experiments were conducted significantly below the donor ionization temperature (≈30K) and in darkness where photo-charge carriers are absent. In essence, at a temperature T=4.3K, the weaker doped c-Si are essentially insulators and conduction AFM is therefore not possible.

We note that the apparent smaller patch size seen in Fig. 5.2 for [P] = 5x10^{18} cm^{-3} is caused by the small distances between the donor states that drop below natural patch sizes observed at low donor densities (with sizes discussed above). Under this high-[P] condition, the observed patch size will be governed by the donor distance, i.e., the measured patch radius is then given by the distance of the current minimum between the two neighbouring patch centers. In essence, the observed patch radius

will become half of the nearest neighbor distance.

In order to corroborate the findings presented above, the experiments were repeatedly conducted at different sample areas as well as for identically prepared silicon wafers with equal dopant concentrations. STM images in the region shown by Fig. 5.1(c), with a 10pA current set point and 2V DC tip-sample bias, are shown in Fig. 5.3 (d) to (f), together with a series of corresponding conduction AFM images in identical areas. Figure 5.3 (a) and (b) are the same images as shown in Fig. 5.1 (b), (e) respectively. Panels (b), (d), (e), and (f) of Fig. 5.3 display additional data sets. Panels (b), (c), (e), and (f) of Fig. 5.3 were recorded on the areas marked by the boxes in (a) and (b), which provide images with successively smaller scale for both the conduction AFM as well as the STM measurements. The data confirm again that there is no recognizable correlation between the STM topography map and the distribution of bright patches in the conduction AFM images (top row). The data also show that the observed surface is pristine (terraces are observed) and that an atomic scale structure of the conduction AFM current distribution exists which is indicative of either the influence of the crystalline silicon lattice or the presence of highly localized surface defects, e.g., silicon dangling bond states.

We repeated the experiments described by Fig. 5.3 and performed STM and conduction AFM experiments various times at various places of the given sample as well as different samples obtained from the same wafer. Figure 5.4 (a) and (d) are the conduction AFM and STM images already shown in Fig. 5.3 (b) and (e), respectively. These data sets are here compared with conduction AFM and STM images shown in and Fig. 5.4 (b), (c), (e), and (f) obtained on different samples at different measurement days that were nominally prepared under the same conditions and from the same silicon wafer. The images were acquired under nominally identical measurement conditions. The STM images (lower row) show that all three measurements reveal different surface point defect densities. While we did not further study the nature of these point defects as well as conditions which favor or suppress their generation, a comparison of the observed densities as well as their increase over time with data of previous UHV studies of c-Si (100)-(2x1) reconstructed surfaces suggests that these are due to water adsorbates [20]. We note that the point defects observed

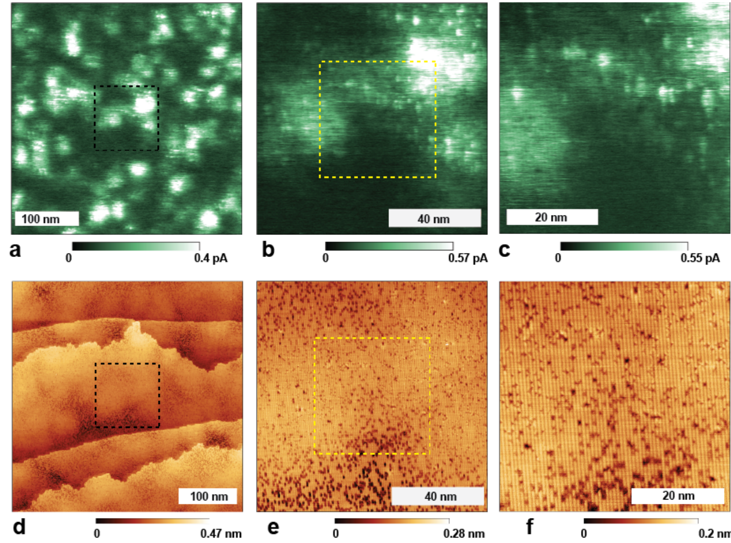

Figure 5.3. Comparison of conduction AFM and STM images of c-Si surface. (a) to (c): Conduction AFM images of c-Si surfaces acquired in darkness at 4.3K. Applied tip voltage is 1.3V for panels (a) to (c). (d) to (f): STM topography images acquired under illumination at 2V tip voltage, corresponding to the areas shown in (a) to (c), respectively. The broad (≈30nm) 'patches' seen in (a) to (c) do not correlate with the STM topography of the surfaces displayed in (d) to (f), respectively. (b), (c), (e), and (f) are the high–resolution images taken in the respective black and yellow box regions shown in (a), (b), (d) and (e), respectively.

here are of different nature than the silicon dangling bond states at Si/SiO2 interfaces discussed in detail in the main text because the areal densities of those silicon dangling bond states does not change with time under nominally identical UHV conditions. In contrast, the AFM conduction images (upper) reveal that the larger current patch sizes and spatial distribution are approximately the same. The AFM conduction images also reveal fine structures within these patches. The AFM and STM images show that the terrace steps in the reconstructed surface do not correlate with the location of the large patches. This is consistent with the hypothesis that the patches are caused by P donors.

5.4 Detection of surface dangling bond states

In order to investigate the nature of the patch fine structures, STM and c-AFM images were taken on (100) c-Si samples with concentrations of [P] $\approx 10^{17}\text{cm}^{-3}$ to 10^{18}cm^{-3} right after flash anneal took place (no oxide) and then again about a day

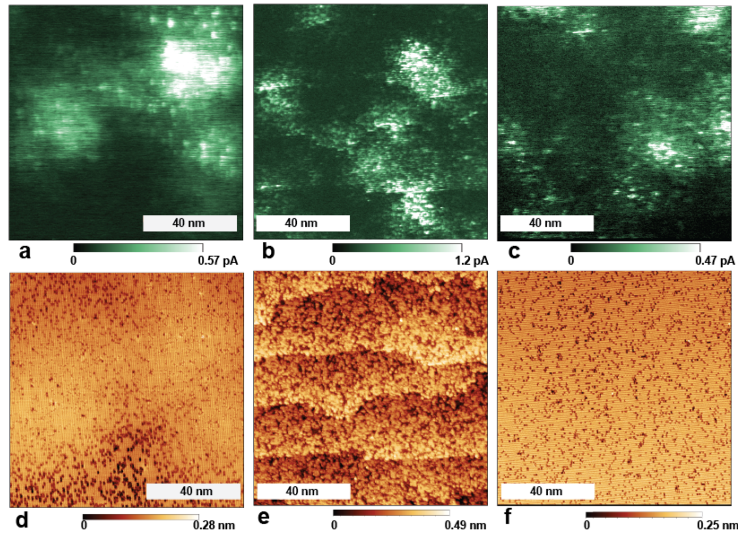

Figure 5.4. Comparison of 100x100nm conduction AFM and STM image combinations taken on different samples taken from the same wafer. All images were acquired on samples from the same wafer under nominally identical measurement conditions. The top row displays conduction AFM images; the bottom row displays STM images at locations corresponding to the respective images in the top row. The STM images reveal that all three surfaces have different atomic scale structure and display different surface point defect densities. This variation is due to the fact that the three samples were flash annealed separately. The locations of the large current patches do not correlate with the terrace steps observed in the STM images.

later after a native oxide had been formed. An STM image of the surface taken right after anneal is shown in Fig. 5.5(a). This data set was acquired at a temperature T = 4.3K, with sample illumination that provided free carrier conductivity to the back contact, and a 20pA current set point with a tip voltage of 2V. The image shows that the surface is fully reconstructed with some defects (dark spots). Figure 5.5(b) is a conduction AFM image taken in darkness at the same location. It is notable that directly after annealing, the conductance is typically high at the step-edges and other intrinsic morphological defects [dark spots in the STM image in (a)] of the surface. It is also notable that current percolation takes place predominantly through surface defects. Nevertheless, there are also many point defects at the surface [dark spots in the STM image in (a)] where current percolation is weak, proving that some surface defects allow for currents to propagate while others do not. In consideration of the general increase of current known to exist throughout the patch-like regions defined by

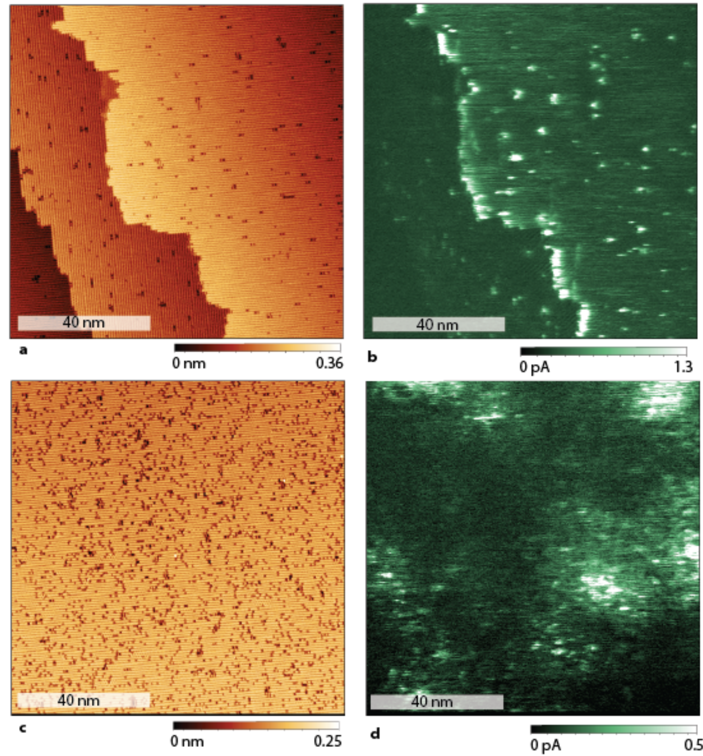

Figure 5.5. STM images and conduction AFM images of a surface of a P–doped c-Si crystal right after a flash anneal (a,b) and after one day (c,d). Initially, the surface has very few defects apart from step edges (a). After a day, the surface has more defects present (c). (b) A dark conduction AFM image taken at the same location and shortly after image (a). It shows that current maxima occur only at a few point-like defects which exist at the surface and at step edges. (c) After a day, a higher defect density has developed and now the P-donor patches appear in the conduction AFM image (d).

the presence of P donor states, the observation of surface defects with and without charge percolation strongly suggests that electric current requires the presence of both, a surface state as well as an underlying donor state. If a surface defect is not connected to a donor state underneath or if a donor state is close to the surface but not to a surface state, there will be no current percolation. We note that for the sample used for the measurements in Fig. 5.5(a) and (b), the overall defect density at the surface is so low that their correlation to patch-like structures attributed to the donor atom is not obvious in the conduction AFM images. In contrast, when these STM and c-AFM experiments are repeated a day later on the same sample, with the same tip, and under the same experimental conditions, the results (shown in panels (c) and

(d)) differ significantly. The STM measurement (c) now shows a reconstructed surface that has a much higher surface point defect density [20]. The conduction AFM image taken on the same area as the image in panel (c) shows that the conductivity patches attributed to phosphorus donor atoms have now appeared. As seen in both panels (c) and (d), the surface defects are randomly distributed across the surface, yet only those defects electrically connected to a nearby P donor state become visible. Thus, the data in Fig. 5.5 show that the small, highly localized states are responsible for the fine structure within the larger current patches, but also for the electrical access to donor atoms in c-Si substrate. Without these highly localized defects, tunneling from the tip to the donor atoms is unlikely. While silicon dangling bonds are expected to exist at homogeneous densities throughout the observed sample areas, current through the highly localized states is observed only when these states connect to an adjacent P donor, which in turn is connected to other P donors which form the percolation paths that provide the observed current. We therefore conclude that electrical current from P donor atoms to the cantilever tip requires the intermediate involvement of these highly localized interface defects.

This realization also corroborates that the above–discussed, fine-structured current patches observed with conduction AFM do not represent P donor wave functions; instead, they are indicative of surface defect clusters in close proximity of P donor states underneath the surface. Thus, while the size and the shape of these patches are likely correlated to the P donor wave–function, this correlation is convoluted with surface defect distributions. The charge percolation maps revealed by the data presented are strongly dependent on the probed electronic states and thus, the geometric nature of their wave–functions, but they are nevertheless not directly equitable to the three-dimensional projections of the wavefunctions of the involved states onto the observed two-dimensional data. We note again that the qualitative reproducibility of the experiments shown in Fig. 5.5 was shown repeatedly with various samples and scanning probes tips.

Next, the nature of the fine structure within the higher conductivity patches was investigated. In order to determine whether it is caused by silicon dbs, samples with similar P dopant densities but varying surface db densities were prepared through

growth of thin oxide layers. (See methods section for details.) Low-temperature grown (<500°C) silicon/ silicondioxide (Si/SiO2) interfaces can exhibit very high db densities (>10^{12} cm^{-2}) which include both crystalline silicon surface states (so-called Pb centers) as well as oxygen vacancy defects in the amorphous oxide layer (so-called E centers) [26, 4, 17]). The average separation between those states is therefore only a few nanometers (<10nm). Figure 5.6 displays the imaging results on such an oxidized surface (2-3 thickness [16]) under otherwise identical conditions as for the measurements described by Fig. 5.1. Panel (a) confirms that, similar to the image in Fig. 5.1(e), patch-like regions with FWHM of the order of 10nm to 15nm exist within which higher current densities are observed, while outside of these regions, the current is small. Also, similar to Fig. 5.1(e), Fig. 5.6(a) displays a distinct fine structure, yet in contrast to Fig. 5.1(e), the fine structure consists of well-separated, randomly distributed, highly localized current maxima. Fig. 5.6(b) and (c) display conduction AFM scans of sub-areas of (a) and (b), respectively, with increasing resolution. Note the data set in (b) is not a magnification of the data in (a) but from a separate measurement in the same sub-area. In order to determine the size of this local current maximum, we have determined its full width at half maximum (6Å) using a linecut taken from the data in (c), as indicated by the red dotted line and shown in Fig. 5.6(d). Note that the current variation in this localized region is approximately 200 fA.

The width of the localized current maximum seen in Fig. 5.6(c) and (d) is determined by either the effective tunneling radius of the probe tip or the actual size of the observed electronic state. Given that all features seen in Fig. 5.6(b) to (d) exhibit approximately the same localization, we conclude that it is due to the resolution limit set by the radius of the tip. This implies that the observed electronic states could be more localized than the widths seen in the image. We therefore believe that these states could be due to silicon dbs at the c-Si surface. Figure 5.6(a) shows that the highly localized current maxima are only detected within the much larger, tens of nm-sized, patch-like structures attributed above to P donors atoms. Between these patches, larger areas exist where no local current maxima are observed. This observation suggests that charge percolation for the observed data sets and under the given bias conditions, occurs preferably through pairs of P donors and the

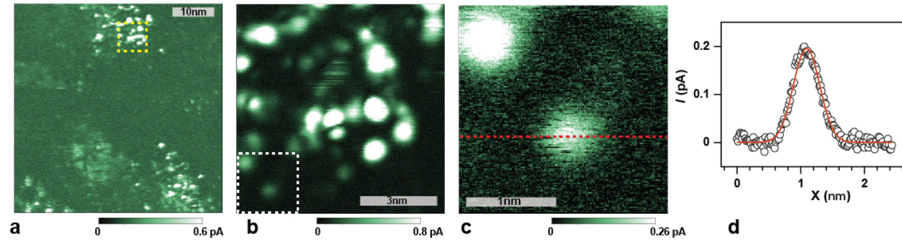

Figure 5.6. Conduction AFM image on a thin SiO_2 layer grown on top of a P–doped Si substrate. (a) Current map obtained from the P–doped c-Si substrate in darkness at 4.3K after a thin SiO_2 film was grown. Large (>20nm) patches surrounded by low-current regions still exist, yet the fine structure of these patches is significantly more isolated. Overall, the measured current densities are lower as seen in (b), which represents an current map with higher scanning resolution obtained on the subarea of (a) marked by the yellow square. (c) Imaged zoomed into the subarea marked by a white square in (b). (d) Plot of the current marked in (c) by the red line as a function of lateral position. The displayed individual current maximum has a full width at half maximum of about 6Å.

surface states (e.g., the db states) rather than directly from the probe tip to the phosphorus donors. For the applied positive tip bias, this is indeed consistent with the well-investigated spin-dependent P/db transitions [28, 22, 18, 14, 29].

Figure 5.7 displays data confirming the results shown in Fig. 5.6(b) through (d). Two sets of conduction AFM images were recorded at different locations under nominally identical conditions. As the experiments display in, i.e., Fig. 5.6(b), localized conduction is observed on a native oxide at 4.3K without light illumination. Figures 5.7(a) and (d) clearly confirm the occurrence of highly localized current maxima which appear in larger, nm-range patch-like structures attributed to the P donor atoms. In contrast to the samples without native oxide, the density of localized maxima within the patches on the oxidized sample is significantly less dense than those observed on the bare silicon surface. The localized maxima indicate electronic states which are electronically coupled to a nearby P atom. We attribute the brightness (current) variations of these point-like states to different transition rates between these states and the P atoms and thus, to their physical distance to a nearby P donor state.

Panels (b) and (e) of Fig. 5.7 are high-resolution images acquired at locations marked by yellow boxes in panels (a) and (d), respectively. Both panels (b) and

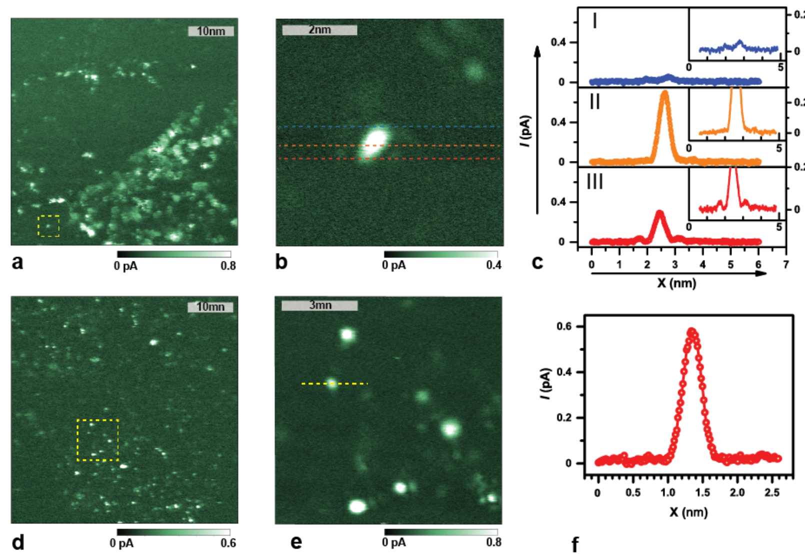

Figure 5.7. Conduction AFM images of P–doped ([P]≈10^{17}cm^{-3} to 10^{18}cm^{-3}) c-Si surfaces with thin native oxide layers at 4.3K without light illumination. Panels (a) to (c) and (d) to (f) represent data sets collected at two different locations. Panel (a) and (d) both contain areas where patch-like clusters of local current maxima are observed while other areas show few localized current maxima. The local current maxima are due to highly localized electronic states in the oxide or at the c-Si oxide interface which are in electronic contact with nearby phosphorus atoms. They are attributed to silicon dangling bond states. Panels (b) and (e) are high–resolution images taken from samples areas indicated by the yellow squares in panels (a) and (d), respectively. Panels (c) and (f) display line profiles of the local current maxima taken in the regions highlighted by the lines in panels (b) and (e), respectively. The widths of these local current maxima are indicative for the strong localization of dangling bond states.

(e) resolve individual current maxima of different shape and size. Similar to Fig. 5.1(d), panels (c) and (f) of Fig. 5.7 show one–dimensional line profiles which were recorded at these positions indicated by the lines in panel (b) and (e). The observed localization of these defects varies from 3–5Å.

The very small localization and the discreteness of the fine structure observed within the P induced current patches is consistent with highly localized dangling bond [23, 14] states at the surface of the c-Si crystal or within the thin silicon dioxide network. The clustering of these highly localized electronic states within the patches is indicative that these states are connected electronically to a phosphorus donor state. Thus, while silicon dangling bonds likely exist at homogeneous densities throughout the observed sample areas, electric current is observed only through the

highly localized surface states when they are connected to an adjacent P donor. As the P donor in closest proximity of the surface states is then connected to other P donors deeper in the bulk, the percolation paths that allow the observed currents are formed.

5.4.1 The current-voltage characteristics of P-db pairs

In order to corroborate the findings presented above and in particular the hypothesis that the charge percolation for the observed conduction AFM images is caused by P-db transitions, we have repeated the imaging and identified hundreds of locations with highly localized current maxima (a few more images are displayed in the supporting information). At each of these states, the conductive probe was positioned at the location of current maximum and the current was monitored while the probe Fermi-level was lowered through an increase of the probe bias voltage. Examples for the current-voltage (I-V) characteristics obtained at different tip positions, resulting from this procedure, are shown in Fig. 5.8(a) to (d). Some of these I-V curves exhibit one (a) or two (d) distinct plateaus on which the current is only weakly bias dependent while others display a bias dependence similar to a macroscopic diode (b) [6, 19] or a plateau with negative slope (c). All of the more than 800 I-V curves fall qualitatively within one of these four groups.

Figure 5.8(e) displays the numbers of curves with I-V characteristics of each of the four different cases shown in Fig. 5.8(a) to (d). 334 I-V curves show Schottky diode-like characteristics and 273 I-V curves show a single flat plateau. Given the random localization and energies of Si/SiO_2 interface states (see Fig. 5.8(f)), many hypotheses explaining the four observed I-V curves can be invoked. For instance, the rare double plateau characteristics could be caused by multiple localized defects being in proximity of the charge percolation path. The single-plateau function could be accounted for transitions between the P donor and silicon surface dangling bonds (so-called P_b states). The band diagram illustrating the P/Pb transitions, as developed from electrically detected magnetic resonance spectroscopy [28, 12, 22, 13], is shown in Fig. 5.8(f). According to this model, the plateau occurs when the Fermi level Ef of the probe is between the energy of the doubly occupied, negatively charged Pb- state

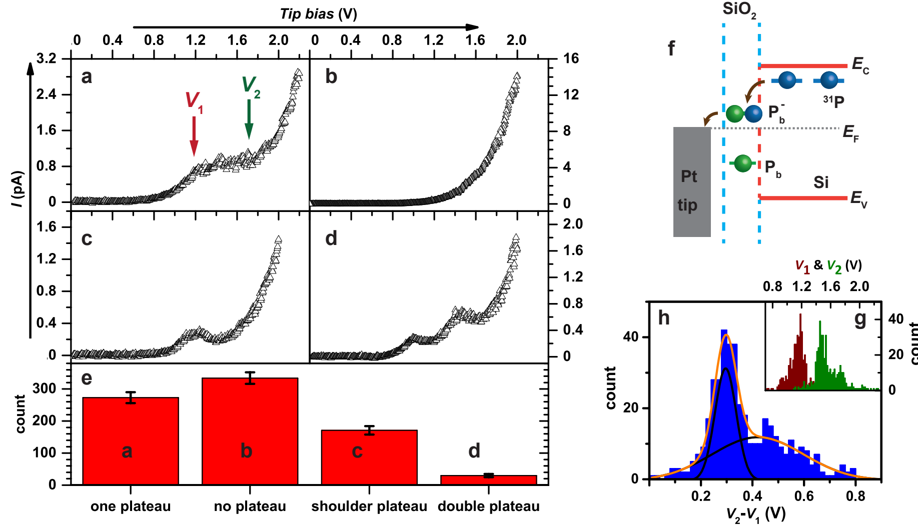

Figure 5.8. Different types of I-V curves and their distribution. (a) to (d) display samples of four qualitatively different types of I-V curves of more than 800 measured different I-V curves acquired on SiO_2 covered Si(100) surfaces. (a) I-V curve with a single flat plateau region; (b) I-V curve without plateau as expected from a macroscopic silicon to platinum Schottky diode; (c) I-V curve with tilted plateau which consists of a local maximum followed by a local minimum; (d) I-V curve with double plateau. (e) Bar diagrams indicating the actual number of qualitatively distinct I-V curves shown in (a) to (d) based on the acquired data. The error bars represent the square root of the actual number. (f) Energy diagram of the doped silicon sample and tip including donor state and the interface dangling bond state (Pb center). (g) Histograms of the plateau-onset (brown) and -end (green) voltages of the 415 plateaus from data sets of I-V curves that display a single flat plateau similar to the data seen in (b). (h) Histogram (blue data) displaying the plateau widths of the given data sets (difference between plateau-onset and end voltage of each curve) as well as the fit (orange line) with a two Gaussian functions (black lines). The good agreement indicates that there are at least two qualitatively different types of highly localized interface states responsible for the local current maxima at the surface. The two Gaussian functions are centered at 300(5) mV and 420(19) mV.

and the single occupied neutral P_b state. Little charge transfer will occur at low bias when the E_f is above the Pb- level because direct tunneling from P donors into the tip is not likely. In contrast, when E_f drops below singly occupied Pb ground state at high bias, an increasing current passes through the states. A similar hypothesis that are also based on existing P/Pb recombination models [28, 12, 22, 13] can be invoked in order to explain the single plateau I-V-behavior with negative slope seen in Fig. 5.8(c) where quantitative differences between the individual transitions for flat plateau IV functions and negatively sloped I-V functions can account for the

qualitatively different behavior.

5.5 Reproducibility and uniqueness of I-V curves

While current-voltage (I-V) curves measured with conduction AFM at different sample locations and conditions fall into four characteristic groups as discussed in the main text, all conduction AFM experiments have shown excellent reproducibility of I-V curves when measurements were repeated at identical sample locations and nominal experimental conditions. In order to demonstrate this reproducibility, repeated experiment were conducted at local current maxima. Figure 5.9 displays the results for repeated I-V curves conducted at two different locations. For each of these locations, only very small differences between each of the measured I-V curves were observed. We attribute the small differences that are observed to the finite thermal drift of the cantilever probe as it moves slowly away from the selected defect state. Defect-1 and defect-2 represent two independent current maxima at different locations pertaining to examples if I-V functions represented by the qualitatively similar data in Fig. 5.8(c) and (a), respectively. Each experiment was repeated seven times.

Since dangling bond states exist at the interface between the c-Si and silicon dioxide as well as within the silicon dioxide, they are all unique due to the randomness of their individual microscopic environment (the continuous random network of the amorphous silicon dioxide). This is the reason that one would expect to see equally random variations in the I-V curves obtained on different dangling bond states. This is further supported by the fit of the distribution of measured energies of the dangling bond states with published data, as shown in Fig. 5.8(h).

Figure 5.10 displays an array of I-V curves recorded with the conduction AFM in darkness and at T = 4.3K at various arbitrary positions across an oxidized c-Si surface. The displayed data sets represent a very small subset of all measured I-V curves which are additional examples for the four qualitatively different I-V curves that have been observed. Each row in the array of Fig. 5.10 displays several qualitatively identical examples. The first row shows single flat plateau I-V curves, the second row shows single-plateau I-V curves with negative slope, the third row displays monotonous diode-like I-V curves , and in the fourth row another single double-plateau I-V curve is

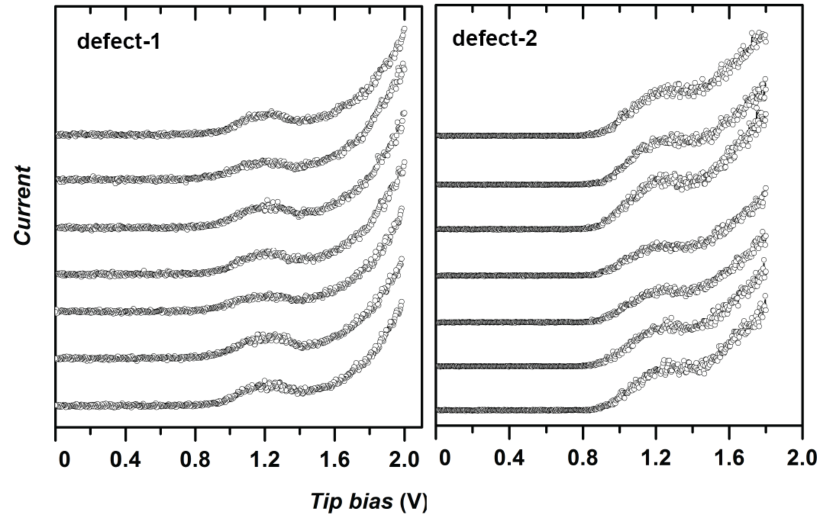

Figure 5.9. Repetition of current-voltage (I-V) measurements using conduction AFM for two randomly chosen surface locations 'Defect-1' and 'Defect-2'. While the two locations display different I-V characteristics, they display very reproducible characteristics for each location. Each curve has identical vertical axes. Since the curves are offset along the vertical axis, no vertical axis level is printed in the plot.

presented. Comparing the data sets within each row shows that within each category, there are still significant quantitative differences. For instance, for the single flat plateau curves displayed in the top row of Fig. 5.10, the onset and endpoints as well as the width of the plateaus are different for each data set. Similarly, the magnitudes of currents vary from a few hundreds of fA to a few pA. Comparing the second row data sets (single plateau curves with negative slope at the plateau), each plateau occurs at different current magnitude and the slope of each plateau differs from each other. Also, the curves in the third row qualitatively look like diodes but both the magnitude of current and the turn on voltage different from each other. The last row displays a double plateau curve. These were observed only 30 times among the more than 800 measured I-V curves.

5.6 Discussion and conclusions

We have quantitatively scrutinized the attribution of the single-flat-plateau I-V characteristics to conduction through P/P_b pairs by examining the widths of the current plateaus for flat plateaus as represented by the I-V function displayed in Fig. 5(a). Literature reports of Pb centers at (100) surfaces indicate that the Coulomb repulsion

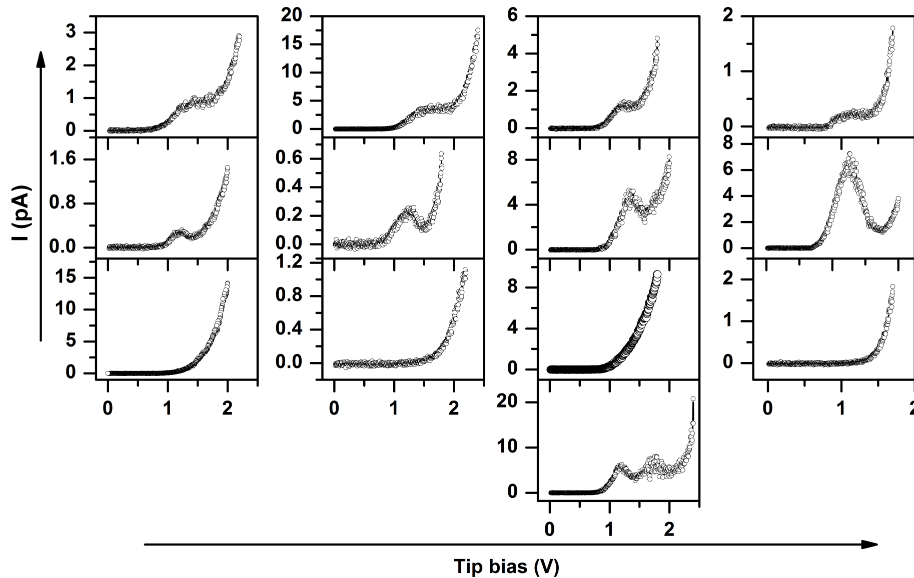

Figure 5.10. Plots of I-V curves measured under nominally identical conditions at various locations of one sample. Each column of the figure represents four measurements performed at locations within a proximity of a few hundred micrometers. While all measured I-V functions are quantitatively different, measurements conducted at each location could be categorized into four qualitatively different sets of curves as discussed in the main text. The double plateau curve shown in the fourth row has been consistently rare ($< 4\%$ of all measurements).

induced correlation energies responsible for the splitting of the singly occupied, neutral Pb state and the doubly occupied negatively charged Pb- state are different for two different types of Pb centers, the P_{b0} as well as the P_{b1} [9, 26]. Moreover, due to the inherent disorder of the amorphous silicon dioxide layer in the direct environment of P_b centers, correlation energies are strongly distributed [9, 26, 3]. Thus, if the single-plateau I-V curves are due to P/P_b transitions, the plateau-width distribution must reveal both the presence of two distinct defect types as well as their respective average values. Figure 5(g) (inset) displays a histogram of the plateau-onset and -end bias voltages obtained from the 415 I-V curves observed with single flat plateaus, sorted in 0.02V bins. The difference between the plateau offset and end voltage for each curve as obtained from the data in Fig. 5(g) is displayed in the histogram of Fig. 5(h), also with 0.02V bin size. For the limited number of available counts, the data reveal an excellent agreement with a double Gaussian fit function, represented by the orange data line. The good agreement with a bimodal distribution supports

the expected presence of two types of states. The Gaussian distributions position are centered at 300(5) mV and 420(19) mV, in good agreement with capacitance-voltage spectroscopy results of the Si(100)/SiO2 interface which shows two types electronic states [26, 3] with electron correlation energy of 350meV and 550meV. Thus, we therefore attribute the locations where current maxima reveal I-V curves with single, flat plateaus to the presence of highly localized P_{b0} or P_{b1} dangling bonds in proximity of a P donor atom.

In conclusion, the application of low-temperature, high-resolution current imaging under dark conditions to surfaces of strongly P–doped c-Si with thin oxide surfaces has allowed us to image charge conduction through individual pairs of P donor and highly localized surface silicon dangling bond (P_{b0} and P_{b1}) states, as verified by spatially resolved imaging and energetic considerations. Hence, a method to electrically contact individual pairs of P donor and Pb interface states on an atomic length scale is demonstrated, which could serve as a selective address- and readout-technique for individual P donor qubits in c-Si.

5.7 References

[1] G. Binnig, H. Rohrer, Ch. Gerber, and E. Weibel. 7x7 reconstruction on Si(111) resolved in real space. *Phys. Rev. Lett.*, 50:120, 1983.

[2] G. W. Brown, H. Grube, and M. E. Hawley. Observation of buried phosphorus dopants near clean Si(100)-(2×1) surfaces with scanning tunneling microscopy. *Phys. Rev. B*, 70:121301, 2004.

[3] J. P. Campbell and P. M. Lenahan. Density of states of P_{b1} Si/SiO_2 interface trap centers. *Appl. Phys. Lett.*, 80:1945, 2002.

[4] W. E. Carlos. Paramagnetic centers at Si-SiO_2 interfaces in silicon-on-insulator films. *Appl. Phys. Lett.*, 50:1450, 1987.

[5] C. J. Chen. *Introduction to Scanning Tunneling Microscopy.* New York, Oxford., 1993.

[6] S. S. Cohen, D. H. Bower, D. M. Brown, and J. F. Norton. Platinum silicide contacts to silicon by lift-off. *J. Appl. Phys.*, 55:4294, 1984.

[7] J. P. Dehollain, J. T. Muhonen, K. Y. Tan, A. Saraiva, D. N. Jamieson, A. S. Dzurak, and A. Morello. Single-shot readout and relaxation of singlet and triplet states in exchange-coupled ^{31}P electron spins in silicon. *Phys. Rev. Lett.*, 112:236801, 2014.

[8] P. Fiorenza, W. Polspoel, and W. Vandervorst. Conductive atomic force microscopy studies of thin SiO_2 layer degradation. *Appl. Phys. Lett.*, 88:222104, 2006.

[9] G. J. Gerardi, E. H. Poindexter, P. J. Caplan, and N. M. Johnson. Interface traps and P_b centers in oxidized (100) silicon wafers. *Appl. Phys. Lett.*, 49:348, 1986.

[10] F. J. Giessibl. High-speed force sensor for force microscopy and profilometry utilizing a quartz tuning fork. *Appl. Phys. Lett.*, 73:3956, 1998.

[11] R. C. Henderson, R. B. Marcus, and W. J. Polito. Carbide contamination of silicon surfaces. *J. Appl. Phys.*, 42:1208, 1971.

[12] F. Hoehne, L. Dreher, M. Suckert, D. P. Franke, M. Stutzmann, and M. S. Brandt. Time constants of spin-dependent recombination processes. *Phys. Rev. B*, 88:155301, 2013.

[13] F. Hoehne, H. Huebl, B. Galler, M. Stutzmann, and M. S. Brandt. Spin-dependent recombination between phosphorus donors in silicon and Si/SiO_2 interface states investigated with pulsed electrically detected electron double resonance. *Phys. Rev. Lett.*, 104:046402, 2010.

[14] F. Hoehne, J. Lu, A. R. Stegner, M. Stutzmann, M. S. Brandt, M. Rohrmüller, W. G. Schmidt, and U. Gerstmann. Electrically detected electron-spin-echo envelope modulation: a highly sensitive technique for resolving complex interface structures. *Phys. Rev. Lett.*, 106:196101, 2011.

[15] B. E. Kane. A silicon-based nuclear spin quantum computer. *Nature*, 393:133, 1998.

[16] M. Morita, T. Ohmi, E. Hasegawa, M. Kawakami and M. Ohwada. Growth of native oxide on a silicon surface. *J. Appl. Phys*, 68:1272, 1990.

[17] P. M. Lenahan and J. F. Conley. What can electron paramagnetic resonance tell us about the Si/SiO_2 system. *J. Vac. Sci. Technol. B*, 16:2134, 1998.

[18] H. Morishita, L. S. Vlasenko, H. Tanaka, K. Semba, K. Sawano, Y. Shiraki, M. Eto, and K. M. Itoh. Electrical detection and magnetic-field control of spin states in phosphorus-doped silicon. *Phys. Rev. B*, 80:205206, 2009.

[19] H. Muta. Electrical properties of platinum-silicon contact annealed in an H_2 ambient. *Jpn. J. Appl. Phys.*, 17:1089, 1978.

[20] M. Nishizawa, T. Yasuda, S. Yamasaki, K. Miki, M. Shinohara, N. Kamakura, Y. Kimura, and M. Niwano. Origin of type-c defects on the $\mathrm{Si}(100) - (2 \times 1)$ surface. *Phys. Rev. B*, 65:161302, 2002.

[21] H. Over, J. Wasserfall, W. Ranke, C. Ambiatello, R. Sawitzki, D. Wolf, and W. Moritz. Surface atomic geometry of Si(001)-(2x1): A low-energy electron-diffraction structure analysis. *Phys. Rev. B*, 55:4731, 1997.

[22] S.-Y. Paik, S.-Y. Lee, D. R. McCamey, and C. Boehme. Electrically detected crystal orientation dependent spin-rabi beat oscillation of c-Si (111)/SiO_2 interface states. *Phys. Rev. B*, 84:235305, 2011.

[23] J. L. Pitters, L. Livadaru, M. B. Haider, and R. A. Wolkow. Tunnel coupled dangling bond structures on hydrogen terminated silicon surfaces. *J. Chem. Phys.*, 134:064712, 2011.

[24] J. J. Pla, F. A. Mohiyaddin, K. Y. Tan, J. P. Dehollain, R. Rahman, G. Klimeck, D. N. Jamieson, A. S. Dzurak, and A. Morello. Coherent control of a single ^{29}Si nuclear spin qubit. *Phys. Rev. Lett.*, 113:246801, 2014.

[25] J. J. Pla, K. Y. Tan, J. P. Dehollain, W. H. Lim, J. J. L. Morton, D. N. Jamieson, A. S. Dzurak, and A. Morello. A single-atom electron spin qubit in silicon. *Nature*, 489:541, 2012.

[26] E. H. Poindexter, G. J. Gerardi, M. E. Rueckel, P. J. Caplan, N. M. Johnson, and D. K. Biegelsen. Electronic traps and P_b centers at the Si/SiO_2 interface: Band gap energy distribution. *J. Appl. Phys.*, 56:2844, 1984.

[27] K. Saeedi, S. Simmons, J. Z. Salvail, P. Dluhy, H. Riemann, N. V. Abrosimov, P. Becker, H.-J. Pohl, J. J. L. Morton, and M. L. W. Thewalt. Room-temperature quantum bit storage exceeding 39 minutes using ionized donors in silicon-28. *Science*, 342:830, 2013.

[28] A. R. Stegner, C. Boehme, H. Huebl, M. Stutzmann, K. Lips, and M. S. Brandt. Electrical detection of coherent ^{31}P spin quantum states. *Nat. Phys.*, 2:835, 2006.

[29] M. Suckert. Electrically detected double electron − electron resonance: exchange interaction of P donors and P defects at the Si/SiO$_2$ interface. *Mol. Phys.*, 111:2690, 2013.

[30] S. Uemura, M. Fuji, H. Hashimoto, and N. Nagai. In situ observation of native oxide growth on a Si(100) surface using grazing incidence X − Ray reflectivity and fourier transform infrared spectrometer. *Jpn. J. Appl. Phys.*, 40:5312, 2001.

[31] M. Veldhorst, J. C. C. Hwang, C. H. Yang, A. W. Leenstra, B. de Ronde, J. P. Dehollain, et al. An addressable quantum dot qubit with fault-tolerant control-fidelity. *Nat. Nano.*, 9:981, 2014.

[32] C. J. Wellard and L. C. L. Hollenberg. Donor electron wave functions for phosphorus in silicon: Beyond effective-mass theory. *Phys. Rev. B*, 72:085202, 2005.

[33] L. Zhang, T. Sakai, N. Sakuma, T. Ono, and K. Nakayama. Nanostructural conductivity and surface-potential study of low-field-emission carbon films with conductive scanning probe microscopy. *Appl. Phys. Lett.*, 75:3527, 1999.

[34] N. Zheng, C. C. Williams, E. G. Mishchenko, and E. Bussmann. A three-dimensional model of single-electron tunneling between a conductive probe and a localized electronic state in a dielectric. *J. Appl. Phys.*, 101:093702, 2007.

CHAPTER 6

BARRIER WIDTH DEPENDENCE OF INDIVIDUALLY OBSERVED SINGLE ELECTRON TUNNELING EVENTS

With the ability to locate individual silicon dangling bonds at an oxidized silicon surface that was demonstrated in the previous chapter, one can now attempt to identify a tunneling random telegraph signal (RTS) using the spin–microscope setup. This chapter is therefore focused on the measurement of the tunneling dynamics of single electrons from a Fermi reservoir to a localized electron state (a silicon dangling bond). For this, the scanning–probe based on a quartz tuning–fork and a Pt tip is applied to a silicondioxde surface. When the tip–Fermi energy is aligned to a localized defect state, tunneling of individual electrons between surface and tip occurs, causing cantilever–detected electrostatic forces to display RTS. Tunneling versus height experiments reveal the barrier–width dependence of the tunneling dynamics and may be utilizable for spin–dependent tunneling based single–spin detection. This research was conducted in collaboration with C. C. Williams and C. Boehme and it has been submitted for publication.

6.1 Introduction

Quantum tunneling, the process that allows objects to pass barriers which are too high for classical motion, is one of the aspects of quantum mechanics that have set this theory so starkly apart from our macroscopic perception of nature. Because of this, tunneling effects have been among the most rigorously tested phenomena since they were first understood in the context of radioactive decay during the late 1920s [7]. Since then, the relevance of tunneling for a broad range of phenomena beyond high energy physics has been explored ranging from many condensed matter physics effects [16, 6, 22] to quantum biology, e.g., in the context of DNA muta-

tion [14]. The quantitative understanding of tunneling has become important for technological applications in electronic [6, 22] and superconducting [11] devices, but also for microscopy, most of all scanning tunneling microscopy (STM) [1, 21]. In spite of these successes, there are still comparatively few examples in the literature where individual tunneling processes are studied between single quantum mechanical states with good control of the parameters governing these processes. While, for instance, individual tunneling of a nuclear fragment (one or several clustered nucleons) can be observed straightforwardly when a radioactive decay occurs, little influence can be imposed on the potential well and the barrier from which these transitions occur. For electrons, tunneling through localized electronic states (e.g., defects in solids [20] or quantum dots [9, 25]) can be observed by current measurement and controlled by tunable barrier heights [23] through application of appropriate electrostatic potentials; however, for these experiments, it is still difficult to control barrier widths as spatial manipulation of electronic states poses a much greater challenge. In contrast, STM does allow us to tune the width of the vacuum gap between a Fermi reservoir in a scanning probe tip very accurately relative to individual electronic states at or below a surface or a molecule. However, while STM has the spatial resolution needed for the observation of tunneling through individual electronic states, it inherently relies on the detection of large electron ensembles (currents) through a conductive substrate. It does therefore not directly allow for the observation of individual electronic transitions.

In the following, we report on the time–dependent study of individual electron–tunneling transitions between a Fermi reservoir of a Pt tip and a single localized electron state in an insulating environment. The experiment is conducted as a force–detected single electron STM experiment, based on the previously reported single electron tunneling force spectroscopy [3, 5, 4, 26] (SETFS). Here, we present the study of the dynamics of random tunneling events by statistical analysis of the transiently recorded random telegraph noise (RTN) of a scanning probe frequency detected electrostatic force changes due to tunneling induced localization changes of individual electrons. The motivation of this study to meet the prerequisite of a previously described single–spin detection scheme based spin–selection rule controlled

tunneling [17], which is the verification of dynamically well-controlled RTN due to tunneling into a single silicon dioxide surface state.

6.2 Theoretical prediction of the cantilever frequency shift due to a single elementary charge transition

The scanning probe setup used in this study is a commercial instrument provided by Omicron Nanotechnology. For dark operation, a so–called Q–plus force sensor was employed onto which a metallic cantilever (Pt) was glued. The sharp Pt cantilever, used in this experiment as a Fermi reservoir, had a tip radius of about 10nm to 15nm. It was made from solid Pt wire and glued to the Q-plus tuning fork using conductive epoxy glue. The solid Pt tip was supplied by Rocky Mountain Nanotechnology, LLC [19]. The experimental setup, illustrated in Fig. 6.1(a), avoid the need for optical detection and the excitation of electron states that are probed or states in their environment (which can cause electrostatic fluctuations), a prerequisite for the systematic study of single electron transitions. Furthermore, due to variability of the temperature down to liquid ^{4}He temperature, the setup allows for the control of phonon activated processes, including thermal excitation of electronic states. The utilization of the Q-plus sensor allows cantilever oscillation–detected electrostatic force measurements at smaller oscillation amplitude ($\approx$ 1nm) and frequency ($f_0 \approx$ 30kHz, about an order to magnitude below typical beam–deflected silicon cantilevers), increasing the overall localization time of the cantilever tip in the proximity of the sample surface and associated force gradient, as desired when force detection and tip–to–surface tunneling are to take place simultaneously. In light of these advantages of the Q-plus sensor approach, it is noted that both the lower resonance frequency as well as the higher spring constant of the sensor (k = 1200Nm^{-1}) cause the disadvantage of a comparatively smaller electrostatic charge–induced cantilever resonance–frequency shift $\Delta f = -\frac{f_0}{2k} F'_{\text{eff}}$ [15, 2], with F'_{eff} being the effective force gradient between the tip and the sample.

We have calculated the frequency shift due to single–electron tunneling between the sample surface and the cantilever based on the given experimental parameters following the model by Bussmann et al. [3] and Wang et al. [24]. This one–dimensional

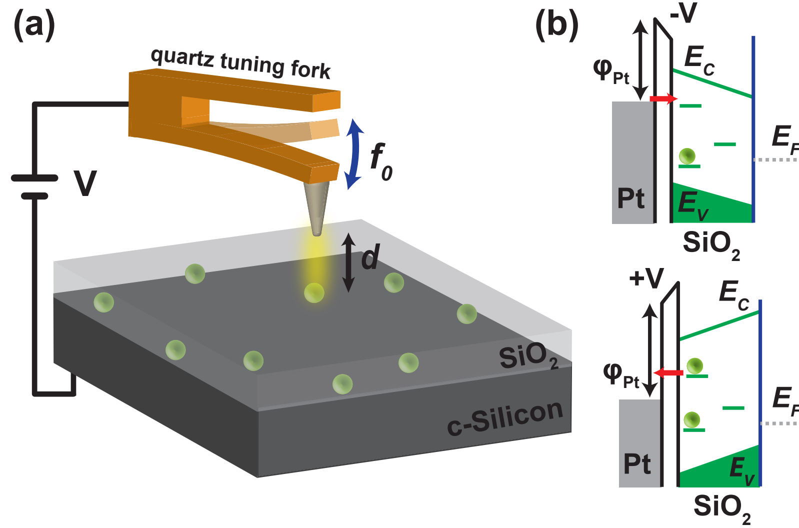

Figure 6.1. Illustration of the experimental setup. (a) The force sensor based on a quartz tuning fork oscillator with sharp Pt probe is oscillating at resonant frequency (f_0=30kHz) at a fixed oscillation amplitude of ≈1 nm. The sample surface consists of 10nm thick SiO_2 film grown on a highly doped crystalline (100) silicon wafer. A DC voltage source was connected between probe and substrate to control the tip bias. Tunneling took place between localized electronic states in the SiO_2 layer (indicated by green spheres). (b) Band diagram of the experiment at positive and negative applied bias. At negative bias, the Fermi energy of the Pt probe is above the energy level of the localized state and an electron can tunnel into the empty state (orange arrow). At positive bias, the Fermi energy of the tip is below the localized energy level and the electron tunnels out (orange arrow).

model is based on the assumption that tunneling occurs between a one–dimensional state and the tip surface, which together form a capacitor configuration. The electrostatic force induced cantilever frequency shift

$$\Delta f = -\frac{f_0}{2k} F'_{\text{eff}} \tag{6.1}$$

is calculated following Morita et al. [2] with

$$F'_{\text{eff}} = \frac{\epsilon_0 A V^2}{(z_m + \frac{t}{\epsilon})^{\frac{3}{2}} (z_m + 2a + \frac{t}{\epsilon})^{\frac{3}{2}}} \tag{6.2}$$

while A is the effective capacitor area (as defined by an effective tip radius of 12nm), V is the applied voltage, t is the thickness of the SiO_2 layer (about 10mn), a is the amplitude of the cantilever oscillation, and z_m is the probe–to–sample gap minimum during the cantilever oscillation cycle. Using these experimental parameters, a cantilever resonance frequency shift of Δf = 0.9Hz was predicted for the experiment

represented by Fig. 6.2, in which an electronic state was located 0.2nm underneath the sample surface.

6.3 Experiment

Experimentally, we build on the previous demonstration that SETFS can access individual electronic states with sub–nanometer spatial resolution with standard laser light beam–deflection AFM[3, 5, 4]. In contrast to these experiments, we are reporting here SETFS experiments on a low–temperature, scanning probe setup with an electrical quartz–tuning fork sensor that allows for force detected scanning probe experiments in complete darkness, to avoid electrostatic fluctuations, and with small oscillation amplitude ($\approx$ 1nm) as needed for experiments where tunneling and force detection take place simultaneously. All experiments were performed at a temperature of T = 77K on a thin 10nm SiO_2 film grown thermally at 1000°C in dry oxygen on top of a highly phosphorous doped, conductive silicon wafer which served as capacitor plate needed for the application of electric fields.

In order to find suitable surface states for the tunneling experiments, the probe was slowly brought into and out of proximity of the surface while the cantilever resonance frequency was monitored. This procedure was repeated at 1473 locations with both positive and negative biases applied between probe and sample. When the probe was within spatial and energetic tunneling range of a localized electronic state, the electrons could undergo an abrupt tunnel transition either from or to the tip as illustrated in Fig. 6.1(b). When tunneling occurs, the local electrostatic force gradient and thus, the cantilever resonance frequency, were modified. This resonance frequency change Δf was then detected by a phase–locked loop (PLL) circuit. As shown in Fig. 6.1(b), the sign and magnitude of the tip bias with respect to the substrate determine the Fermi level of the reservoir relative to the band levels of the substrate, with increasing biases causing the Fermi level to drop. While Fermi energies above (below) the localized state in tunneling range would always keep the state occupied (empty), an alignment of both levels within the range of thermal energies would allow for continuous tunneling into and out of the localized state. Since each transition constituted a charging or discharging event, the cantilever frequency shift

would exhibit RTN behavior.

6.4 Single electron tunneling force spectroscopy/microscopy

In order to find a combination of the tip bias V and the tip–to–surface distance d where tunneling can occur, we first adjusted the bias V to a constant, usually negative level before we measured the frequency shift $\Delta f(d)$ as a function of d at each new lateral tip position. Figure 6.2(a) displays $\Delta f(d)$ for $V = -4$V for the position on which the data presented in the following was measured. Note that contact between the tip and the SiO_2 surface ($d = 0$) is defined where $\Delta f(d)$ reaches an absolute minimum. For the measurement of the data in Fig. 6.2(a), the probe was slowly brought closer to the substrate. The data show that with decreasing d, a monotonous decrease of Δf occurs due to the increasing electrostatic force gradient between the charges in the tip and the surface which form a biased capacitor. At $d \approx 8.5$Å , a significant (larger than the Δf noise) departure of Δf from this monotonous behavior is observed. Upon further decline of d, the monotonous decrease is resumed. Note that the non-monotonous change of $\Delta f(d)$ introduced a frequency shift offset of about 0.9Hz when $d < 8.5$Å which is similar to that observed by Klein et al. [12] and Bussmann et al. [3]. The blue vertical bar in Fig. 6.2(a) represents the result of a theoretical calculation of Δf expected for a single elementary charge transition based on the one–dimensional tunneling model described by Bussmann et al. [3, 2] under utilization of experimental parameters given for the experiments described here. Given the agreement of these results with the observed frequency shift offset, we conclude that the data displayed in Fig. 6.2(a) are caused by electron transitions from the cantilever into an single electronic surface state. Note that while the data in Fig. 6.2(a) are indicative of a single electronic state, they are not due to individual tunneling transitions. Since the cantilever height was lowered adiabatically during this measurement, it is expected that within the gap range where the tip Fermi level and the electron state align energetically, tunneling can occur multiple times. We attribute the gradual shift of the offset of $\Delta f(d)$ between d=8.5Å and $d = 8.2$Å to this effect.

As shown in Fig. 6.2 (b) and (c), the frequency shift as a function of the applied

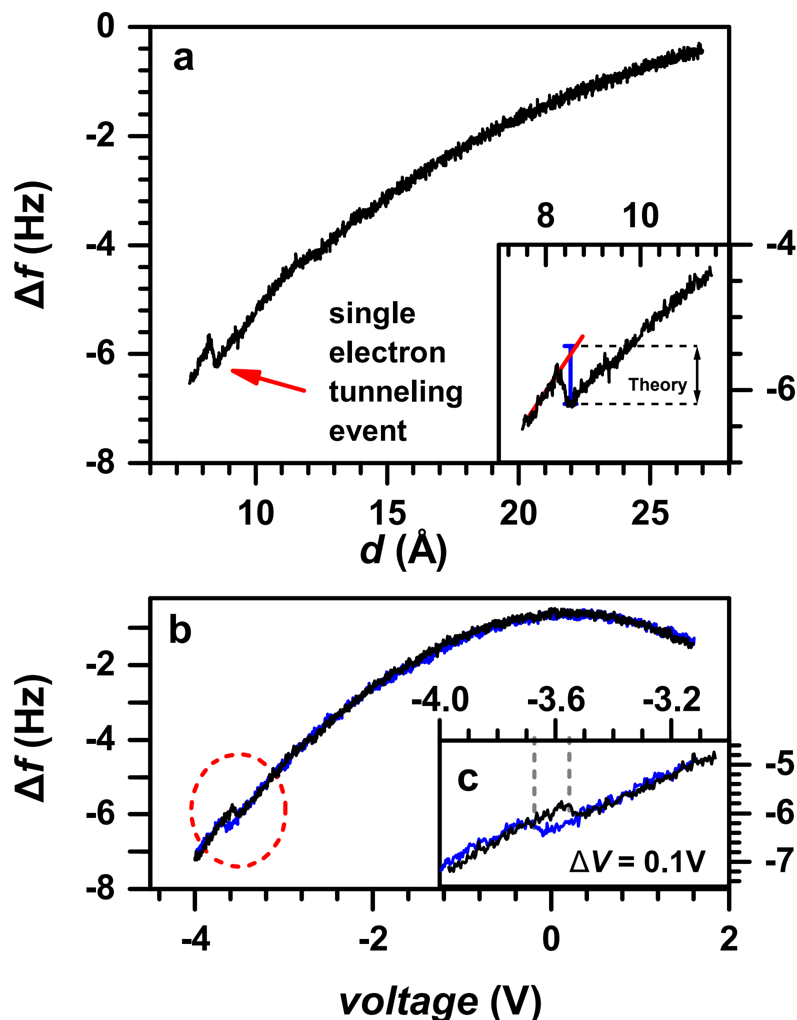

Figure 6.2. Cantilever frequency shift curve as a function of tip-to-surface gap and bias voltage. (a) Plot of measured cantilever frequency shift $\Delta f(d)$ as a function of the cantilever tip–to–surface distance d for decreasing d (the probe moved towards the surface) with bias $V = -4$V applied between tip and the sample. A single electron tunneling event is observed when an offest of the frequency shift appears due to the electrostatic force change caused by the single electron transition. The blue bar represents the calculated offset to Δf based on Ref. [27] for the Q-plus cantilever assuming a spring constant $k = 1200\text{Nm}^{-1}$ and oscillation amplitude of 1nm, a tip radius of 12nm, and an SiO_2 film thickness of 10nm. (b) Measurements of the cantilever frequency shift $\Delta f(V)$ as a function of the DC bias voltage V for positive (black) and negative (blue) sweeps while the tip position (laterally and vertically) remains unchanged relative to the SiO_2 surface. Single electron tunneling events are observed around $V \approx -3.6$V, with a hysteresis that is highlighted by the inset plot (c) that shows the same data as (b) on magnified scales.

cantilever voltage reveals an approximately 100mV wide hysteresis between electron tunneling into and out of the sample surface, causing a hysteresis between the Fermi energy of the Pt tip and the surface defect level of about ≈30meV (voltage drop scaled into gap). This hysteresis is only partially caused by thermal activation as the thermal energy at 77K is approx. 6.6meV. Instead, this hysteresis can be attributed to the interplay between the given tunneling probability (the tunneling rate coefficient that is governed by the sample surface to tip distance) and the dynamics of the voltage sweep [27]. As the Fermi level shifts above (below) the defect level during a negative (positive) tip–to–surface voltage ramp for a given comparatively large tip–surface gap [8.5Å for the experiment represented by Fig. 6.2 (b) and (c)], the actual tunneling event may take place a finite amount of time after the voltage has passed the tunneling threshold.

After finding a cantilever lateral position within the SiO_2 surface and a distance from the SiO_2 surface (8.5Å) where tunneling is possible, we fixed both parameters and performed tunneling spectroscopy by sweeping the bias voltage between $V = -4$V and +2V. The results of these measurements of the frequency shift $\Delta f(V)$ as a function of the bias voltage V are shown in Fig. 6.2(b) for a positive (black) and a negative (blue) bias sweep. The data sets confirm that tunneling occurs at a particular Fermi energy of the probe, with a small hysteresis of about 150mV shown in the inset plot of Fig. 6.2(b) between a positive sweep, corresponding to a gap voltage hysteresis of about 37mV under consideration of the silicon dioxide layer. We have repeated the experiment displayed in Fig. 6.2 at more than 1473 arbitrarily chosen lateral positions and found single electron transitions at 164 ($\approx 11\%$) of these attempts with similar behavior. Since the localization of point defects in SiO_2 is known to be very strong [13, 10], we conclude that for the measurements where single electron transitions were not observed, the tip to defect distances were outside the tunneling regime. For an assumed tunneling within surface area of radius of 10nm, the observed probability of finding tunneling events leads to a density of localized states of $3.1 \times 10^{10}\text{cm}^{-2}$, consistent with the known defect densities of high–temperature grown SiO_2 layer [13].

When tunneling was observed at a given lateral tip position, the experiment shown

in Fig. 6.2 could be repeated for different tip–to-surface distance d, if the bias voltage V was adjusted appropriately such that the resonant alignment of the reservoir–Fermi level and the localized state was maintained.

6.5 Random tunneling signal (RTS)

Following the observations shown in Fig. 6.2, we continued to monitor $\Delta f(t)$ as a function of time while d and V where kept constant at values that favor tunneling events (when the reservoir–Fermi level and the level of the localized state are within the thermal energy) as determined in way described above. Figure 6.3(a) displays these functions for four different tip–to–surface gaps recorded over 6 second time intervals. Note that in order to improve the statistical analysis, these measurements were repeated two or three times for each distance. For each applied tip–to-surface gap d, all measurements are plotted in Fig. 6.3(a) consecutively onto the same time axis, with the separation between the measurements labeled on the time axis. For $d = 1(1)$Å, the function $\Delta f(t)$ displays noise that is identifiable as RTN only after analysis in a histogram which sorts the observed frequency shift into bins with 10mHz widths. The corresponding histogram displayed in Fig. 6.3(b) which is based on the 6s of data reveals a multimodal distribution of $\Delta f(t)$ with two main peaks centered approximately around about -9Hz and -7Hz, respectively. As the bimodality is the hallmark of RTN, this is proof that the observed time–domain noise has a strong RTN component. By repetition of this procedure, we also observed RTN signals for tip–to–surface distances of $d = 1.5(1)$Å, 2.0(1)Å, and 2.5(1)Å. Since the lateral cantilever position remained nominally unchanged between these measurement, all data displayed in Fig. 6.3 involve the same localized electronic state.

The comparison of the data sets in Fig. 6.3(a) and (b) collected for different tip–to–surface distance reveals three qualitative observations: (i) RTS is observed for the probed lateral cantilever position and all probed vertical tip distances. We conclude from this that during our experiment, the scanning probe experiment was stable enough to maintain all experimental conditions, i.e., the position of the probe relative to the observed electronic state; (ii) The center of both frequency shift peaks increases with decreasing d. This observation is caused by the increasing electrostatic forces

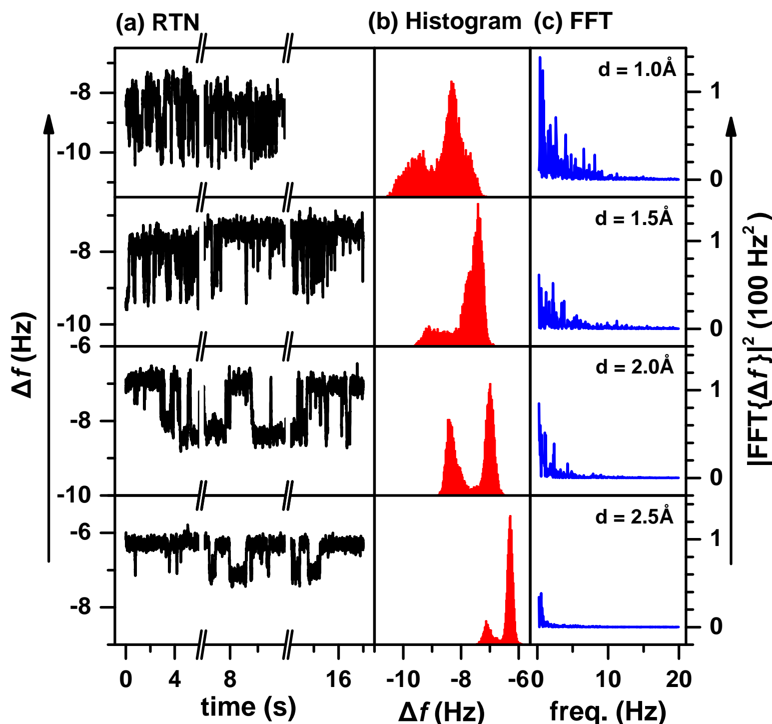

Figure 6.3. RTS at different tip-to-sample gap and corresponding histogram and noise spectra. (a) RTS signal with metal tip and a dielectric sample at different tip-sample gaps at 77K in darkness. The extra noise in Δf is due to a single electron shuttling back-and-forth between probe and sample. At smaller gap, the shuttling rate is very high which leads to the unresolved step and while tip–sample gap increased, the rate goes down which results in a step like Δf. (b) Histograms of the frequency shift data with 10mHz bin size. The histograms show the relative amount of time the electron spends in the tip and trap state as a function of height. It also reveals the discrete nature (bimodal) of electron tunneling. Two discrete peaks confirms that there is only one electron shuttling back-and-forth between tip and sample. The two peaks in the smallest gap are smeared due to the finite bandwidth in the detection system. (c) Plot of the square of Fast Fourier Transforms of the RTS signal. The higher frequency components at smaller tip-sample gap compared to lower frequency component at larger tip-sample gap confirms that rate of electron shuttling increased while reducing the gap.

between the tip and surface; (iii) The frequency separation of the two modes fluctuates statistically around an average value of $\delta f = 1.4$Hz with a standard deviation of $\sigma_\delta =$ 0.2Hz matching theoretical calculations for single electron forces [27] under the given experimental parameters. Note that these values were determined not just from the displayed four data sets but transient RTN data obtained from 40 transients measured at 7 location of the ≈164 cites on which single electron tunneling events were detected.

We conclude from the presence of fluctuations around the theoretically predicted value that local charge fluctuations in proximity of the probed electronic state influence the force measurement; (iv) Comparison of the four data in (a) shows that the RTS becomes monotonously faster as d decreases. Qualitatively, this is expected from elementary quantum mechanics; the tunneling probability increases when the tunnel barrier width is decreased. In order to scrutinize this quantitatively, we analyzed the dynamic tunneling behavior [i.e., the time–dependence of $\Delta f(t)$] by conducting fast Fourier transformations (FFT) whose results are displayed in Fig. 6.3(c) for each value of d.

These data confirm the observation that tunneling processes occur more frequently when d decreases. For smaller d, the FFT components at higher frequencies are much more pronounced. If the observed RTN is truly governed by spontaneous tunneling events that occur with a probability r, the FFT data must obey a Lorentzian shape $\mathrm{FFT}\,[\Delta(t)]\,(f) \propto r^2/\left(f^2+r^2\right)$ that is centered around 0Hz. However, given the finite length of the RTN transients, the fit of the data in Fig. 6.3(c) will reveal limited agreement solely on the ground of the statistic fluctuations seen in Fig. 6.3(c). Thus, in order to reduce the influence of these statistical fluctuation, we numerically calculated the integral function of each FFT data set in the range between 0.6Hz to 300Hz and then fitted the resulting data set with an integrated Lorentz function $F(f) = A \arctan\left(f/r\right)$ as shown in Fig. 6.4(a) to (d). The lower integration interval boundary was chosen to be 0.6Hz in order to exclude influences of the DC components of the time transients during the 6s recording interval (a rapidly decaying slit function whose influence becomes negligible above 0.6Hz). The fits display excellent agreement with the integrated data sets. Figure 6.4(e) contains a semi–logarithmic plot of the fit results for the Lorentzian widths r as a function of tip–to–surface gap d (black data points). These experimentally obtained data were then fit with an exponential decay function which is also displayed in Fig. 6.4 as a linear function (red line). As expected from the tunneling theory by Zheng et al. [27], the exponential fit shows good agreement with the tunneling rate coefficients r and it reveals an barrier height of $\Phi = 5.3(3)$eV, in good agreement with the work–function of Pt [8].

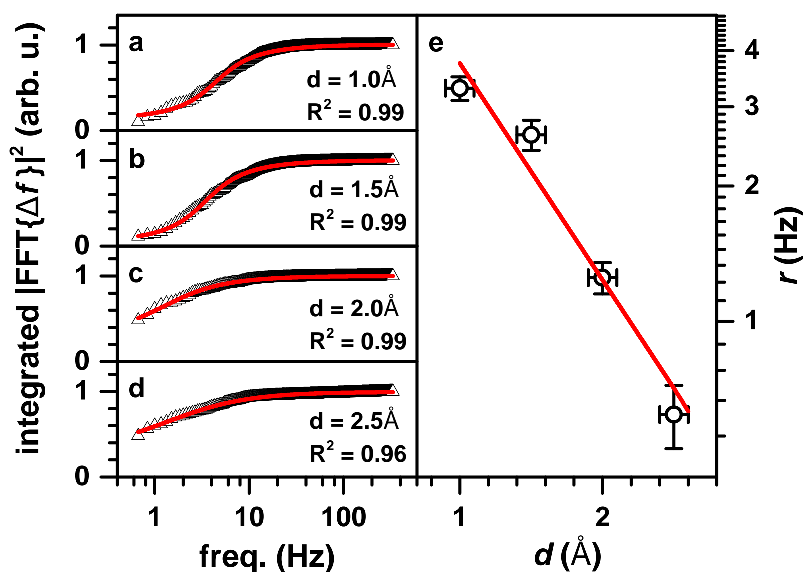

Figure 6.4. Integrated RTS spectra and electron shuttling rate calculation. (a) to (d): The black data points represent the integrated RTS power spectra for different cantilever distances d obtained from the data in Fig. 6.3(c). The integration interval was 0.6Hz to 300Hz. The red lines present the result of fits with integrated Lorentzian functions centered around 0Hz. (b) Semilogarithmic plot of the Lorentzian decay width r obtained from the fit results shown in (a) to (d)) as a function of the tip–to–sample gap d. The agreement of the data with a linear fit reveals the exponential dependence of the tunneling probability on d.

6.6 Conclusion

In conclusion, we have demonstrated the transient observation of individual electron tunneling transitions between a Pt Fermi reservoir and a localized state in an SiO_2 surface using scanning probe detected electrostatic force measurements. The observed tunneling dynamics confirms the exponential tunnel–barrier width dependence of the tunneling probability. The detection of single–electron tunneling transitions between a scanning probe and localized electron states is a step towards the achievement of single–spin detection on electrically isolated, highly localized electron states [18].

6.7 References

[1] G. Binnig, H. Rohrer, Ch. Gerber, and E. Weibel. Surface studies by scanning tunneling microscopy. *Phys. Rev. Lett.*, 49:57, 1982.

[2] E. Bussman. *Single Electron Tunneling Force Microscopy, Thesis.* University of Utah, 2006.

[3] E Bussmann, D. J. Kim, and CC Williams. Single-electron tunneling to insulator surfaces measured by frequency detection electrostatic force microscopy. *Appl. Phys. Lett.*, 85:2538, 2004.

[4] E. Bussmann and C. C. Williams. Single-electron tunneling force spectroscopy of an individual electronic state in a nonconducting surface. *Appl. Phys. Lett.*, 88:263108, 2006.

[5] E. Bussmann, N. Zheng, and C. C. Williams. Single-electron manipulation to and from a SiO_2 surface by electrostatic force microscopy. *Appl. Phys. Lett.*, 86:163109, 2005.

[6] L. Esaki. New phenomenon in narrow germanium $p-n$ junctions. *Phys. Rev.*, 109:603, 1958.

[7] R. W. Gurney and E. U. Condon. Wave mechanics and radioactive disintegration. *Nature*, 122:439, 1928.

[8] W. M Haynes. *CRC Handbook of Chemistry and Physics.* CRC press, 2013.

[9] A. T. Johnson, L. P. Kouwenhoven, W. De Jong, N. C. Van der Vaart, C. J. P. M. Harmans, and C. T. Foxon. Zero-dimensional states and single electron charging in quantum dots. *Phys. Rev. Lett.*, 69:1592, 1992.

[10] J. P. Johnson, D. W. Winslow, and C. C. Williams. Measurement of depth and energy of buried trap states in dielectric films by single electron tunneling force spectroscopy. *Appl. Phys. Lett.*, 98:052902, 2011.

[11] B. D. Josephson. Possible new effects in superconductive tunneling. *Phys. Lett.*, 1:251, 1962.

[12] L. J. Klein and C. C. Williams. Single electron tunneling detected by electrostatic force. *Appl. Phys. Lett.*, 79:1828, 2001.

[13] P. M. Lenahan and J. F. Conley. What can electron paramagnetic resonance tell us about the Si/SiO_2 system. *J. Vac. Sci. Technol. B*, 16:2134, 1998.

[14] C. Matta. *Quantum Biochemistry.* John Wiley & Sons, 2010.

[15] S. Morita and F. J. Giessible. *Noncontact Atomic Force Microscopy.* Springer, 2009.

[16] J. R. Oppenheimer. Three notes on the quantum theory of aperiodic effects. *Phys. Rev.*, 31:66, 1928.

[17] A. Payne, K. Ambal, C. Boehme, and C. C. Williams. Atomic-resolution single-spin magnetic resonance detection concept based on tunneling force microscopy. *Phys. Rev. B*, 91:195433, 2015.

[18] A. Payne, K. Ambal, C. Boehme, and C. C. Williams. Atomic-resolution single-spin magnetic resonance detection concept based on tunneling force microscopy. *Phys. Rev. B*, 91:195433, 2015.

[19] rmnano.com. Rocky mountain nanotechnology.

[20] K. Y. Tan, K. W. Chan, M. Mottonen, A. Morello, C. Yang, J. van Donkelaar, A. Alves, J.-M. Pirkkalainen, D. N Jamieson, R. G Clark, et al. Transport spectroscopy of single phosphorus donors in a silicon nanoscale transistor. *Nano Lett.*, 10:11, 2009.

[21] J. Tersoff and D. R. Hamann. Theory and application for the scanning tunneling microscope. *Phys. Rev. Lett.*, 50:1998, 1983.

[22] R. Tsu and L. Esaki. Tunneling in a finite superlattice. *Appl. Phys. Lett.*, 22:562, 1973.

[23] N. C. Van der Vaart, S. F. Godijn, Y. V. Nazarov, C. J. P. M. Harmans, J. E. Mooij, L. W. Molenkamp, and C. T. Foxon. Resonant tunneling through two discrete energy states. *Phys. Rev. Lett.*, 74:4702, 1995.

[24] R. Wang and C. C. Williams. Dynamic tunneling force microscopy for characterizing electronic trap states in non-conductive surfaces. *Review of Scientific Instruments*, 86:093708, 2015.

[25] J. Weis, R. J. Haug, K. V. Klitzing, and K. Ploog. Competing channels in single-electron tunneling through a quantum dot. *Phys. Rev. Lett.*, 71:4019, 1993.

[26] N. Zheng, C. C. Williams, E. G. Mishchenko, and E. Bussmann. A three-dimensional model of single-electron tunneling between a conductive probe and a localized electronic state in a dielectric. *J. Appl. Phys.*, 101:093702, 2007.

[27] N. Zheng, C. C. Williams, E. G. Mishchenko, and E. Bussmann. A three-dimensional model of single-electron tunneling between a conductive probe and a localized electronic state in a dielectric. *J. Appl. Phys.*, 101:093702, 2007.

CHAPTER 7

SUMMARY AND OUTLOOK

In the course of this dissertation, prerequisite studies aiming at the implementation of a concept for single–electron spin spectroscopy with atomic scale resolution, the so-called single–spin magnetic resonance tunneling force microscopy (SSTFM), were carried out. SSTFM was discussed conceptually and simulations showing the experimental feasibility of this approach were shown. Several key requirements for the implementation of SSTFM were demonstrated experimentally, including (i) that it is possible to fabricate thin silicondioxide layers on crystalline silicon with very high densities ($[E'] > 5 \times 10^{18}\text{cm}^{-3}$) of paramagnetic silicon dangling bonds (so–called E' centers) that possess an appropriate relaxation dynamics (longitudinal relaxation times $T_1 \approx 600\mu$S at 5K) for their utilization as spin–readout probes for SSTFM; (ii) that a commercial ultra-high vacuum scanning probe microscope can be modified such that magnetic resonant excitation of electron spins will be possible at low magnetic fields (≈20mT), where both the magnitude and the direction of the magnetic field vector around the probe could be manipulated and monitored with high accuracy using electrically detected magnetic resonance magnetometry based on spin–dependent recombination in a conducting polymer–thin film; (iii) that single paramagnetic defect states in crystalline silicon, namely phosphorus donor electron states and silicon dangling bond states, can be detected using conduction atomic force microscopy (c-AFM), which was also used for the characterization of the current–voltage curve of individual pairs of phosphorus and dangling bond states; and (iv) that the RTS of individual electron tunneling between a metal probe and a surface state was verified. Furthermore, using the measured barrier–width dependence of the single electron tunneling dynamics, it is confirmed that the barrier height of the probe is 5.3(3) eV.

In spite of the work presented above, SSTFM has so far still not been demonstrated experimentally. However, none of the results presented above suggest that there are

fundamental obstacles that would prevent its implementability. Thus, future work based on the dissertation presented here will have to focus on further progress on SSTFM. From the observed charge carrier transition rates through the P/P_b pairs (the electric currents), we know that a successful application of SSTFM will require magnetic resonant spin manipulation faster than the average single electron transition rate of less than 1μs. Thus, the existing scanning probe setup will have to be modified in order to allow for larger magnetic driving fields B_1. This could be achieved by using micro–wire (strip–line) resonators for the RF excitation that are operated in the near field regime (i.e., substrate height $<<$ width of the strip–line. Furthermore, aside from an improved magnetic resonance excitation setup, tunneling between individual states located in two dielectric surfaces (one on a AFM tip and the other as the sample surface) will have to be demonstrated since the RTS presented above was all obtained from a metal to dielectric system. This goal, which requires not just to bring two dielectric layers in close proximity but also that two localized states within these layers be spatially aligned, is probably the greatest challenge to overcome. Most likely, this can be achieved through an incremental iteration process where first, the metal to dielectric–layer based tunneling experiment is repeated with the metal and the dielectric swapped between tip and sample surface, before a tunneling experiment based on all–dielectric materials is attempted. In any case, a successful demonstration of SSTFM would be a major breakthrough since it would not only open new avenues for defect detection and characterization but also enable entirely new pathways to pursue spin–based storage and quantum storage as well as processing.